CHARACTERIZATION OF FRACTURED RESERVOIR AND SIMULATION OF EOR TECHNIQUES

A Dissertation

by

GENG NIU

Submitted to the Office of Graduate and Professional Studies of
Texas A&M University
in partial fulfillment of the requirements for the degree of
DOCTOR OF PHILOSOPHY

Chair of Committee,	David Schechter
Committee Members,	Kan Wu
	Hadi Nasrabadi
	Yuefeng Sun
Head of Department,	Jeff Spath

August 2019

Major Subject: Petroleum Engineering

ABSTRACT

Oil production from the fractured tight reservoirs has been increasing since the early 2000s and now accounts for a large portion of onshore US oil production. Complex fracture network composed of hydraulic fractures and natural fractures plays an important role in well depletion, but its geometry and properties have large uncertainty. On the other hand, different methods to improve oil recovery in the fractured tight reservoir have been tested in labs and fields recently. Although people generally understand the micro-mechanisms of these methods, the impact of fracture network on production enhancement has not been systematically studied.

In this study, unstructured gridding algorithms are improved to apply to the reservoir with high fracture density. Then the depletion behavior of the dual-porosity methods and the discrete fracture network (DFN) method are compared based on the conceptual model, demonstrating the necessity of using DFN method in the fractured tight reservoirs. In terms of DFN application in real formations, microseismicity (MS), core observation, pumping schedule, outcrop map, and FMI log are used to characterize their fracture network geometry. History match is done to calibrate the reservoir models, which can gain confidence in using the DFN models for further study. To model EOR techniques in field scale, micro-mechanisms revealed from lab experiments about surfactant imbibition and CO_2 huff n' puff are used to generate appropriate simulation parameters. A series of surfactant spontaneous imbibition and CO_2 huff n' puff simulations are done on those calibrated models to study the EOR performance and seek the optimal operation parameters.

Simulation results show that dual-porosity methods cannot take the transition flow between fracture-matrix into account, and cannot accurately model the discontinuity feature of fracture networks, which are critical to EOR performance. After calibration, DFN dynamic fluid flow

models can approximately match the production data. Surfactant spontaneous imbibition simulation shows a marginal production increase compared to water imbibition cases. It is found that wettability alteration incurred in the fracture system could play a more important role in production enhancement, compared to the wettability alteration incurred in a small range of matrix. Simulation results of CO_2 huff n' puff indicate injection pressure and injection schedule impact the recovery performance.

This study proposes a workflow to build reliable DFN models to represent fractured tight reservoirs with the use of multiple data sources. Furthermore, the performance of EOR technics is investigated with various scenarios. It is found that fracture geometry significantly affects depletion and EOR performance, so that appropriate field-scale simulation, in addition to core-scale experiments, is recommended for EOR pilot design.

DEDICATION

To my parents, Jingang Niu and Shuping Chen,

for their encouragement and support.

To my wife, Yi Xiao,

for being with me and sharing happiness and joy.

To my colleagues and friends,

for their discussions and insights through my research.

ACKNOWLEDGMENTS

I would like to express my highest gratitude to my committee chair, Dr. David Schechter for his advice, patience, encouragement and financial support during this study.

My appreciation is also extended to my committee members, Dr. Kan Wu, Dr. Hadi Nasrabadi, and Dr. Yuefeng Sun for their guidance and support throughout the course of this research.

Thanks also go to my friends and colleagues in the department, especially to Dr. Jianlei Sun. Jianlei helped me step into the research of reservoir modeling. I also want to extend my gratitude to CNOOC International for its financial support and research guidance.

Finally, I would like to thank my family for their encouragement and continuous support.

CONTRIBUTORS & FUNDING SOURCES

Contributors

This work was supported by a dissertation committee consisting of Professor David Schechter, Kan Wu, and Hadi Nasrabadi of the Department of Petroleum Engineering and Professor Yuefeng Sun of the Department of Geology & Geophysics.

All the work conducted for the dissertation was completed by the student independently.

Funding Sources

Graduate study was supported by a research funding from CNOOC International Limited.

NOMENCLATURE

BHP	Bottom-Hole Flowing Pressure
DAS	Distributed Acoustic Sensing
DFN	Discrete Fracture Network
DP	Dual Porosity
DPDK	Dual Porosity Dual Permeability
DTS	Distributed Temperature Sensing
EDFM	Embedded Discrete Fracture Modeling
EOR	Enhanced Oil Recovery
EOS	Equation of State
EUR	Estimated Ultimate Recovery
FDM	Finite Difference Method
FEM	Finite Element Method
FVM	Finite Volume Method
GOR	Gas Oil Ratio
HF	Hydraulic Fractures
HnP	Huff n' Puff
IFT	Interfacial Tension
MMP	Minimum Miscibility Pressure
NF	Natural Fractures
NNC	Non-Neighbor Connections
PEBI	Perpendicular Bisector

PSS	Pseudo-Steady State
PV	Pore Volume
SRV	Stimulated Reservoir Volume
WOR	Water Oil Ratio

TABLE OF CONTENT

Page

LIST OF FIGURES

Page

LIST OF TABLES

Page

CHAPTER I

INTRODUCTION

1.1 Approaches to Model Fractured Reservoirs

Hydraulic fractures (HF) and natural fractures (NF), which construct complex fracture networks with high conductivity, play a significant role in unconventional reservoir production. Several approaches have been developed to model these complex fracture networks. One class is the continuum approaches, such as the dual-porosity (DP) method, the dual-porosity dual-permeability (DPDK) method (Kazemi et al. 1976; Warren and Root 1963), the subdomain method (Beckner et al. 1991; Wu and Pruess 1988). These approaches assume an equally spacing orthogonal fracture network with perfect connection, and simplify the flow behavior between fracture and matrix. The other class is the discrete fracture networks (DFN) approaches. The DFN approaches explicitly model the fractures with arbitrary distribution for the purpose of depicting their geometry and conductivity. The fluid flow in the reservoirs represented by DFN could be solved analytically and numerically.

The semi-analytical method uses superposition principle with diffusion equations of the planar sinks (fracture panels) (Bao et al. 2017; Jia et al. 2015; Yu et al. 2014; Zhou et al. 2013). This method assumes the reservoir matrix is homogeneous. The computation time it uses is very short, but nonnegligible error exists in complex cases. Additionally, the semi-analytical method is not suitable for compositional simulation.

The numerical approaches to solve DFN problems relate to gridding methods and numerical discretization methods of the flow equations. Gridding methods include mesh-free methods and mesh-dependent methods.

The mesh-free methods or nonconformal methods incorporate fracture information implicitly into the background-grid systems. Thus, they avoid the meshing of complex fracture networks. One of the mesh-free methods, embedded-discrete-fracture model (EDFM), uses additional grids in the computation domain to represent fracture segments. The transmissibilities of matrix/fracture and fracture/fracture fluid flow are computed and added to matrix system as additional non-neighbor connections (Li and Lee 2008; Liang and Du 2018; Moinfar et al. 2014). The gridding system used is structured: Cartesian or corner-point (Xu and Sepehrnoori 2019). The EDFM method cannot capture the early transient flow without refinement in matrix blocks (Chai et al. 2016). Consequently, to model reservoirs with high-density fractures or to study problems with severe change near fractures, very fine grids are required, which leads to tremendous grid numbers. In other words, the advantages of mesh-free are weakened. Another mesh-free method named multisegment well (MSW) was developed (Du et al. 2015; Edwards et al. 2013). MSW uses wellbore nodes to represent high-conductivity fractures, which makes the fracture grid not necessarily to contact to each other through the grid faces. However, MSW has the similar issues in modeling very complex networks as EDFM.

The mesh-dependent methods are trying to explicitly model the fracture networks. Fracture blocks are differentiated from matrix blocks by assigning different properties. Local-grid-refinement (LGR) has been widely accepted as the major fracture gridding method in the industry because of its simplicity and availability in several commercial simulator packages (Correia et al. 2012). It uses a zigzag shape of line segments with refinement to represent fractures based on the

structured tartan grids. The main advantage of the LGR method is simple and fast. It also comes with several disadvantages. The fracture length in LGR method is not accurate, leading to an error in simulation results. Additionally, it is very difficult to coarsen the reservoir background grids because the background-grid size depends on the fracture-grid size.

Another category of mesh-dependent methods is the unstructured grid, such as the triangular grid and the perpendicular bisector (PEBI) grid. The unstructured grid approaches have the advantage to conform the complex geometry of fractures and wells by explicitly modeling those. Triangular grid approaches treat fracture intersections through the introduction of a special node at each intersection (Caillabet et al. 2000; Caillabet et al. 2001). Such treatment works well for single-phase flow, but problems arise for multiphase flow. The reason is that the small size of these special nodes can lead to difficulties in the stability and allowable timestep of the computation. An improved method was developed by Granet et al. (2001), which assumed there is no accumulation term at the interaction, and introduced a modified upwinding for the intersection nodes. That is to say, the triangular grid approaches have compatibility issues with commercial simulators.

A more favorable unstructured grid approach is the PEBI grid. If a Delaunay triangulation is applied to the triangular grids, then the dual grid is a PEBI or Voronoi grid. Such grid system makes two-point approximations applicable, and commercial simulators could be used for computation (Karimi-Fard et al. 2004). PEBI grid is capable to locally conform to the fracture networks and reduce grid orientation effects (Heinemann et al. 1991). Additionally, it is also able to handle non-uniform aperture distribution and low-angle intersections, and generate the minimum number of grids required, resulting in enhancement of the simulation accuracy with the

lowest possible computational cost (Olorode et al. 2012; Sun and Schechter 2015; Sun et al. 2015, 2016b; Wang and Shahvali 2016). However, the generation of PEBI grid is a difficult process.

The numerical discretization methods of the flow equations include finite-element methods (FEM), finite-difference method (FDM), finite-volume (or control volume finite-difference) method (FVM), and equivalent 1-D finite-difference based on Eikonal equation. FEM use the integral form of the governing equations to formulate the mathematical discretization. The mesh nodes can be discretionarily distributed in the area of interest with complex geometry. The existing approaches based on FEM are successful in the simulation of single-phase flow and heat transfer. But for multiphase flow in highly heterogeneous medium, since they do not ensure local mass conservation, saturation results could have significant error (Baca et al. 1984; Juanes et al. 2002; Karimi-Fard and Firoozabadi 2001; Kim and Deo 2000; Riviè et al. 2000). Moreover, FEM is generally expensive in computation.

FDM and FVM are widely used in commercial simulators. FDM uses the differential form of the governing equations to formulate the mathematical discretization. One of the popular simulators using FDM is CMG. FDM is easy to understand and code, but they need very fine grids to achieve mass conservation. Like FEM, FVM also uses the integral form of the governing equations. FVM is a combination of FDM and FEM. The popular simulators using FVM are Schlumberger Eclipse and Halliburton Nexus. FVM can have mass conservation no matter the grids are fine or coarse. Both FDM and FVM can compute structured and unstructured grids.

A special FEM is a method based on the Eikonal equation and fast marching method (FMM). Together with gridding technics of EDFM and PEBI, FMM has been used to study the depletion problems in fractured reservoirs (Xue et al. 2018; Xue et al. 2016; Yang et al. 2017a; Yang et al. 2017b). FMM assumes that the pressure contour is the same as the diffusive time of

flight (DTOF) contour. As a result, the three-dimensional diffusivity equation, which describes the reservoir fluid flow, is reduced to an equivalent one-dimensional formulation, requiring less computation time (Li and King 2016). However, such assumption may not be true for the reservoirs with high heterogeneity, resulting in significant inaccuracy (Wang et al. 2017). Thus, the feasibility of using FMM to model reservoirs with complex fracture network is questionable. Moreover, EOR processes in fractured reservoirs, which involve a significant change in phase saturation and component fractions, may be impossible to be handled by FMM.

Most of the published research about the unstructured grid used arbitrary DFN or stochastic DFN in terms of DFN generation. Few field data were utilized in their DFN generation approaches. Lack of the knowledge of appropriate approaches to use field data to generate DFN geometry could be a reason that DFN method is not as popular as the DP method in the industry. One goal of this work is to develop workflows that making use of available field data in DFN geometry generation and reservoir model calibration.

1.2 Surfactant Spontaneous Imbibition in Tight Rock

Unlike the flooding procedure in conventional reservoirs with high permeability, surfactant EOR in unconventional reservoirs is a process in which surfactant is added into hydraulic fracturing fluid and reservoirs are soaked for a period. Many kinds of surfactant have been tested on different reservoir rocks in the labs. Spontaneous imbibition experiments were presented in every study, directly evaluating the surfactant performance in oil production enhancement. For Wolfcamp rocks, cationic surfactant showed the best performance on the carbonate-rich rock, while anionic surfactant showed the best performance on the quartz-rich rock (Alvarez and Schechter 2017).

Water spontaneous imbibition experiments on the conventional core (permeability > 300 md) showed higher recovery factors, which were more than 10% (Zhou et al. 2000). The recovery factors of water imbibition on unconventional (tight) cores were generally less than 10% (Zhang et al. 2018a). Besides, the diameter of the conventional cores was 1.5 inch, which was bigger than that of the tight cores (1 inch). And it took much longer time for the conventional core to reach equilibrium status for the imbibition experiments. Additionally, the CT image of tight cores during imbibition indicated the density change was more severe at the edge than that in the center. One possible explanation was that for the conventional cores, water can penetrate deeply into the center of the core because of its high permeability. Capillary pressure altered there needed a relatively long time to push oil trapped in the center outward. For tight cores, the penetration of water was limited, and capillary pressure was unlikely to push out deeply trapped oil in low permeability zone. So it did not take that much time to finish imbibition process incurred in the shallow area.

Surfactant-assisted spontaneous imbibition on tight cores could result in an oil recovery of 35% (Saputra and Schechter 2018). And such imbibition process usually ended within a shorter period, compared to water imbibition. A rational reason was that the decreased interfacial tension, compared to water, increased the rate of the countercurrent flow. Further discussion is carried out in Chapter VI.

1.3 CO_2 Huff n' Puff in Tight Rock

Lab experiments of CO_2 huff-n-puff (HnP) on re-saturated tight rock showed a recovery factor of 49%, and revealed that the dominant microscopic mechanisms are vaporization and oil expansion (Adel et al. 2018; Tovar et al. 2018a, 2018b). A large portion of the produced oil is recovered during the first cycle, which was considered to be a rapid process compared to several months of re-saturation. The results also showed that operating pressure has a great influence on the recovery factor, especially, elevated pressure beyond MMP leads to a higher recovery factor. More discussion of the detail about experiments and simulation is in Chapter VII.

1.4 Research Objective

For simulation of fractured reservoirs, although some gridding methods such as EDFM described above, and some numerical methods such as surrogates models and proxy models (Bao and Gildin 2017; Bao et al. 2018) could significantly reduce the computation cost, they cannot achieve accurate results for EOR processes in reservoirs with high fracture density, due to either the lack of underlying physics of the reservoir fluid interactions or numerical simplifications in these methods. Therefore, PEBI grid with FVM simulator is selected for this work to capture the detailed change near fractures during depletion and EOR. The FVM simulator used for this work is Nexus from Halliburton. Additionally, FEM simulators, IMEX and GEM from CMG, are also used to run single-porosity models and DP models. The PEBI grid generator is an in-house software coded with MATLAB.

Throughout this work, I will try to resolve the following questions:

1) How to properly mesh the reservoirs with high-density fractures based on PEBI grid?

2) What are the differences between DP methods and DFN method?

3) How do we incorporate different sources of field data to generate DFN geometry?

4) What is the performance of surfactant spontaneous imbibition in field scale?

5) What is the performance of CO_2 huff n' puff in field scale? What are the impact factors?

CHAPTER II

IMPROVEMENT OF PEBI GRID GENERATION AND GRID SENSITIVITY STUDY ON MULTI-PHASE FLOW

2.1 Projection Points and Refinement at Intersection and Tips

In the process of mesh generation, when the grid size is large, fractures with small spacing may cause distortion of the grids near fractures. It is because the fixed points which conform to the fracture geometry may not be aligned for each pair of neighboring fractures. Reducing the size of the PEBI grid can increase additional layers among fractures to reduce distortion, but it will tremendously increase the number of grids. To overcome this issue, projection points are added to fractures if there are fracture tips nearby. This will make the fixed points from one fracture aligned to nearby fixed point from other neighboring fractures.

The original method of PEBI generation leads to relatively large intersection grid. It may cause inaccuracy if the number of intersections is large, and the distance between them is small. Yang et al. (2017b) proposed an approach to deal with the intersection grid, which could introduce minimum geometry alteration. However, the grid size of intersections is very small, and if there are multiple intersections, it may cause a convergence problem. Especially for the gas injection simulation, the saturation of the intersection gridblocks could change very rapidly. In this study, In order to minimize the error of simulation and improve the computation efficiency, this study adopts a refinement method to grid the intersection, tips and projection points by assigning additional fixed points with geometric progression spacing (**Fig. 1**). Fig. 2 shows the comparison of grids with and without refinement and projection points.

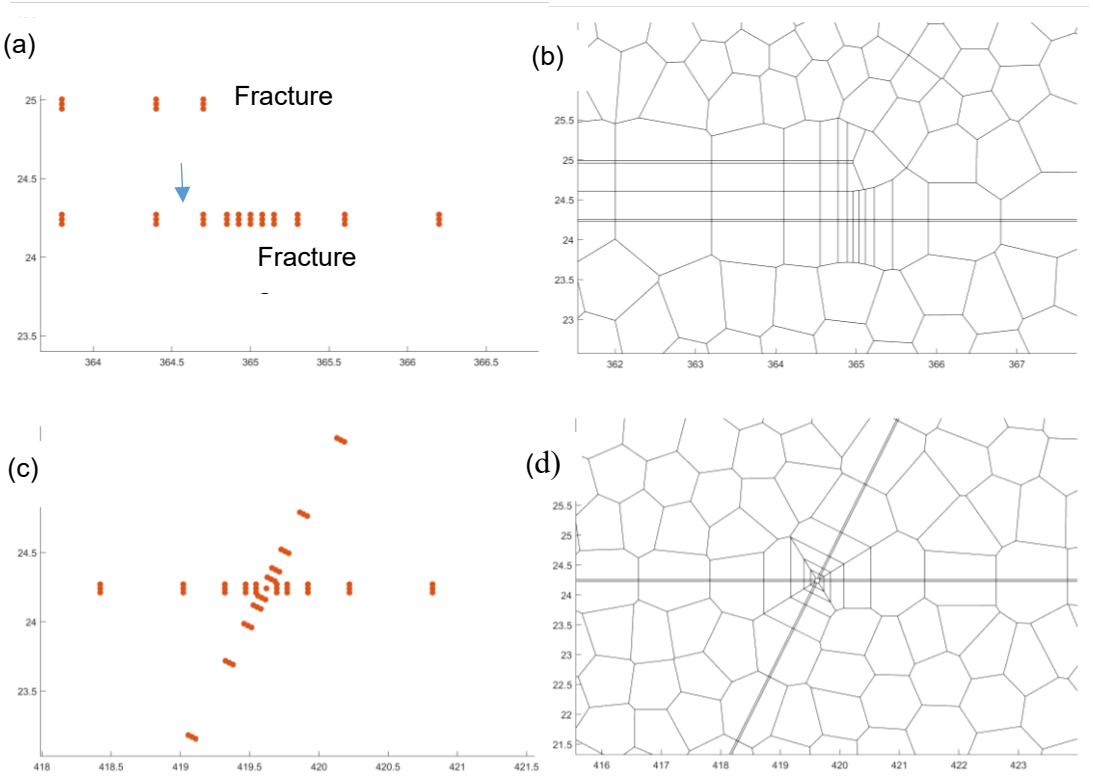

Fig. 1—(a) a projection point is added to the fracture 2, and refine fixed points are assigned around the tip of fracture 1 and projection point; (b) PEBI grids are generated at the tip and the projection point with geometric progression size; (c) refine fixed points are assigned around the intersection; (d) PEBI grids are generated at the intersection with geometric progression size.

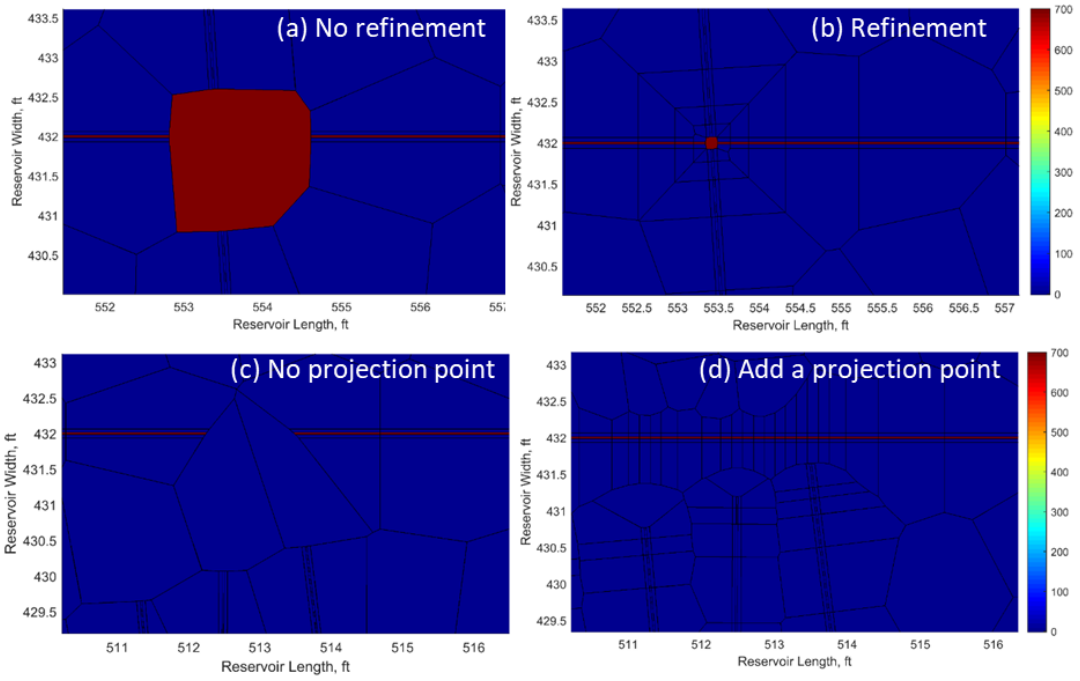

Fig. 2—Effect of applying refinement and adding projection point. (a) if no refinement is applied, the intersection grid is too large; (b) after refinement, the intersection grid is sufficiently small; (c) if projection point is not added to the fracture segment where tip is nearby, the matrix grid can interrupt the fracture; (d) after adding a projection point, the fracture can keep integrated.

2.2 Grid Sensitivity in Multi-Phase Flow

Coarse gridding gains error in simulation results, while fine gridding increases computation time. Therefore, an appropriate grid size should be determined for each specific problem. Generally, for fluid flow in reservoirs, grid with a relatively small difference in size should not shift the results too much, i.e., insensitivity in grid size. Sun (2016) showed that the results of depletion problems were not sensitive to either grid size or grid types. But the multi-phase simulation has not been systematically tested yet. To study the sensitivity of PEBI grid size for multi-phase flow, a single-fracture compositional model containing EOS of volatile oil is used. A Cartesian grid model and three PEBI grid models with a reference size of 2 ft, 4 ft, and 8 ft are generated, shown in 错误! 未找到引用源。.

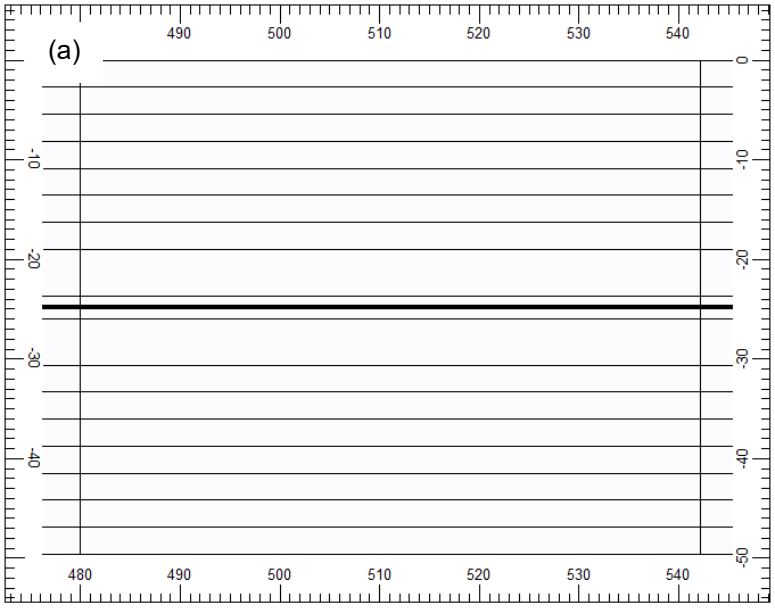

Fig. 3—Part of the grid in each model. (a) Cartesian grid; (b) (c) (d) PEBI grid with a reference size of 2ft, 4ft, and 8ft, respectively.

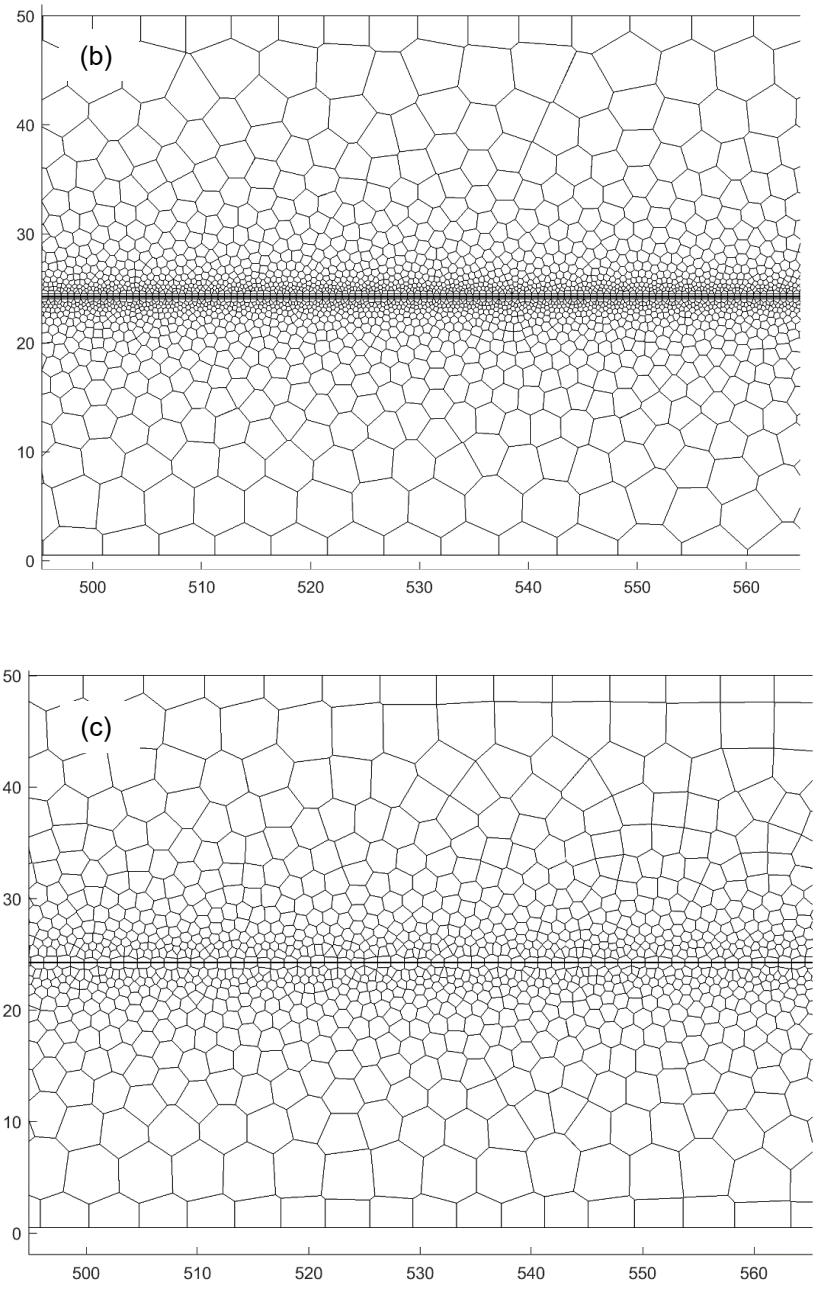

Fig. 3—Continue.

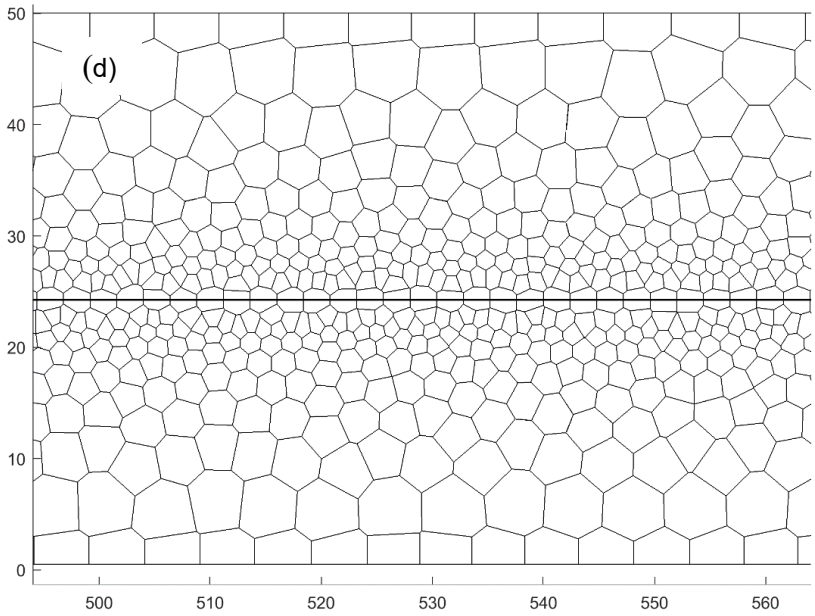

Fig. 3—Continue.

Firstly, single-phase fluid flow is tested by operating depletion above bubble point pressure. The purpose of this procedure is to ensure the input of PVT is correct for Nexus, since the EOS unit used in Nexus is different from that in CMG. Simulation results of cumulative oil production and GOR are shown in **Fig. 4** and **Fig. 5**. The results of models discretized by the Cartesian grid and the PEBI grid with various size match are in good agreement.

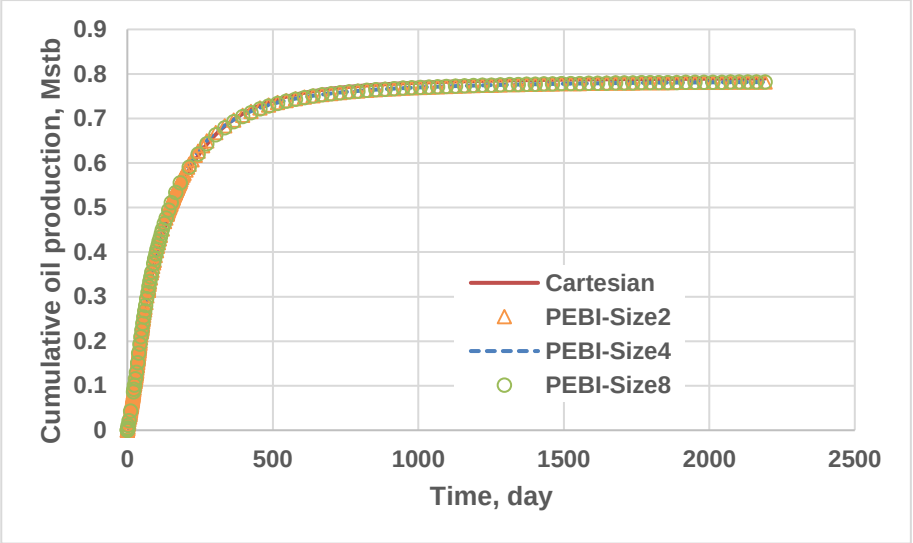

Fig. 4—Cumulative oil production of models with the Cartesian grid and the PEBI grid (2 ft, 4 ft, and 8 ft), simulating the single oil-phase flow.

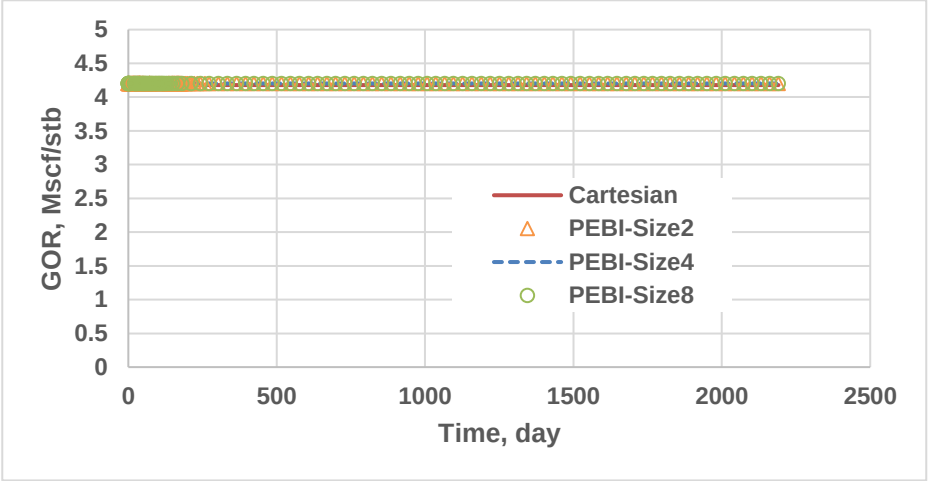

Fig. 5—GOR of models with the Cartesian grid and the PEBI grid (2 ft, 4 ft, and 8 ft), simulating the single oil-phase flow.

The match of cumulative oil production and GOR indicates the input of EOS for CMG and Nexus are the same. On the other hand, for single-phase flow, the simulation is not sensitive to the size of PEBI grid.

Secondly, two-phase flow is tested by setting the initial water saturation higher than the connate water saturation. This procedure designed is to make sure inputs of relative permeability curves and viscosities for CMG and Nexus simulations are the same. Simulation results of cumulative oil production, cumulative water production and water-oil ratio (WOR) are shown in **Fig. 6** and **Fig. 7**. The results of all models match well.

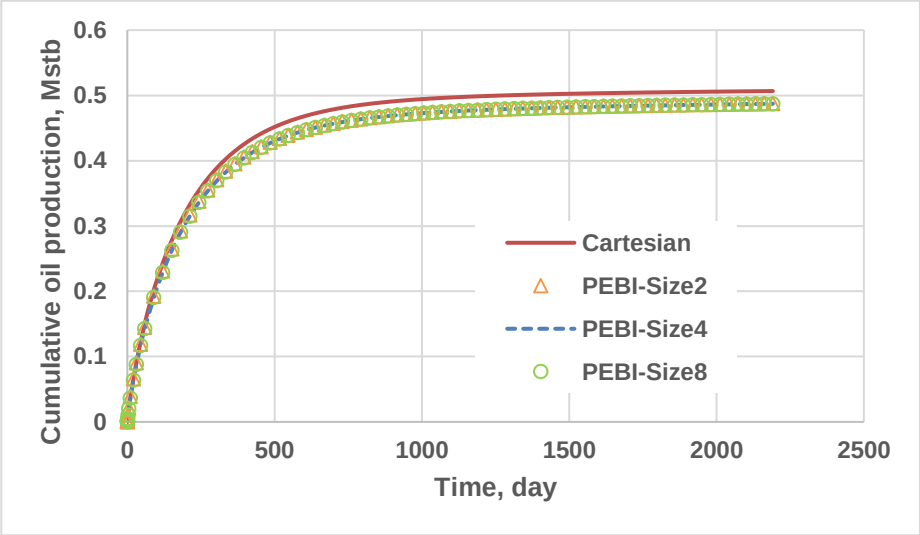

Fig. 6—Cumulative oil production of models with Cartesian grid and PEBI grid (2 ft, 4 ft and 8 ft), simulating the water-oil two-phase flow.

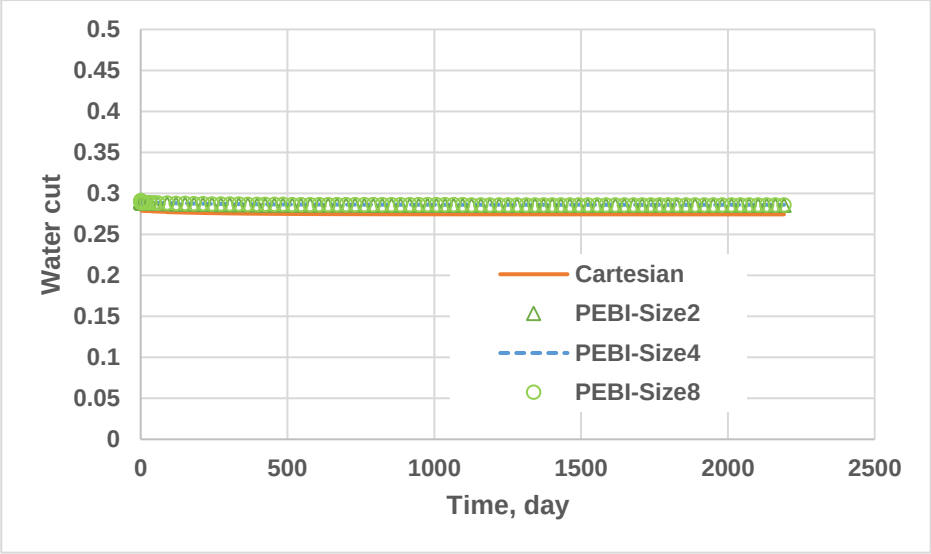

Fig. 7—Water cut of models with Cartesian grid and PEBI grid (2 ft, 4 ft, and 8 ft), simulating the water-oil two-phase flow.

Thirdly, the gas phase is involved by operating the bottom-hole pressure (BHP) under bubble point pressure. Initial water saturation is set to connate water saturation. Simulation results of cumulative oil production and gas-oil ratio (GOR) are shown in **Fig. 8** and **Fig. 9**. Only the results of the small PEBI size (2 ft) model match the results of the Cartesian model. For models with PEBI grid, larger size leads to late GOR increase and higher oil production.

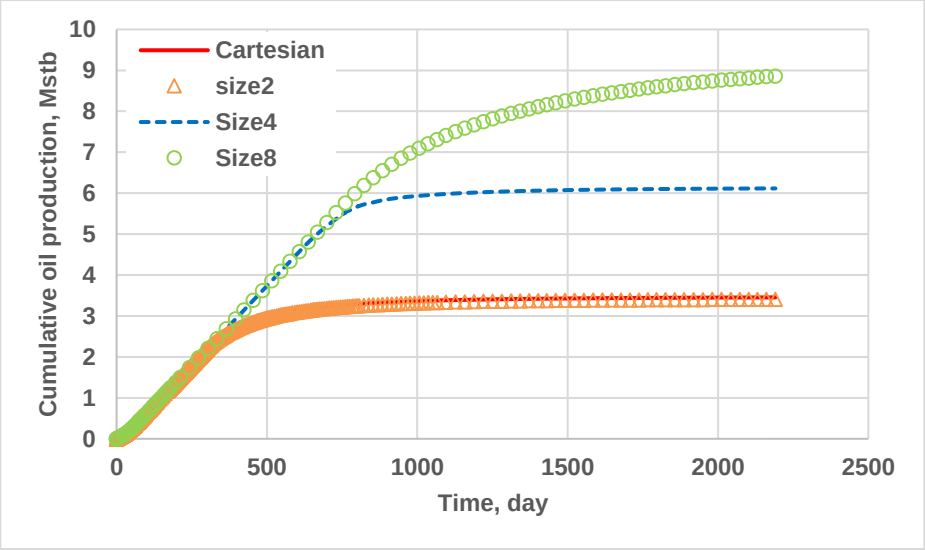

Fig. 8—Cumulative oil production of models with the Cartesian grid and the PEBI grid (2 ft, 4 ft, and 8 ft), simulating the gas-oil two-phase flow.

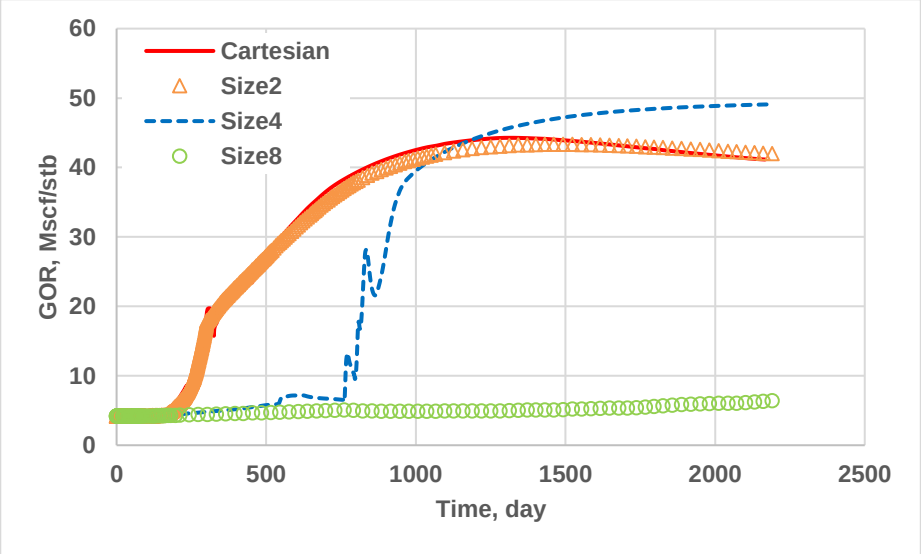

Fig. 9—GOR of models with the Cartesian grid and the PEBI grid (2 ft, 4 ft, and 8 ft), simulating the gas-oil two-phase flow.

Fig. 10 and **Fig. 11** show the gas saturation map and pressure map of the PEBI-Size8 model at 243 day, respectively. The calculated saturation pressure of this oil at reservoir temperature of

307 F is 3727.4 psi. It is observed that a large area where pressure lower than saturation pressure does not transfer to two-phase gridblocks, i.e., the two-phase front is late than the pressure front. The reason is that the simulator Nexus does not run a transition test on every gridblock at each time step by default, since it is computation consuming. It merely tests the single-phase gridblocks which neighbor two-phase gridblocks. So, if the time step is too large, even pressure of a new large area has depleted across the saturation pressure in this time step, only a layer of gridblocks neighboring the two-phase gridblocks, instead of the whole undersaturated area, will turn into two-phase blocks.

The maximum allowable time step is set to 31 days for all cases. However, the smaller grid size is, the more severe the saturation changes, the more difficult the convergence will be. So, in the computation process, the time step size has to be cut when convergence fails. For the PEBI-Size2 model, the number of total time steps is 605, while for the PEBI-Size8 model, the number of total time steps is 107. With more time steps, the PEBI-Size2 simulation could catch the gridblocks under phase transition more precisely.

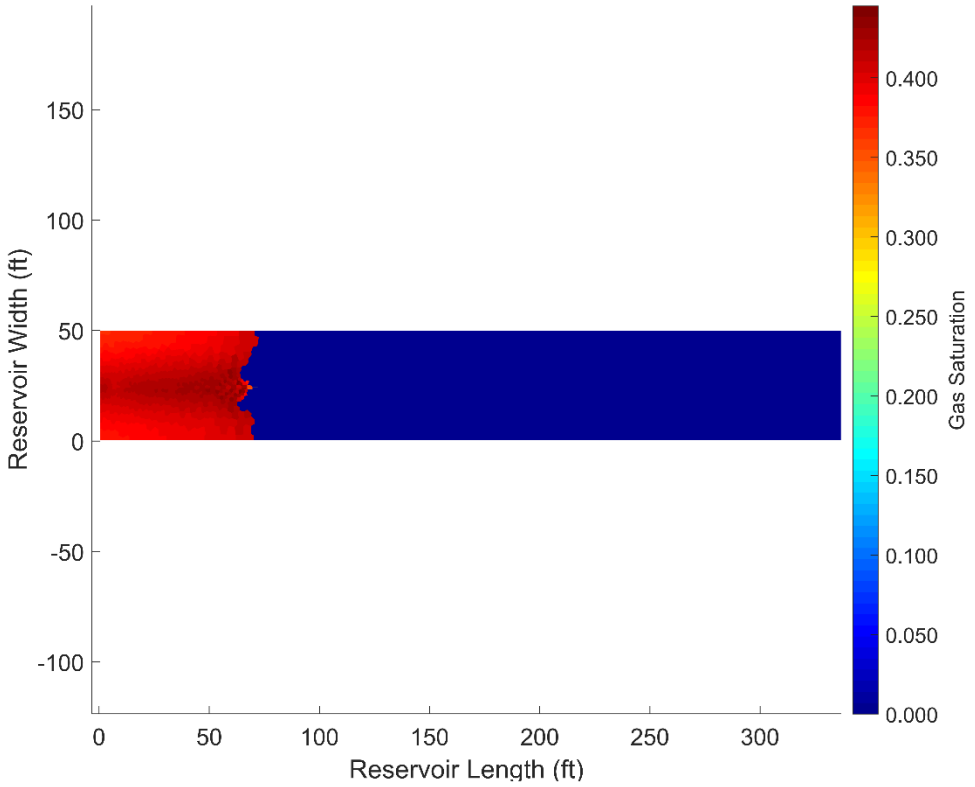

Fig. 10—Gas saturation map of the PEBI-Size8 model at 243 day.

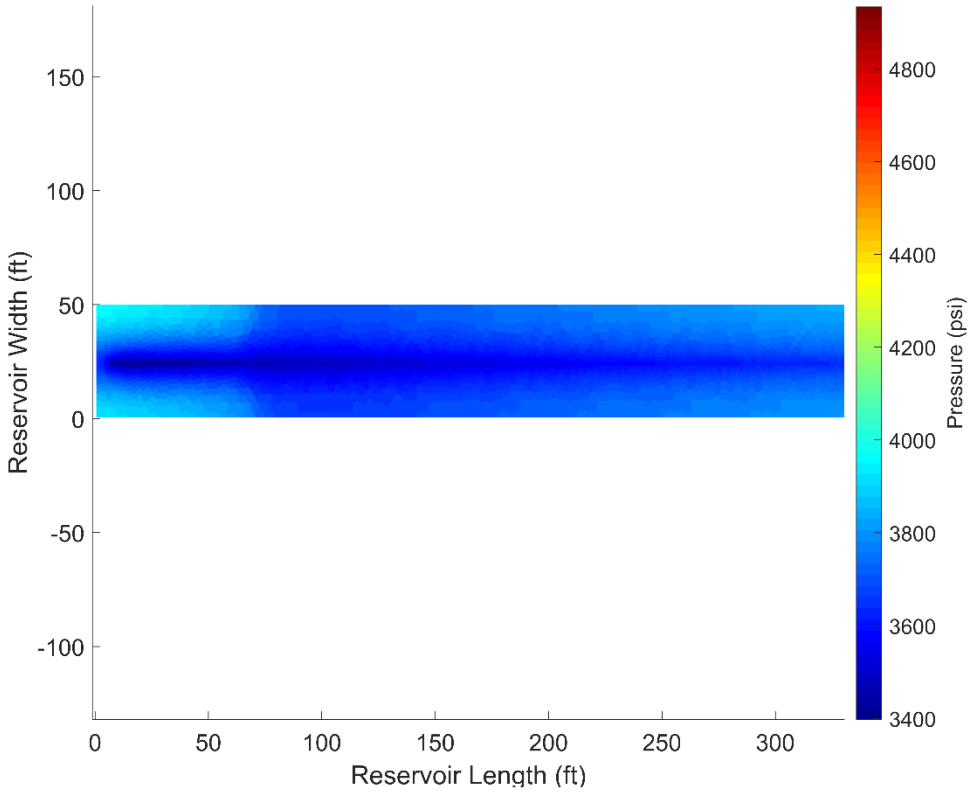

Fig. 11—Pressure map of the PEBI-Size8 model at 243 day.

To ensure the gridblock in transition being accurately captured, two methods are applied and compared. One method is to test more gridblocks for phase determination in each time step. The PEBI models with size 2 ft and size 8 ft are used to try with this option, and the cases are named Size2_Delta and Size8_Delta, respectively. DELTA is a Nexus phase transition test option that enables the gridblocks to be tested if they meet one of the criteria: (1) adjacent to two-phase gridblocks or single-phase blocks of another phase; (2) gridblock pressure decrease and/or mole fraction change exceed a specified small value. The other method to capture transition gridblock is to decrease the maximum time step size, so that the newly tested gridblocks could cover the pressure front in each time step. The PEBI model with size 8 ft is used to test the scenario with a maximum time step size of 5 days. The simulation results of cumulative oil production and GOR

are shown in **Fig. 12** and **Fig. 13**. The results of the Cartesian grid model and the original PEBI-Size2 model are also plotted as references. The CPU time used in each case is shown in **Fig. 14**.

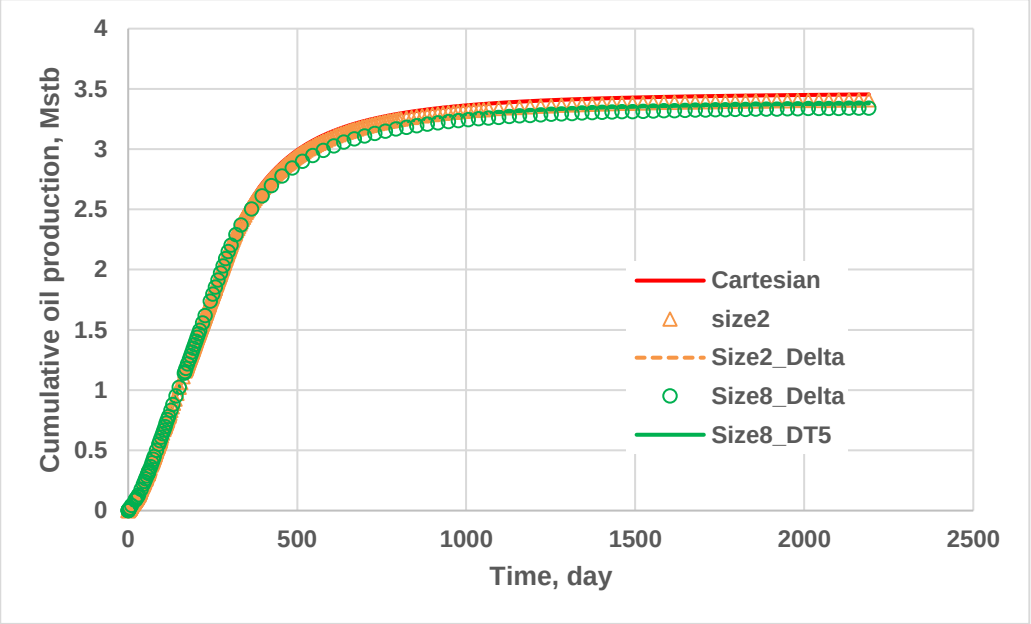

Fig. 12—Cumulative oil production of the Cartesian grid model, the original PEBI-Size2 model, the PEBI-Size2 and PEBI-Size8 models with DELTA option, and the PEBI-Size8 model with a maximum time step size of 5 days.

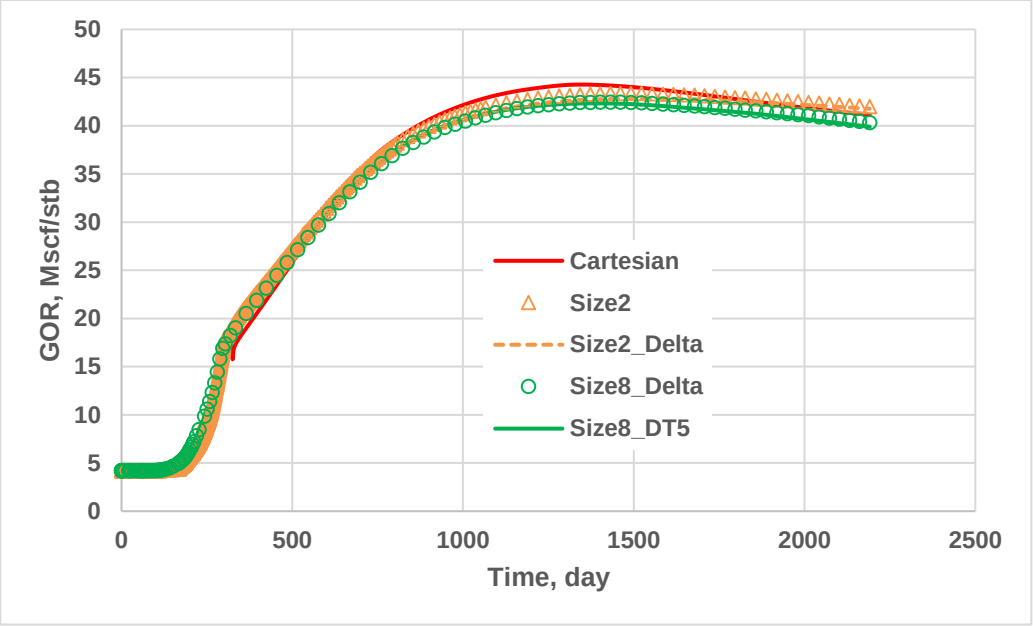

Fig. 13—GOR of the Cartesian grid model, the original PEBI-Size2 model, the PEBI-Size2 and PEBI-Size8 models with DELTA option, and the PEBI-Size8 model with a maximum time step size of 5 days.

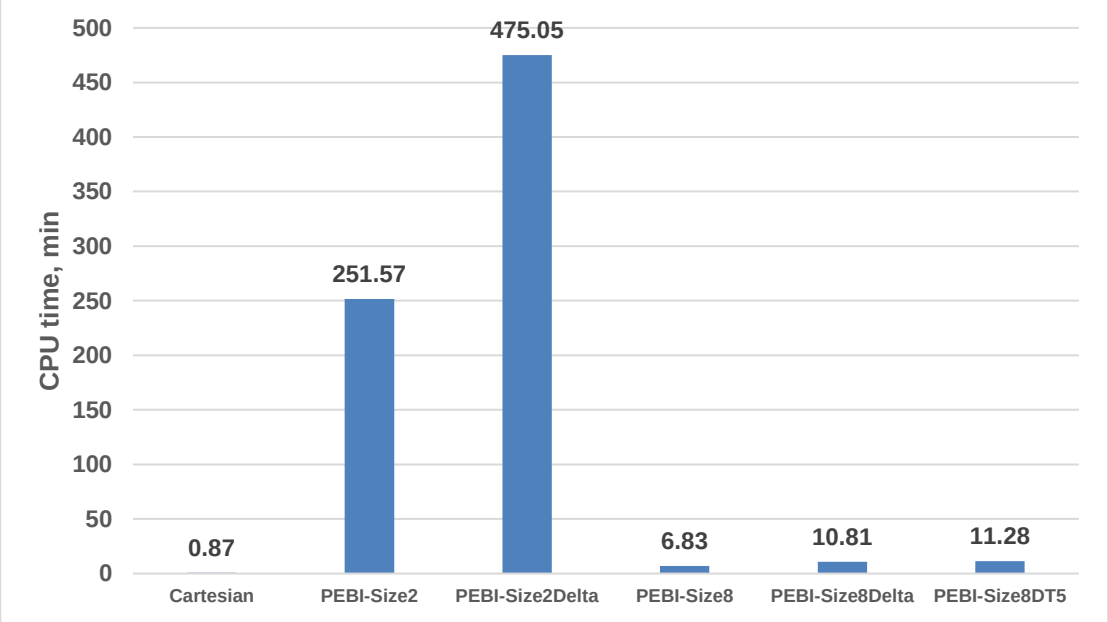

Fig. 14—CPU time used for each case.

The good match of the results indicates both methods can capture gridblocks under phase transition effectively. Comparing the results of the DELTA case and the case with smaller maximum time step size run on the PEBI-Size8 model, the DELTA method is a little bit more accurate, because it is closer to the results of PEBI-Size2 models. Models with more gridblocks cost significantly more computation time. Conducting transition calculation on larger number of gridblocks or using smaller time step size will generally consume 1.6~1.9X computation time of the original setup. DELTA option needs slightly less time. Considering the dramatic pressure change and the complex fracture networks with high fracture density, it is recommended to use fewer gridblocks with smaller time step size or DELTA option to assure simulation accuracy and save computation time. DELTA option is used for the simulations in the following chapters.

2.3 Theory of Phase Behavior Simulation

2.3.1 Diffusion

Common numerical approaches neglect the thermodynamic process of diffusion at the gridblock level. Instead, the assumption of local equilibrium of chemical potential is made (Hoteit 2011). It is reasonable for processes of two-phase depletion or gas injection in high permeability media, because both eddy diffusion caused by convection (pressure difference) and molecular diffusion caused by chemical potential (concentration difference) could take effect to achieve the equilibrium in a relatively short time. The former mechanism is more significant.

Diffusion coefficients in porous media are usually smaller than those measured in open space. They depend on the tortuosity, porosity, and constrictions of the porous media. The ratio of

diffusion coefficients in porous media is commonly between 0.15 and 0.7. Molecular diffusion in gas huff-n puff in tight rock will be further discussed in Chapter VI.

2.3.2 Phase Equilibrium

Given the fluid composition and temperature, the saturation pressure is determined and could be calculated by EOS during the simulation. Saturation pressure is the pressure at which the fluid mixture is at equilibrium phase with an infinitesimal amount of an incipient phase. The component fugacity in each phase is used as a criterion to determine the equilibria. The physical meaning of fugacity of a component i in vapor/liquid phase is a measure of the potential for transfer of that component between phases, written as f_i^V or f_i^L. In the micro view, fugacity is a measure of the transport driven force of molecules caused by intermolecular force among molecules of the same species, and among molecules of one species and those of other species. On the macro level, the fugacity of one component in one phase is a function of component mole fraction (x_i for a liquid phase and y_i for a vapor phase), pressure (p), temperature (T) and compressibility factor (z). Coefficients of its function depend on the EOS model used, and are determined once the EOS input is given (Coats 1980; Fussell and Yanosik 1978). At equilibria of a specified temperature T, as a result of mass transfer by convection and molecular diffusion, the chemical potentials of each component in vapor and liquid phases are equal:

$$\boldsymbol{f_i^V = f_i^L}, \mathrm{i} = 1,2,\ldots,\mathrm{N} \quad \ldots\ldots \textbf{Eq. 1}$$

In which

V means vapor;

L means liquid;

i is the component;

N is the number of components.

Since the composition of the initial phase is known, for example, (x_1, x_2,…x_N), and z is a solution of EOS with known variable T and unknown variable P, the only unknown variables are (y_1, y_2,…y_N, P). **Eq. 1** contains n equations. And one more equation is needed to solve the n+1 unknown variable:

$$\sum_{j=1}^{N} y_j = 1 \quad \text{..... Eq. 2}$$

The solution of P is the saturation pressure P_{sat}.

CHAPTER III

COMPARISON BETWEEN DFN MODEL AND DUAL-POROSITY MODEL ON DEPLETION SIMULATION

3.1 Validation of the Single-Porosity Model on a Reservoir with Single Hydraulic Fracture

Dual-porosity (DP) methods are widely used in commercial simulators such as CMG and Eclipse. The computation approach is based on the "Sugar Cube" conceptual model (Warren and Root 1963). The Warren and Root (WR) DP method attempts to solve the fluid flow problem for such conceptual model, but it is not an accurate solution due to some simplifications. On the other hand, the DFN method with PEBI grid is able to give a more accurate solution to the same conceptual model, because it explicitly models the fracture network. Before identifying the limitation of the WR DP method, this section begins with a comparison of the analytical method, the single-porosity method and the DFN method. The purpose of this is to tune the black-oil PVT and check the reservoir setup, making sure the reservoir models built for CMG and Nexus have the same properties. **Fig. 15** shows the CMG model of the single-hydraulic-fracture reservoir with single-porosity matrix. The grid system used is Cartesian. **Fig. 16** shows the Nexus model for the same reservoir setup, while the grid system is unstructured (PEBI).

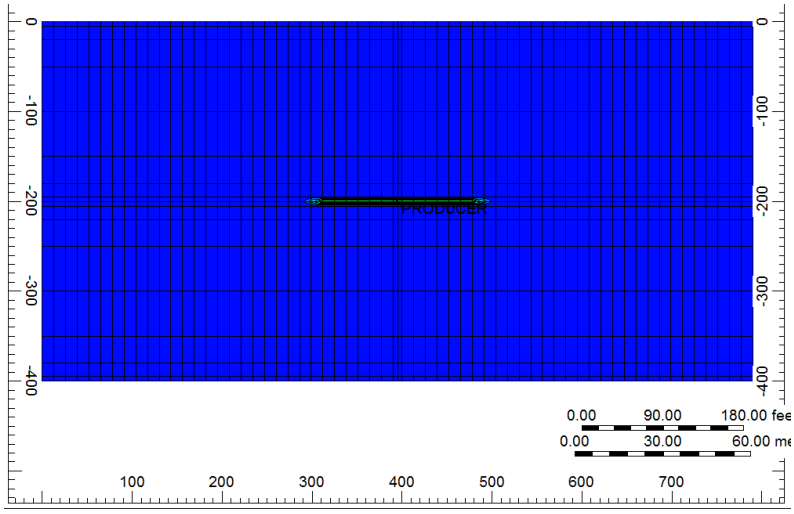

Fig. 15—the Cartesian grid of the single-hydraulic-fracture single-porosity model.

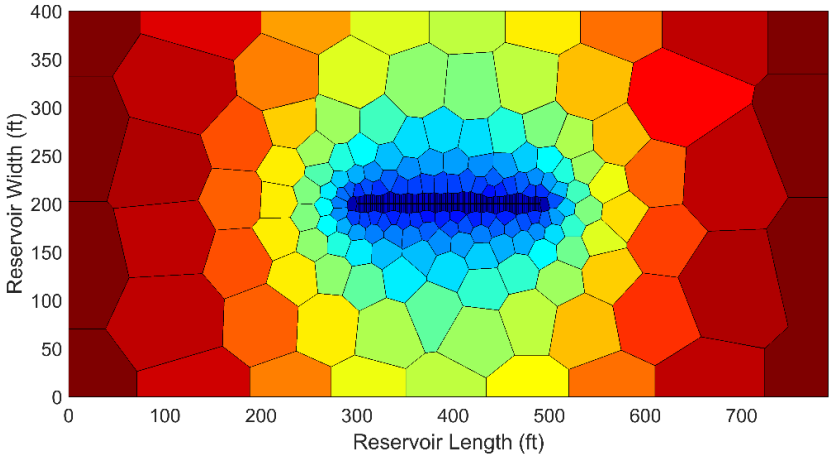

Fig. 16—the PEBI grid of the single-hydraulic-fracture single-porosity model.

The scenario is to produce oil from the single-hydraulic-fracture at a constant rate. The BHP results of the CMG Cartesian grid model, the Nexus PEBI grid model, and the Kappa analytical model are shown in **Fig. 17**. The good match of them confirms that the input of these two numerical simulation models is correct.

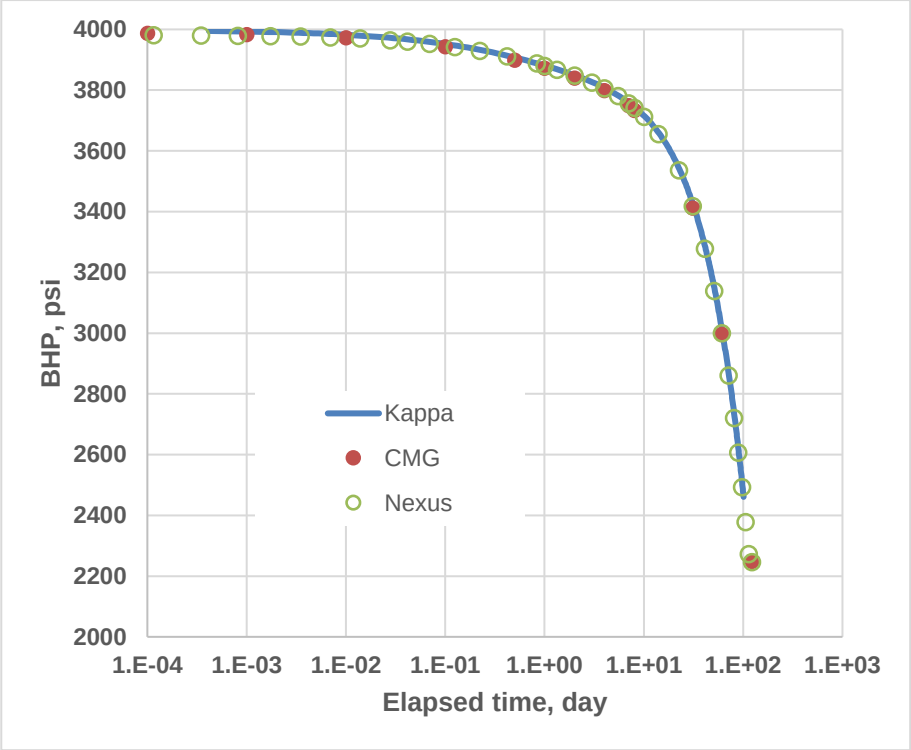

Fig. 17—Comparison of the results from the Kappa analytical method, the CMG Cartesian grid model and the Nexus PEBI grid model for the single-hydraulic-fracture single-porosity reservoir.

3.2 Comparison of the Dual-Porosity Method and the DFN Method on Continuous Natural Fracture Network

With the same PVT and reservoir dimensions as those used in the previous single-porosity models, a single HF model with dual-porosity matrix was generated with the Cartesian grid (**Fig. 18**). The "matrix" contains natural fractures and intact matrix. Accordingly, a single HF model with discrete perpendicular NFs was generated with the PEBI grid (**Fig. 19**). The spacing of NFs is 40 ft in the horizontal plane. Equivalent fracture permeability is calculated for the DP models, according to the fact that cross area of fracture gridblock is the same as that of matrix grid block. The equivalent natural fracture spacing is also adjusted by a multiplier of 1.065, since the shape factor of the WR method is not correct in comparison to the true solution of its conceptual model (Syihab 2009).

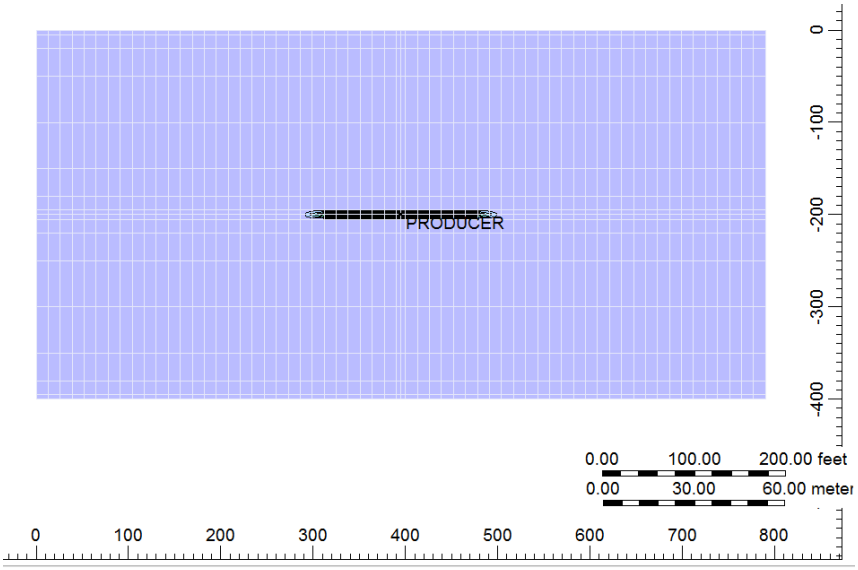

Fig. 18—The Cartesian grid of the single-hydraulic-fracture dual-porosity model.

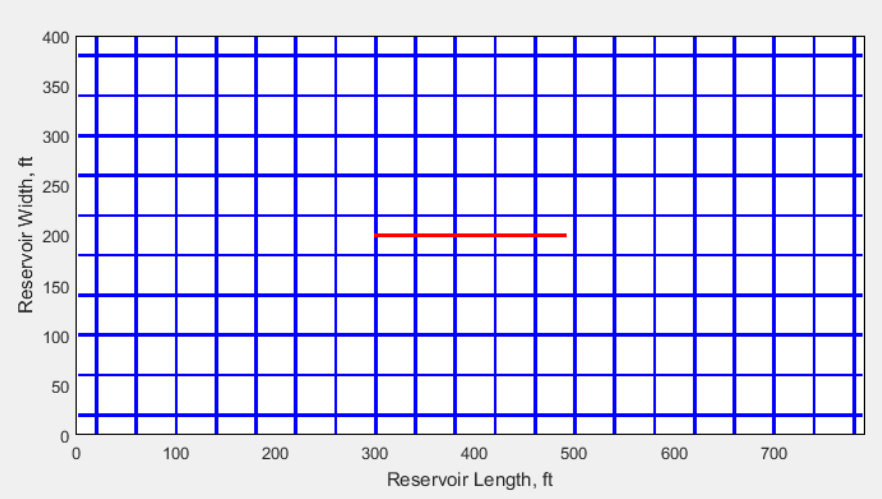

Fig. 19—The DFN of the single-hydraulic-fracture model with discrete NFs.

Simulation results of depletion on the fracture system alone are shown in **Fig. 20**, including BHP and pressure derivate. NFs have a permeability of 100 md, while matrix has 0 md permeability. The results of these two methods match well. This scenario is equivalent to a single-porosity model.

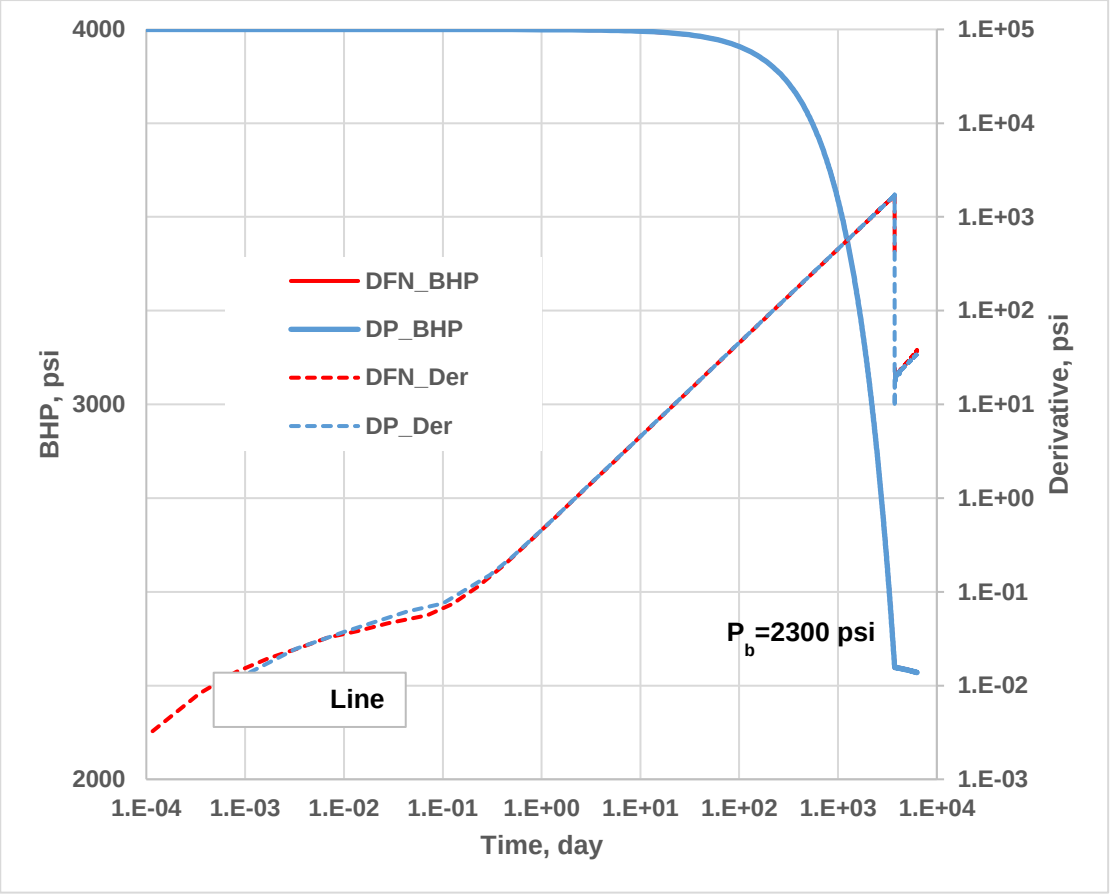

Fig. 20—Simulation results of the fracture system only.

When the matrix has a permeability of 10 nd, BHP becomes much higher due to the oil contribution from the matrix (**Fig. 21**). The BHP results still match well. But the derivative is different in the time range from approximately 0.01 ~ 300 days. This is because the matrix-NF flow in the WR dual-porosity method is treated as pseudo-steady state (PSS) flow. The transient flow incurred in the early stage is not considered. On the other hand, the DFN model can capture this feature. Therefore, the derivative of the DFN model results in a smoother curve.

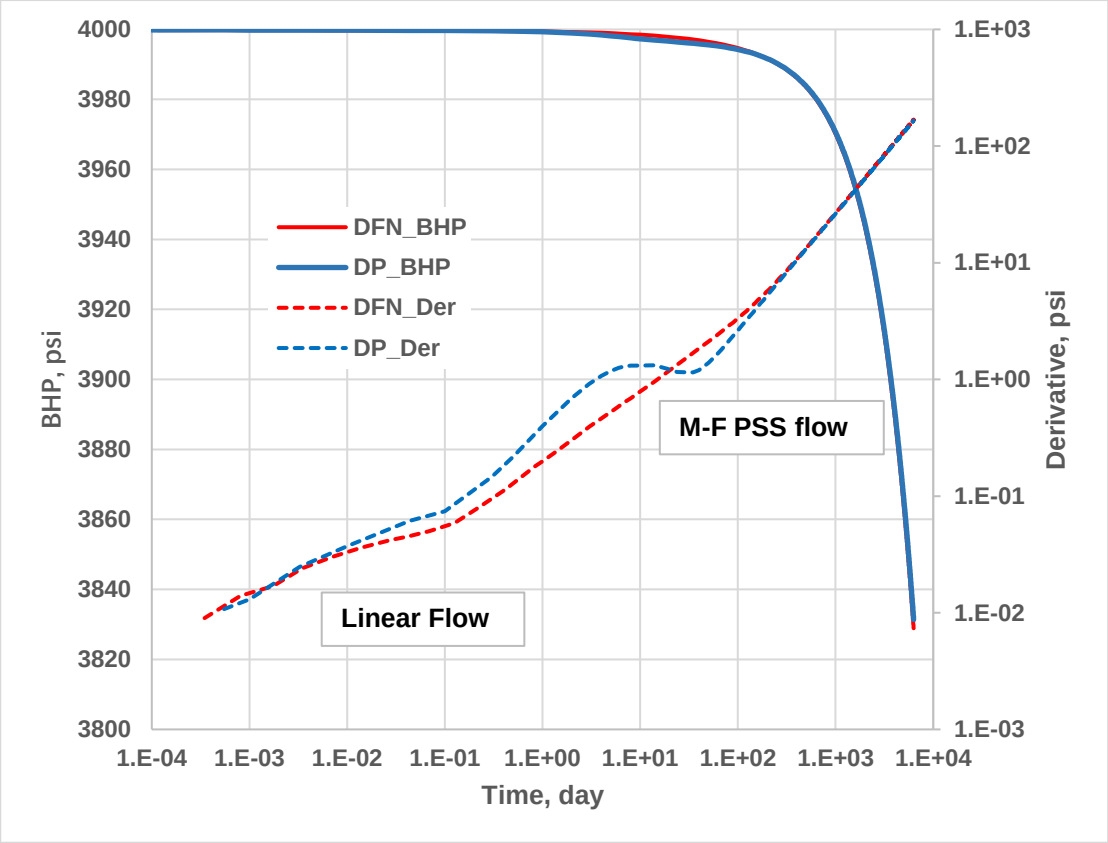

Fig. 21—Simulation results of the single-hydraulic-fracture dual-porosity model with Km=10 nd.

Another comparison is conducted on a model with a smaller matrix permeability of 1 nd. The results are shown in **Fig. 22**. There are obvious differences in both BHP and pressure derivative within the period of 0.001 ~ 1580 days.

After the mismatch period, BHP and pressure derivative match very well for the two methods for both cases of K_m=10 nd and K_m=1 nd. It is because during this late period, the flow mechanism of fracture-matrix is PSS flow for both the two methods (**Fig. 23**), and the previous cumulative production is the same. Thus, the two methods should have exactly the same behavior. Before this, the matrix-fracture flow in DFN model is transient flow (**Fig. 24**). Therefore, in the DP method, the matrix-fracture flow rate is "insufficient" due to the PSS assumption, so the BHP

of the DP method needs to decrease more sharply to honor the constant production rate. After a while, the BHP of the DP method needs to turn to the BHP of the true PSS matrix-fracture flow, which should coincide the BHP of the DFN method in the late period. As a result, BHP of the DP method during this transition period needs to decrease slowly, leading to a dip in the pressure derivative plot.

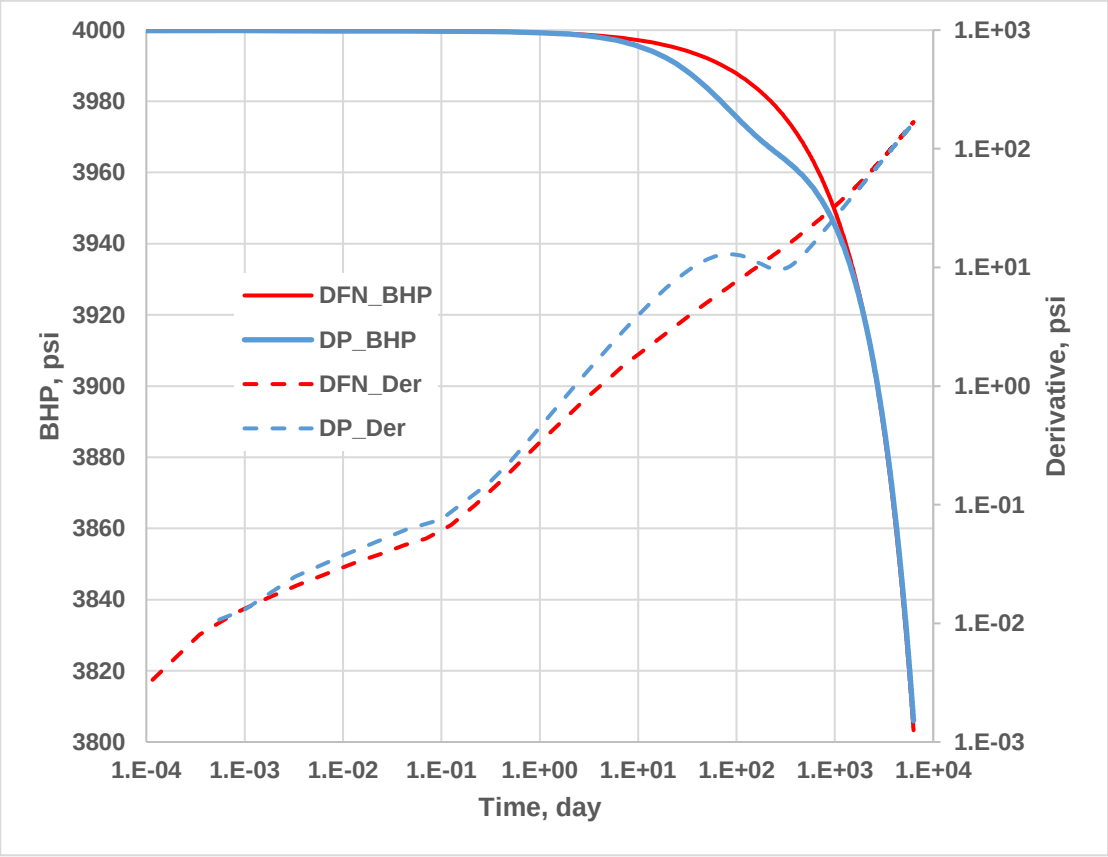

Fig. 22—Simulation results of the single-hydraulic-fracture dual-porosity model with Km=1 nd.

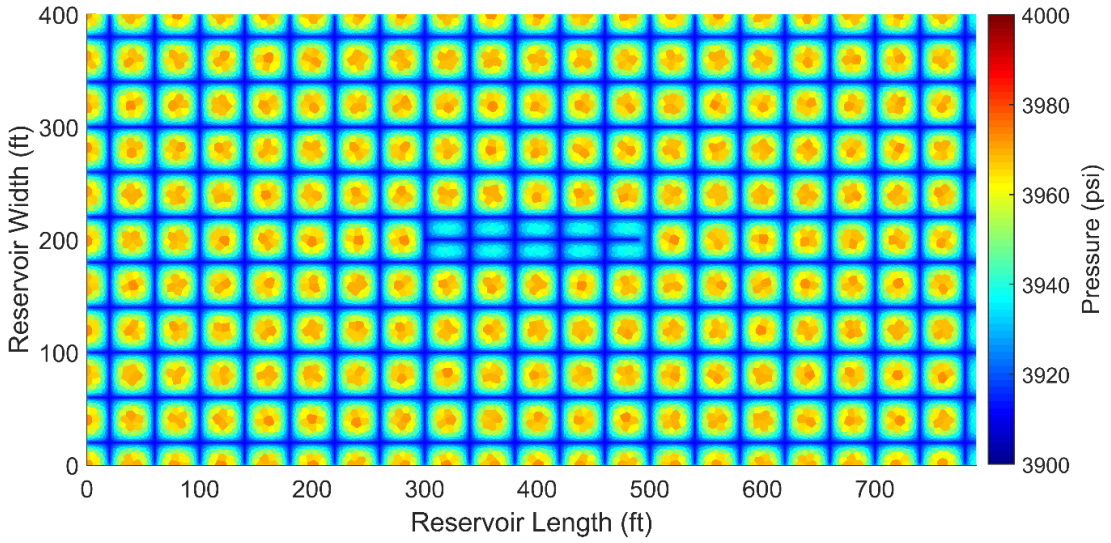

Fig. 23—DFN pressure map at 2283 day. It is a PSS flow between natural fracture and matrix.

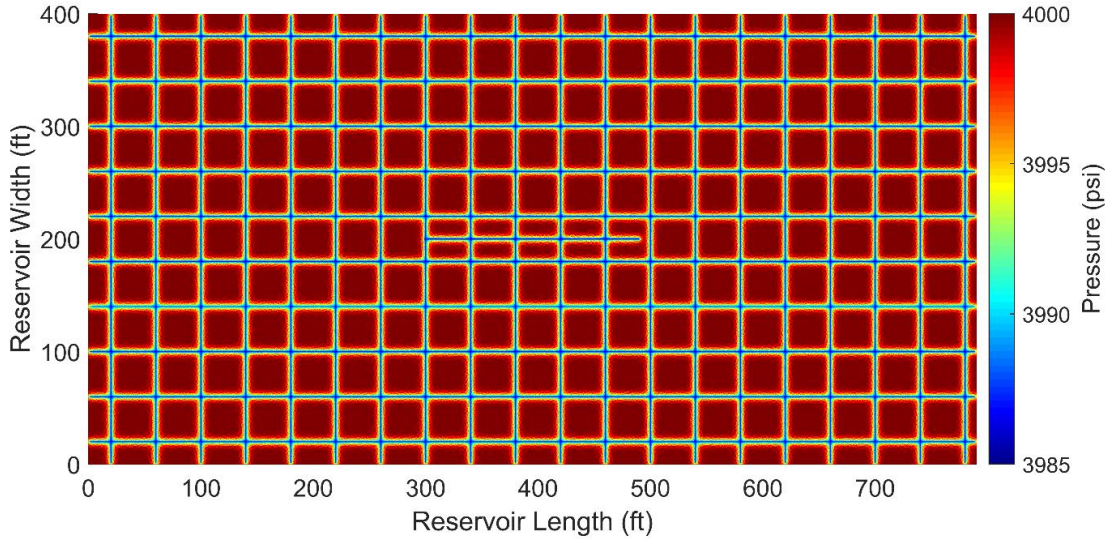

Fig. 24—DFN pressure map at 122 day. It is a transient flow between natural fracture and matrix.

The dip in the pressure derivative plot comes later for the DP method with K_m = 1 nd, compared to that for the DP case with K_m=10 nd. And so does the coincidence point of the BHP. This is because if the matrix permeability is small, the transient period of matrix-fracture flow is long, and the true PSS comes late. The timing of coincidence can be approximately estimated by:

$$t_{pss} \approx 1200\frac{\emptyset\mu c_t r_e^2}{k} \quad \textbf{Eq. 3}$$

In which

t_{pss} is the beginning time of PSS flow, hr;

$\emptyset$ is the matrix porosity, dimensionless;

μ is the oil viscosity, cp;

c_t is the total compressibility, psi^{-1};

r_e is the reservoir radius, but using half of the natural fracture spacing here, ft;

k is the matrix permeability, md.

The value used to calculate t_{pss} is shown in **Table 1**. For the matrix permeability of 10 nd, t_{pss} is 254 day. From **Fig. 21**, the coincidence time is around 230 day. And for matrix permeability of 1 nd, t_{pss} is 2541 day. From **Fig. 22**, the coincidence time is around 2000 day. The calculated value is a little bit higher, since **Eq. 3** is originally for radius flow. t_{pss} could be used to estimate the mismatch period as a result of the PSS assumption of DP models.

Parameters	Value
∅	0.109
M, cp	0.291402
c_t, psi^{-1}	4*10^{-6}
r_e, ft	20

Table 1—Reservoir parameters for the calculation of t_{pss}.

For natural fracture permeability as high as 100 md, the fracture conductivity is considered as infinite compared to the matrix permeability of the tight rock. Therefore, almost all the fluid in the matrix flows to the hydraulic fracture through the natural fractures. However, if the natural fracture permeability is small, the natural fracture conductivity is finite. Hence flow among matrix blocks, which crosses the fractures, will play a more important role. Cases with NF permeability of 0.01 md are run by the DFN method, the DP method, and the dual-porosity dual-permeability (DPDK) method. Four combinations of NF spacing of 40 ft and 10 ft, and matrix permeability of 10 nd and 1000 nd are tested. The BHP results are shown in **Fig. 25**. The DFN method is considered as a benchmark here because it can capture all the flow regimes. From **Fig. 25(a)** we can see that if the NF spacing is big and matrix permeability is small, BHP for the DP method does not match well. Moreover, there is also a mismatch of BHP for the DPDK method caused by its assumption of matrix-fracture PSS flow. But the results of the DPDK method is more accurate, compared to those of the DP method.

When we compare the models with same NF spacing, **Fig. 25**(a) vs (b), and **Fig. 25**(c) vs (d), it is obvious that the DP method could not get a correct result if the matrix permeability is high, which leads to strong matrix to matrix flow. Compare **Fig. 25**(a) and **Fig. 25**(c), and we can see the DP method and the DPDK method work better for reservoirs with small NF spacing. If the

matrix permeability is high and NF spacing is small, both the DP method and the DPDK method could give accurate results for this depletion scenario.

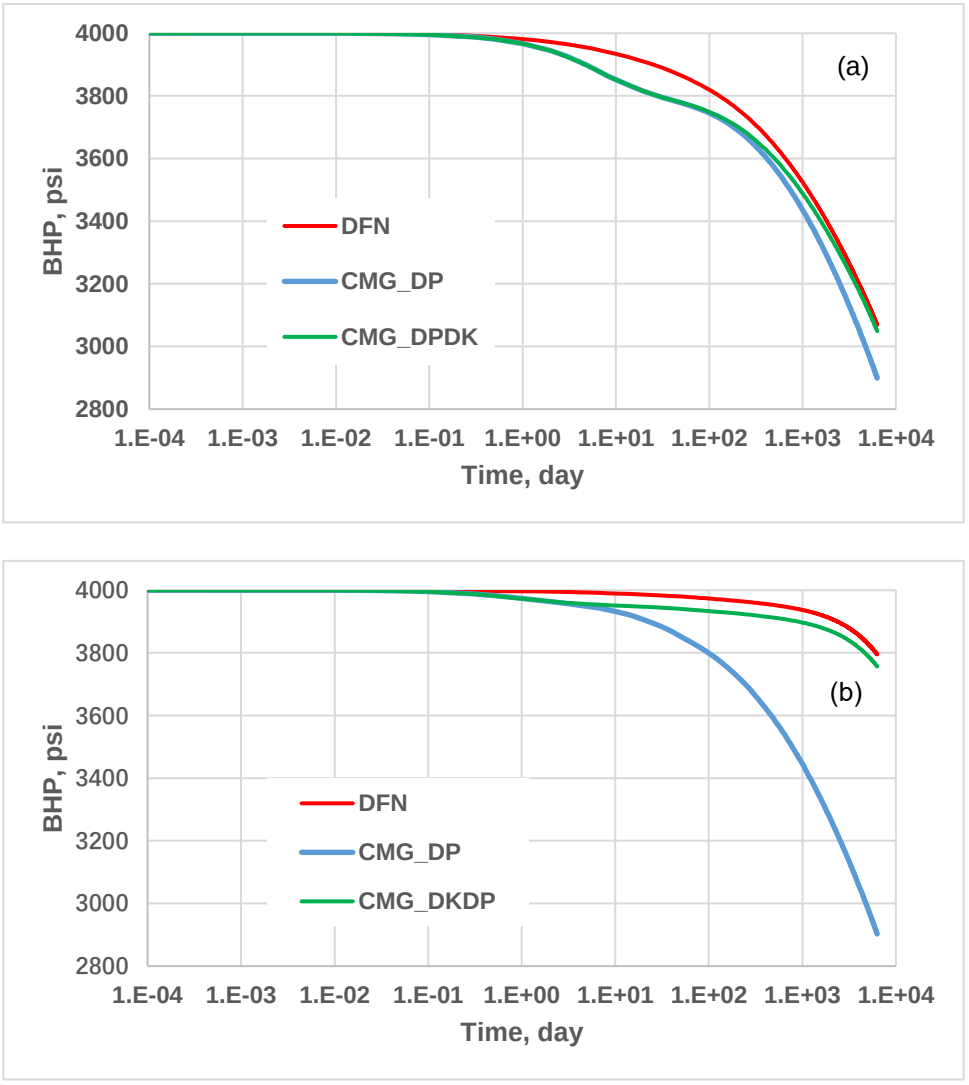

Fig. 25—BHP results of models with NF permeability of 0.01 md. (a) Matrix permeability is 10 nd, and NF spacing is 40 ft; (b) Matrix permeability is 1000 nd, and NF spacing is 40 ft; (c) Matrix permeability is 10 nd, and NF spacing is 10 ft; (d) Matrix permeability is 1000 nd, and NF spacing is 10 ft.

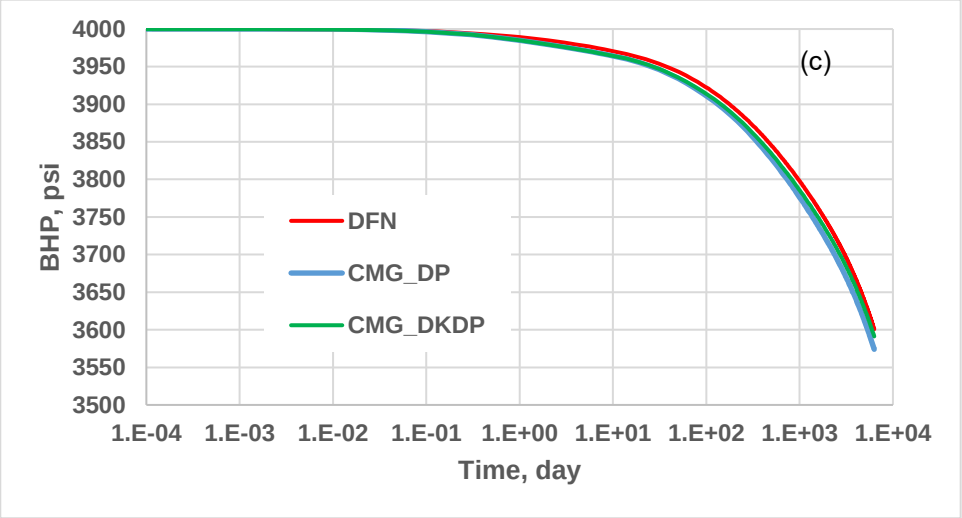

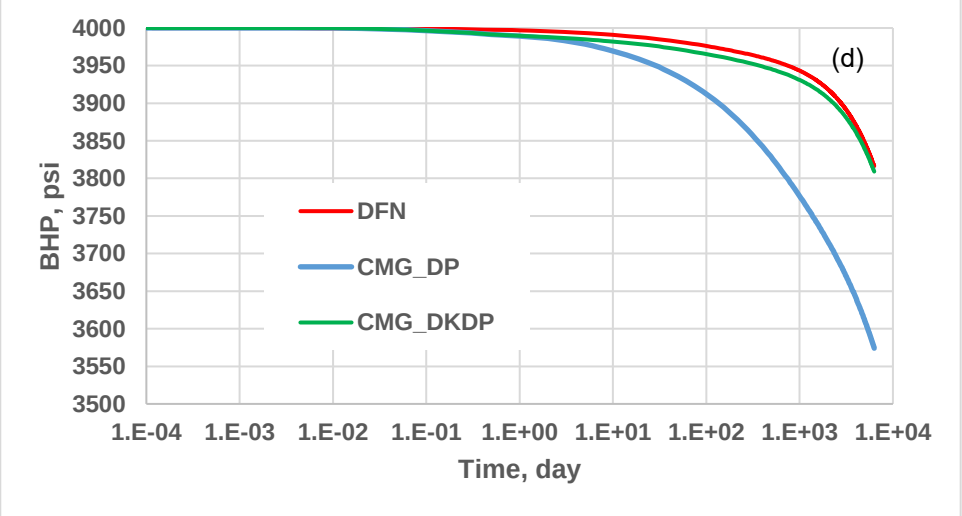

Fig. 25—Continue.

3.3 Comparison of the Dual-Porosity Method and the DFN Method on Discontinuous Natural Fracture Network

The cases in the previous section are based on the DP conceptual model, which contains perfect continuous NF. But in fact, the NF system has extensive discontinuity in different types (Belayneh and Cosgrove 2004; Gale et al. 2014; Lei et al. 2017), shown in **Fig. 26** 错误!未找到引用源。. To study the applicability of the continuum methods (DP and DPDK) for fractured reservoirs with discontinuity, a single-HF model with interruptions on NFs is built (**Fig. 27**). In E-W direction, the length of each NF is 80 ft, and the distance between every two neighboring NFs' head and tail is 2 ft. NFs in N-S direction are kept continuous. The NF spacing is 40 ft.

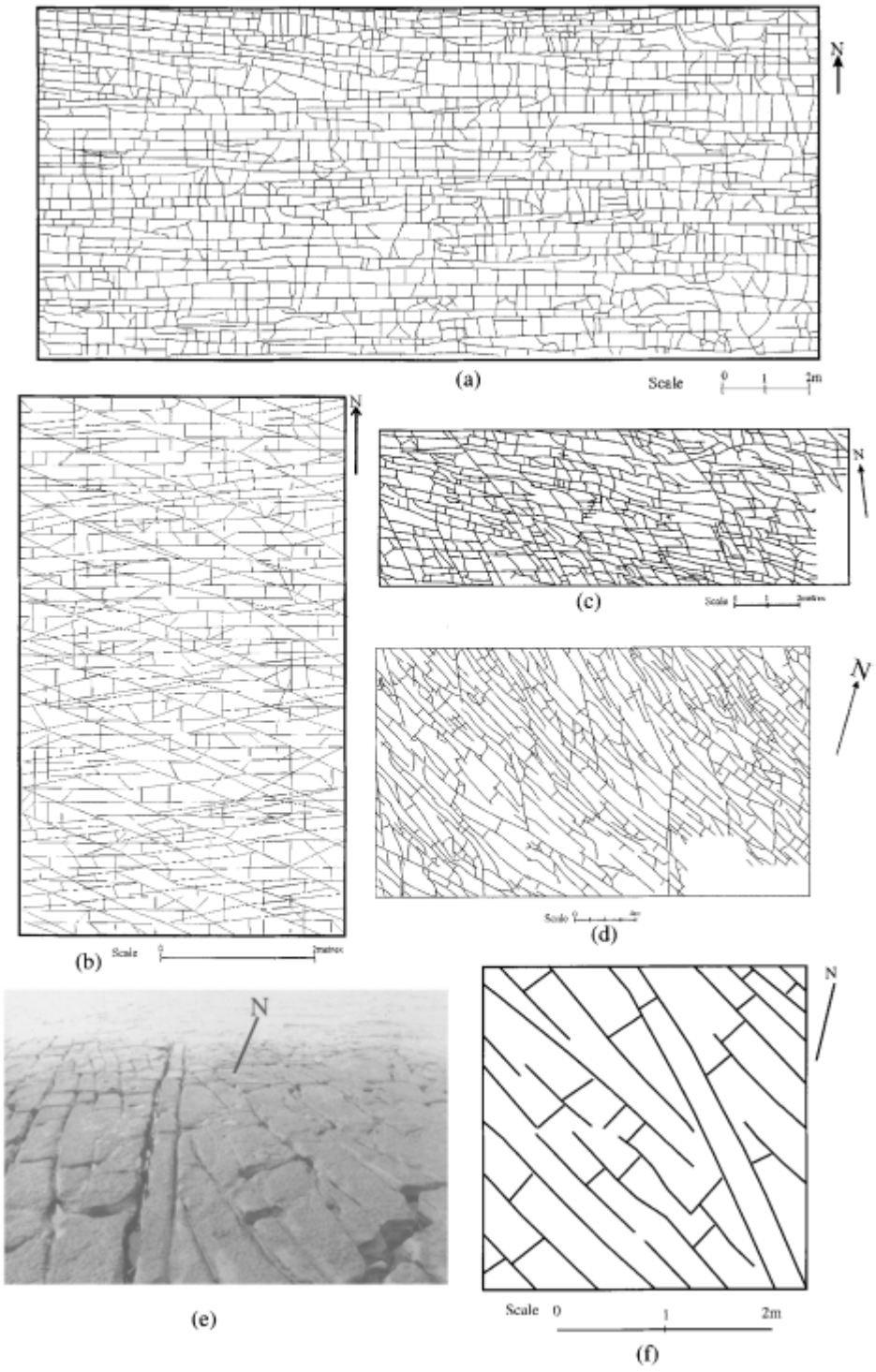

Fig. 26—Outcrop maps of limestone at the south margin of the Bristol Channel Basin, UK

Reprinted from the paper by Belayneh and Cosgrove (2004).

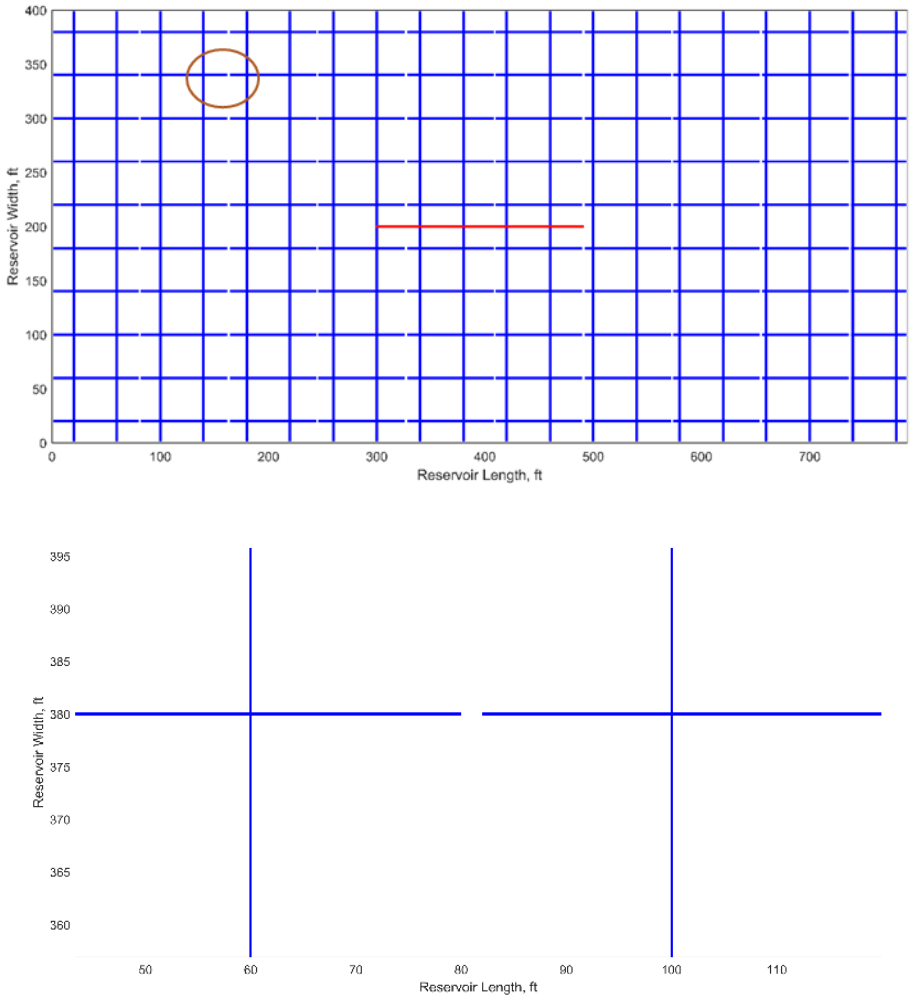

Fig. 27—The reservoir model with 2-ft interruptions. Upper: the full view of the reservoir; Lower: zoom-in of the discontinuity.

Three scenarios with different reservoir property combinations are tested on this discontinuity model by the DFN method: (a) NF permeability = 100 md, matrix permeability = 10 nd; (b) NF permeability = 100 md, matrix permeability = 1000 nd; (c) NF permeability = 0.01 md, matrix permeability = 1000 nd. Additionally, the same scenarios are also run on the continuum model with the DFN method and the DPDK method, containing no interruption in natural fractures. BHP results are shown in **Fig. 28**. From **Fig. 28(a)**, we can see the discontinuity in NF significantly affect the depletion behavior if matrix permeability is low (10 nd). If the matrix permeability is

relatively high (1000 nd), the results are close (**Fig. 28(b)**). Especially when NF permeability is low, i.e., the permeability contrast between NF and matrix is small, the behavior of the continuity case and the discontinuity case are even closer (**Fig. 28(c)**).

Note that the discontinuity model used here is a simplified one. The real underground fracture networks could be more complex and the density distribution is uneven, especially after hydraulic fracturing, which will be shown in Chapter V. In general, when the permeability contrast is small, and the discontinuity distance is small, the DPDK method could be feasible for the depletion simulations.

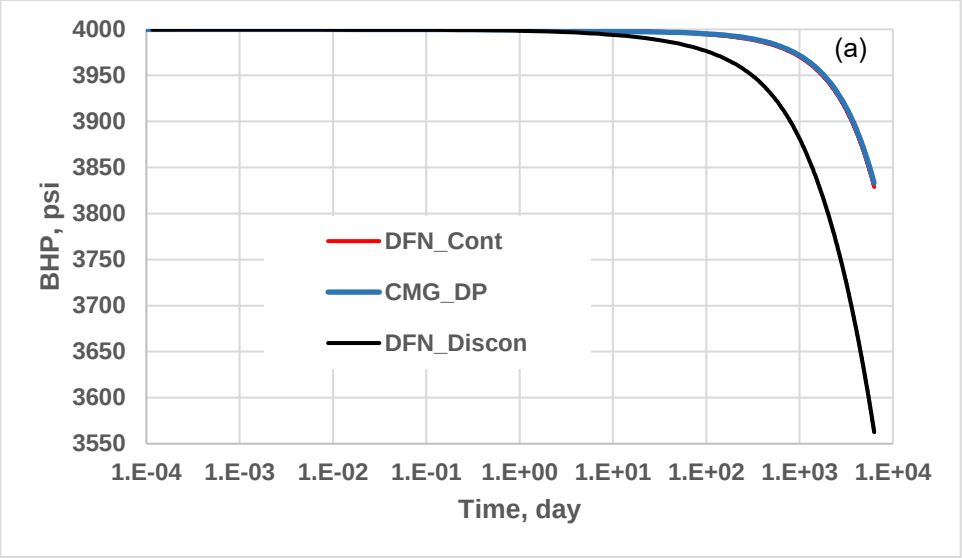

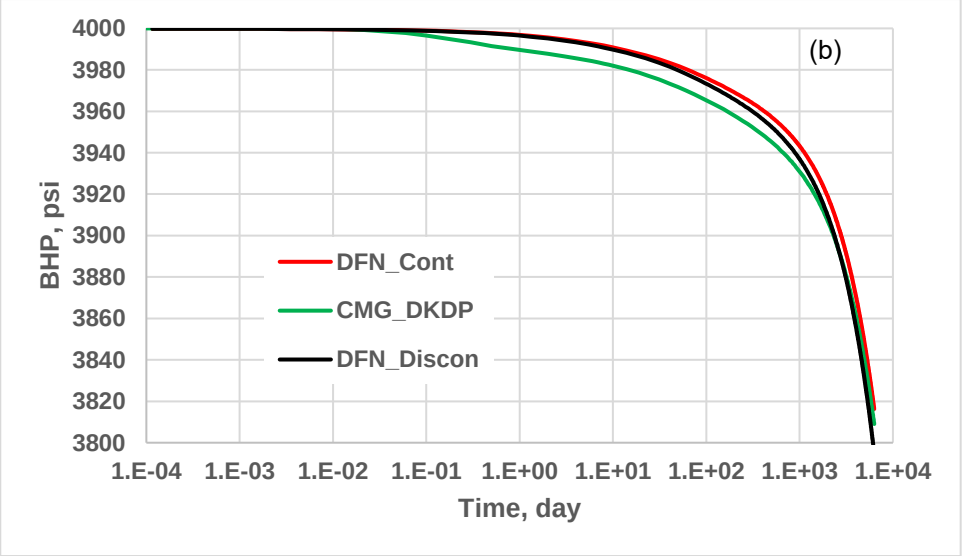

Fig. 28—BHP results of models with discontinuity. (a) Matrix permeability is 10 nd and NF permeability is 100 md; (b) Matrix permeability is 1000 nd and NF permeability is 100 md; (c) Matrix permeability is 1000 nd and NF permeability is 0.01 md.

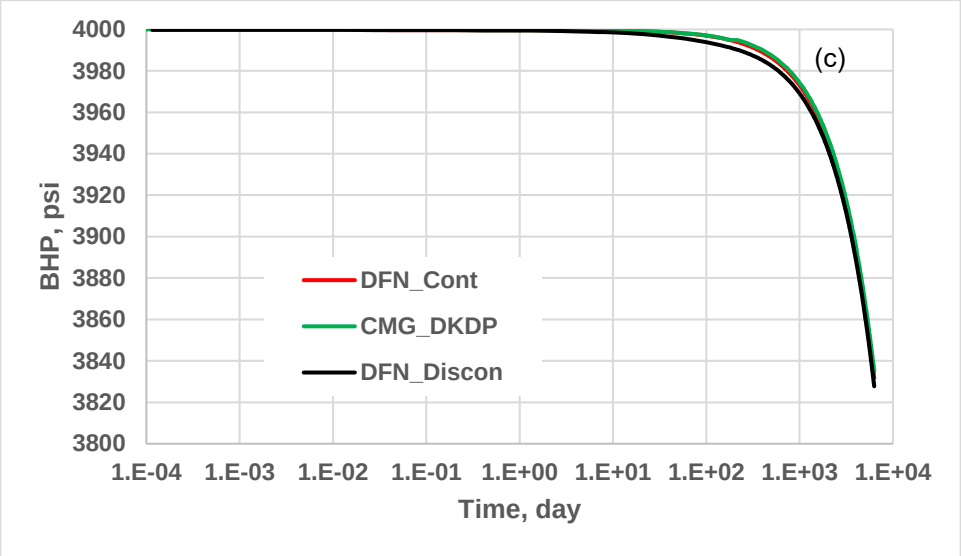

Fig. 28—Continue.

CHAPTER IV

GENERATE A DFN MODEL WITH MICROSEISMICITY AND CALIBRATE IT WITH HISTORY DATA

In this section, data of a multistage hydraulically fractured horizontal well is used to generate DFN and calibrate the corresponding reservoir model. This well was placed in the Spraberry formation in Permian basin. Data shared by the operator contains microseismicity, core observation, and production rate and pressure. Workflow is described below about how to utilize these operator's data and public information to build a reservoir fluid-flow model.

4.1 DFN Generation with Constrain of Stimulation Treatment Schedule

One of the advantages of DFN methods is that it can utilize available field data to generate the geometry and properties of fracture networks with relatively accuracy. Sun et al. (2016a) proposed a workflow of semi-stochastic DFN generation with core observation data and microseismic (MS) data. The assumption for that method is that only one induced natural fracture passes through a microseismic event location, and all such natural fractures have probability to be propped during fracturing. Some of these natural fractures are connected to hydraulic fractures if they are in the way of the traveling tips of hydraulic fractures, and the connected natural fractures are propped by capturing and altering the propagation path of hydraulic fluid carrying proppant. An example of generated DFN, which contains connected natural fractures and hydraulic fractures, is shown in **Fig. 29**. This fracture network is able to transport hydrocarbon fluid to well perforations, and named as flow-producing DFN (FP-DFN). Nevertheless, in fact, not all the MS

anchored natural fractures have the same probability to be connected with the main hydraulic fractures and to be effectively propped. Thus, this approach has high uncertainty and an inaccurate description of a stimulated reservoir. This also increases difficulties in fluid flow simulation due to the numerous fracture segments. In this section, a workflow is proposed to screen the "effective" MS events by adding HF treatment schedule into account.

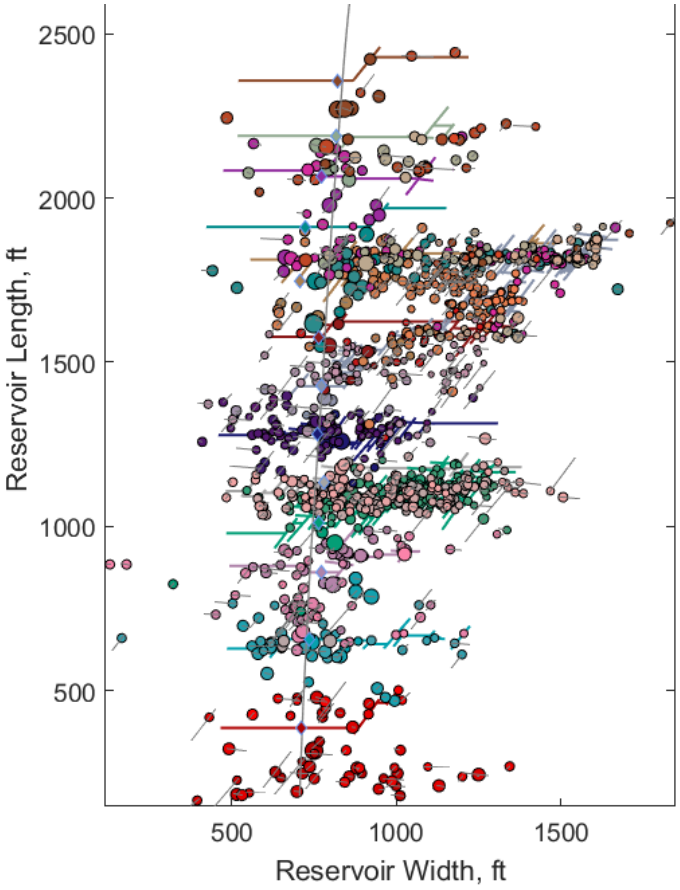

Fig. 29—An example of DFN generated in disregard of the hydraulic treatment schedule. This is for a 15-stage hydraulically stimulated well in the Spraberry Trend area.

4.1.1 Filtering Process of the Microseismic Events

The microseismicity incurred during hydraulic fracturing is an acoustic part of the energy release due to tensile failure, shear failure or mixed-type failure along planes of weakness in the rock (Batchelor et al. 1983). Most of such rock failures have shear nature (Warpinski et al. 2004). The most common failure criterion used in rock mechanics is the Mohr-Coulomb equation (Jaeger and Cook 1969). For fractured porous media with fluid saturated, it can be written as:

$$\tau_f = S_f + \mu_f(\sigma_f - p_f) \quad \text{Eq. 4}$$

where: τ_f = shear strength of the fracture;

S_f = cohesion of the fracture;

μ_f = friction coefficient along the fracture;

σ_f = normal stress acting on the fracture plane;

p_f = pore pressure within the fracture.

Let's consider this equation during hydraulic fracturing. The failure of natural fractures can be triggered by the stress field change caused by rock deformation ("dry" events). Such stress field change could be either increase of the shear stress along the fracture plane (τ_f), or decrease of the normal stress acting on the fracture plane (σ_f). The shear failure could also be triggered by the pore pressure (p_f) increase due to the leak-off of hydraulic fluid into the natural fractures ("wet" events). Moreover, the combination of the above mechanisms may also result in shear failure.

Numerical simulation of geomechanic model shows that at each time step, the microseismicity mostly exists around the hydraulic fracture tip or the expended hydraulic fracture (Nagel et al. 2012). Those events could propagate relatively further if the natural fractures are less

stiff (Garcia-Teijeiro and Rodriguez-Herrera 2014). However, the diffusion front of the MS events generally coincides with the hydraulic fracture tip propagation in the time domain (McKenna et al. 2016; Shapiro et al. 2009).

Several analytical models describe the propagation of hydraulic fractures. The PKN model was proposed by Perkins and Kern (1961) to compute fracture length and width with a fixed height, and improved by Nordgren (1972) by adding fluid loss effect. It assumes that fracture toughness could be neglected. Based on the PKN model, basically, the half-length r_f of the fracture (which is assumed symmetric in respect to the borehole) is approximately given as a function of the injection time *t* by the following equation:

$$r_f(t) = \frac{Q_I t}{4h_f C_L \sqrt{2t} + 2h_f w} \quad \text{..... Eq. 5}$$

where: Q_I = injection rate of the fracturing fluid (ft^3/min),

C_L = fluid leak-off coefficient (psi/$min^{0.5}$),

h_f = fracture height (ft), and

w = the fracture width (ft).

From the observation of the top view of the MS map of the stimulated well located in the Spraberry Trend area (**Fig. 29**), it is reasonable to use a 2D propagation model such as the PKN model, because the distribution of MS events in each stage has strong directionality. Since the tips of hydraulic fractures are the most powerful and fast-spreading sources to trigger the slippage at natural fractures, the front of the MS cloud should be around the tips, and only the MS events at the front representing natural fractures that possibly capture and altering the path of the tips, following by the proppant entering. So

Eq. 5 is used to identify the "effective" MS events, where locating natural fractures possibly propped and play an important role in fluid producing. On the other hand, the "ineffective" MS events may be numerous, but the natural fractures there are not propped, or even not invaded by hydraulic fluid.

It is simplified in this section that only one pair of fracture wings exist in each stage, although there are actually two clusters per stage for this well located in the Spraberry Trend area. Previous studies of numerical simulation and field observation indicate a heel-biased fluid and proppant distribution because of the premature cluster screenout near the toe clusters, as well as the stress shadow effect (Wheaton et al. 2016; Wu et al. 2017a).

The parameters used for

Eq. 5 are determined by the available field data, as well as the trial and error for an acceptable match of MS cloud front. The flow rate and elapsed time of treatment fluid are obtained from the report of the stimulation job. Propped fracture height should be less than the vertical dimension of the MS cloud (500 ft). A reference leak-off coefficient of 0.0012 $ft/min^{0.5}$ is summarized from a Lower Spraberry model, which is relatively high and unlikely to be a result of the matrix permeability obtained from core experiments (Barba and Cutia 1992). Width, leak-off coefficient, and height are considered the same for all the stages, and finally obtained through the match.

Fig. 30 (a)(c)(e) shows the tip propagation in PKN model matches the front of the MS cloud in stage 5, 6 and 13, respectively. The propagation starts at the beginning of hydraulic fluid entering the perforation and stops at the pump shutting down. The MS events within a distance of 50 ft from the propagation plot are considered effective and marked as black dots. Note that not all the natural fractures located at these effective MS events necessarily intersect with hydraulic

fractures and involve in the propped DFN. Generally, only fractures, which are near enough to the propagation path of HF and can fail at a favorable angle, will be propped by the entry of slurry. For our analysis, it is important to have the early MS events, since the "wet" events caused by leak-off are not spread far at the early time. Therefore, these early events illustrate the propagation path of the tips with high confidence. **Table 2** shows the parameters obtained by history match. Data from Barba and Cutia (1992) is listed for the sake of comparison.

Parameters	Matched Value	Value from Literature
Height (ft)	390	450
Final length (ft)	420-500	300
Width (inch)	0.3	-
Leak-off coefficient (ft/min^0.5)	0.001	0.0012
Qi, Flow rate of treatment fluid (bpm)	60	42-56

Table 2—The input parameters for PKN-type hydraulic fracture to screen MS events representing possibly propped natural fractures

4.1.2 Propped-DFN Generation with Material Balance of Proppant

A general rule for proppant entry is that the average fracture width is 2-2.5 times the average proppant diameter (Smith and Montgomery 2015). Thus, for 20/40 mesh proppant used in our case requires the entry width to be from 0.055 to 0.07 inch. However, the width of natural fractures in Lower Spraberry from core description ranges from 0.008 to 0.023 inch. So we can make an assumption that proppant could enter the natural fractures only if it captures the hydraulic tip and fracture fluid is altered into the new propagation path. On the other hand, natural fractures induced by stress field change or fluid leak-off from the intersected HF only can be assumed to be unpropped ("self-propped" shear fractures).

On the other hand, the numerical simulation indicates that the average velocity of proppant in the slurry is generally lower than that velocity of fracture fluid. The higher the volumetric concentration of proppant, the bigger the difference. At some critical concentration proppant particles touch each other and further proppant transport becomes impossible. This leads to a significant reduction in propped fracture lengths and heights compared to the dimension of hydraulically opened fracture (Blyton et al. 2015).

Thus, in this study, it is assumed that proppant will fill the DFN created by the hydraulic fluid tip and will partially fill natural fractures in direct connection to the main HF. The total mass of proppant pumped gives us a volume of the DFN which can be propped considering packing density of 95.6 lb/ft^3 for 20/40 sand. The propped fracture width is generally from 0.1 to 0.5 inch (McDaniel et al. 2009; Perkins and Kern 1961). Considering that the propped fracture should be narrower than the one predicted by PKN model, 0.24 inches is a reasonable approximation and used for this study. Similarly, the propped fracture height should also be smaller than the matched value, and 150 ft is used. These values are considered acceptable based on the history matched results in the following section. Further research should be done in HF simulators to improve our understanding.

To sum up, the effective MS events are screened by the match with PKN model for tip propagation, identifying the possible natural fractures that involved in the propped DFN, which is generated in a semi-stochastic approach the like previous study (Sun et al. 2016a). Additionally, such propped DFN is constrained by the proppant material balance. In other words, the modeled propped fractures stop propagation in the formation matrix or connected natural fractures when the proppant exhausts. It is assumed that only one induced natural fracture passes through each of the MS events, and the strike of these natural fractures follow the same distribution of that observed

in the cores. Fracture length is assigned by a power law distribution constrained by minimum, maximum and exponent. The input parameter for propped DFN generation is depicted in **Table 3**. Strike and intensity are summarized from core observation. The generated DFN for stage 5, 6 and 13 are shown in **Fig. 30 (b)(d)(f)**, respectively. For most of the stages, the effective MS events distribute more linearly compared to the whole MS cloud, which also indicates that the hydraulic fractures propagate semilinearly along the maximum horizontal stress even in the formation with highly developed natural fractures. The generated DFN for all 15 stages are shown in **Fig. 31**. It is clear that although the MS events are numerous, the effective events are limited and the propped DFN is relatively simple.

Parameters	Set 1 (N 35 deg. E)	Set 2 (E-W)
Mean Strike	35 deg.	90 deg.
Normalized Intensity Ratio	1.8	1
Fisher Parameter (k)	120	80
Minimum Fracture Length (lmin)	50 ft	50 ft
Maximum Fracture Length (lmax)	100 ft	120 ft
Power Law Exponent (α)	0.8	0.9
Propped Fracture Height	150 ft	150 ft
Propped Fracture Width	0.24 in	0.24 in

Table 3—The input parameters for stochastic natural fractures

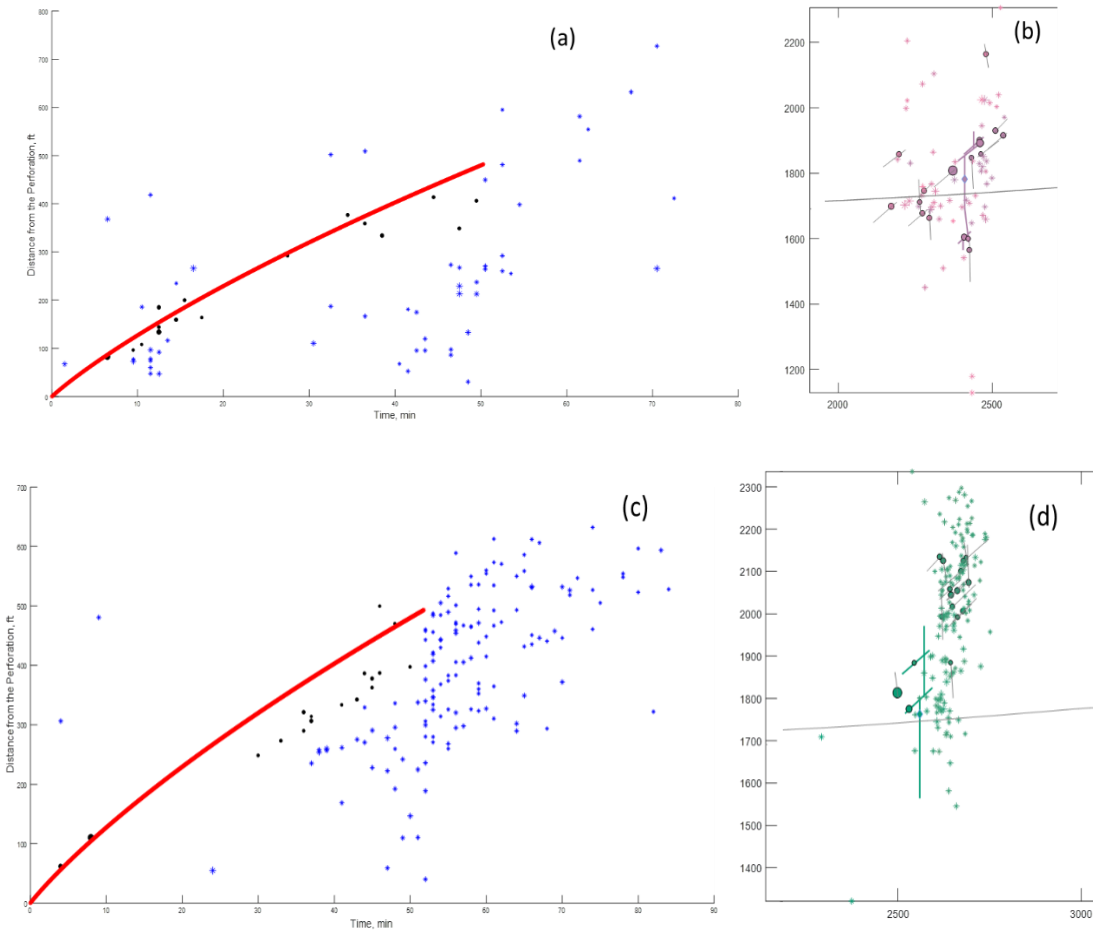

Fig. 30—(a)(c)(e) Spatial-temporal evolution of hydraulic fracture tips and MS events in stage 5, 6 and 13, respectively. Black dots: events near the traveling tip both spatially and temporally; Blue stars: events away from the tips; Red line: the propagation of tips. (b)(d)(f) The fluid-production DFN constrained by flited MS events and proppant volume. Dots: effective MS events; Stars: ineffective MS events.

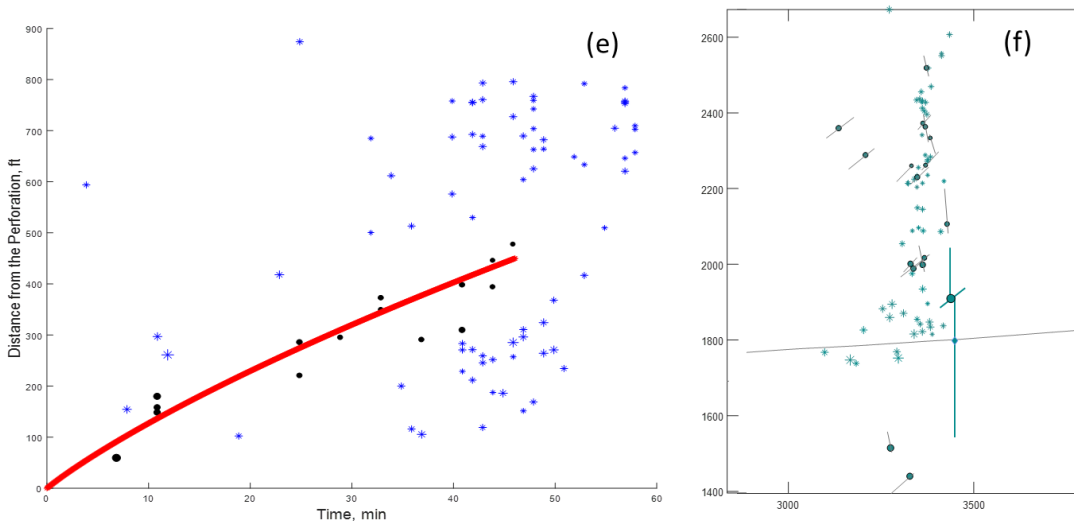

Fig. 30—Continue.

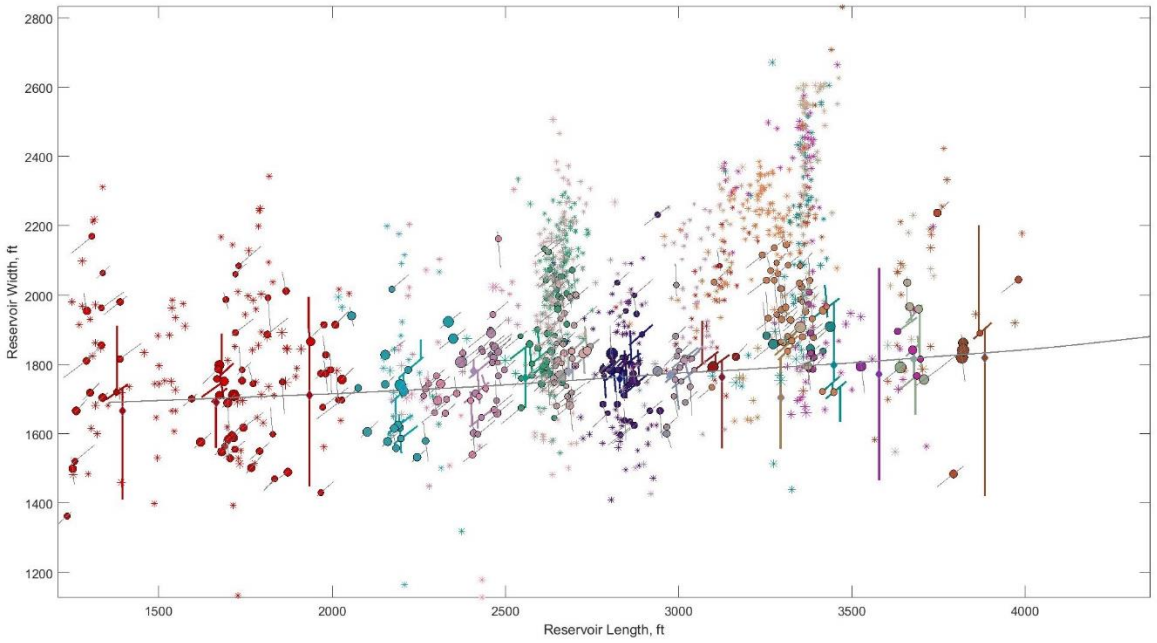

we

Fig. 31—Propped-DFN for the 15-stage fractured well.

History match is an effective method to verify the proposed method, and delivers a reasonable and reliable reservoir model representing the flow behavior. The available data for this well in the Spraberry formation is collected and processed with proper correlation to obtain necessary inputs for the simulation.

4.2.1 Reservoir Dimension and Rock Properties

Although the lease area and the number of wells drilled in the lease are known from the public reports, it is not easy to identify the drainage area of each well. A relatively large dimension is used to ensure the pressure maintenance for honoring actual or historical production rate. The depth, porosity and rock compressibility are gathered from the data provided by the operator. The pore pressure of Spraberry in Western Area ranging from 2000 to 2800 psi (Friedrich and Monson 2013), here an initial pressure of 3300 psi is assumed in consideration of pressure build-up during the shut-in period after fracturing treatment.

An average absolute permeability of 0.108 md for the matrix is obtained from core analysis, which agrees well with permeability correlated from porosity ranging from 0.16 to 0.18 md (Guevara 1988). Higher permeabilities of 0.36 to 6.9 md were observed when the Spraberry formation had initial reservoir pressure, which is a likely result of a superposition of natural fractures' permeability and matrix permeability (Dyes and Johnston 1953). The experimental study also showed that the unpropped fractures contribute much more than the rock matrix, but their conductivity is only 1 percent or less of that of propped fractures (Wu et al. 2017b). For this reason, the induced but not propped natural fractures are not involved in the propped DFN, but account

for an enhanced transmissibility of the matrix. Accordingly, a “matrix” permeability of 0.5 md is set for this history match. The properties of the reservoir matrix and the propped fractures are summarized in **Table 4**.

The propped fractures have a permeability of 3000 md and width of 0.02 ft in this model, resulting in a conductivity of 60 md-ft, which is relatively low compared to the estimated value from the previous numerical studies (Barba and Cutia 1992). The chosen fracture conductivity can be considered as acceptable, because the simulation runs indicate that a higher conductivity does not significantly increase the well production or pressure behavior.

Parameters	Value
Propped Fracture Width (ft)	0.02
Propped Fracture Porosity (1)	0.35
Propped Fracture Permeability (mD)	3000
Reservoir Temperature (^{o}F)	140
Initial Reservoir Pressure (psi)	3300
Reference Pressure (psi)	3300
Reference Datum Depth (ft)	7500
Reservoir Thickness (ft)	150
Reservoir Length (ft)	5500
Reservoir Width (ft)	3500
Reservoir Top Depth (ft)	7500
Rock Compressibility (1/psi)	3.90E-07
Horizontal Matrix Permeability (md)	0.5
Vertical Matrix Permeability (md)	0.5
Matrix Porosity (1)	0.107
Wellbore Radius (ft)	0.328

Table 4—Properties of propped fractures and reservoir

4.2.2 DFN Discretization

PEBI mesh is generated for the propped DFNs (**Fig. 32**). The properties of cells and inter-cell such as depth, transmissibility and pore volume are calculated based on the cell dimensions as well as fractures and matrix properties listed above.

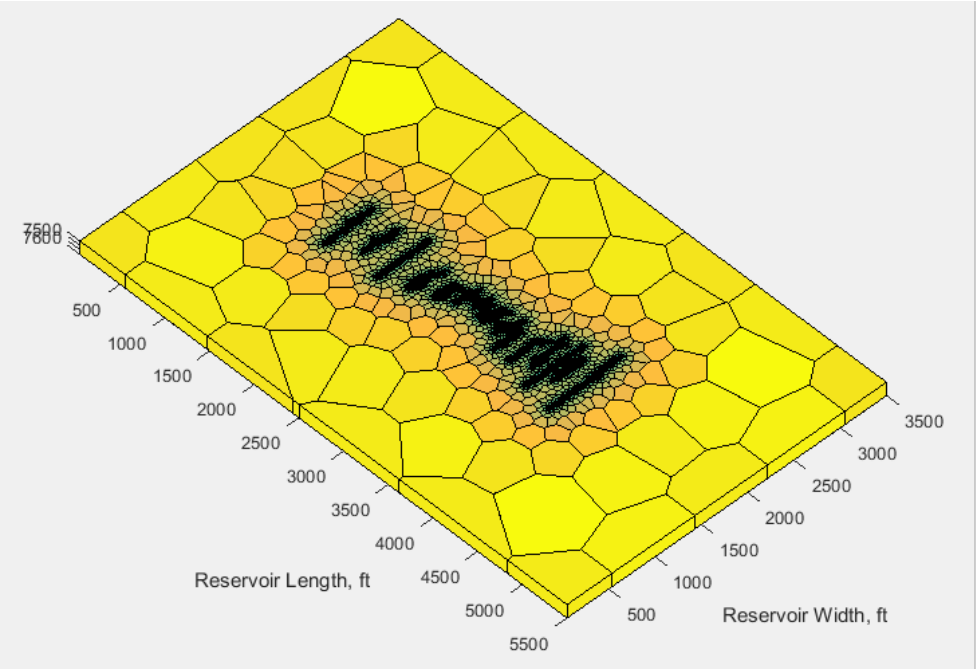

Fig. 32—the 2.5D unstructured mesh of the DFN.

4.2.3 Reservoir Fluid Properties

Oil, gas and water properties are either gathered from data published or shared from the operator. PVT table is generated from a black-oil correlation based on oil and gas gravity and GOR. The calculation of local properties of the fluid follows the method summarized by McCain (1991). Oil bubble point is calculated based on solution GOR method – the combination of Lasater's

correlation and Standing's correlation (Beggs 1987; Chierici et al. 1974). The fluid properties and PVT data are shown in **Table 5** and **Table 6**.

Parameters	Value
Oil API Gravity (°)	42.3
Gas Specific Gravity (1)	0.932
Initial GOR, scf/bbl.	750
Bubble Point Pressure (psi)	1611
Water Density (lb/ft3)	61.83
Water Compressibility (1/psi)	3.15E-6
Water Viscosity (cp)	0.5
Water Formation Volume Factor (RB/STB)	1.003

Table 5—Water and oil properties from the field data, literature and correlation

Pressure (psia)	Bo (RB/STB)	Bg (RB/MSCF)	Rs (MSCF/STB)	Vo (cp)	Vg (cp)
14.7	1.039	1.3931	0.0086	204.1029	0.0103
121.1	1.0546	1.1906	0.041	24.1079	0.0104
227.6	1.0736	1.0307	0.0791	12.4777	0.0107
334.0	1.0952	0.9088	0.1208	8.2558	0.0109
440.4	1.1189	0.8143	0.1651	6.0716	0.0113
546.9	1.1445	0.7394	0.2115	4.7359	0.0117
653.3	1.1717	0.6785	0.2597	3.8344	0.0121
759.7	1.2005	0.6281	0.3096	3.1856	0.0127
866.2	1.2308	0.5857	0.3608	2.6971	0.0133
972.6	1.2625	0.5496	0.4133	2.3179	0.0141
1079.0	1.2955	0.5183	0.467	2.017	0.0149
1185.5	1.3297	0.491	0.5217	1.775	0.0159
1291.9	1.3652	0.4669	0.5774	1.5792	0.0171
1398.3	1.4018	0.4454	0.6341	1.4202	0.0183

Table 6—The PVT table for oil and gas in the black-oil model

Pressure (psia)	Bo (RB/STB)	Bg (RB/MSCF)	Rs (MSCF/STB)	Vo (cp)	Vg (cp)
1504.8	1.4395	0.4263	0.6916	1.291	0.0197
1611.2	1.4783	0.409	0.75	1.1858	0.0212
2348.9	1.774	0.3237	1.1743	0.8213	0.0324
3086.7	2.1113	0.272	1.6268	0.6971	0.042
3824.5	2.4846	0.237	2.1021	0.6361	0.0498

Table 6—Continue.

4.2.4 Relative Permeability Curves

Putra and Schechter (1999) developed relative permeability curves for both fracture and matrix based on imbibition test on the Upper Spraberry rocks. Relative permeability curves with the same straight-line type are used for propped fractures in this study. Berea sandstone cores with heterogeneous fractures have a slightly curved relative permeability for oil-water flow, and the endpoints of relative permeability are 1 for both water and oil (Deghmoum et al. 2001). However, such sandstone cores have a matrix permeability of 100 md, which is much higher than that of 0.108 md in our case. It is possible that the relative permeability becomes less curved if the matrix permeability is lower, since the fractures play a more dominant role. Hence, slightly curved relative permeability is used for the matrix as a result of the fractured feature of this reservoir. Natural fractures behave as channels for fluid flow, especially during the early stage of production. Moreover, an end point (1) of relative permeability is set for water at residual oil saturation, in view of the unpropped but opened NF benefiting high water production rate at the beginning. On the other hand, a lower end point (0.8) of oil relative permeability is set, owing to the reduced fluid flow when the width of unpropped NF decreases with pressure drawdown (**Fig. 33**).

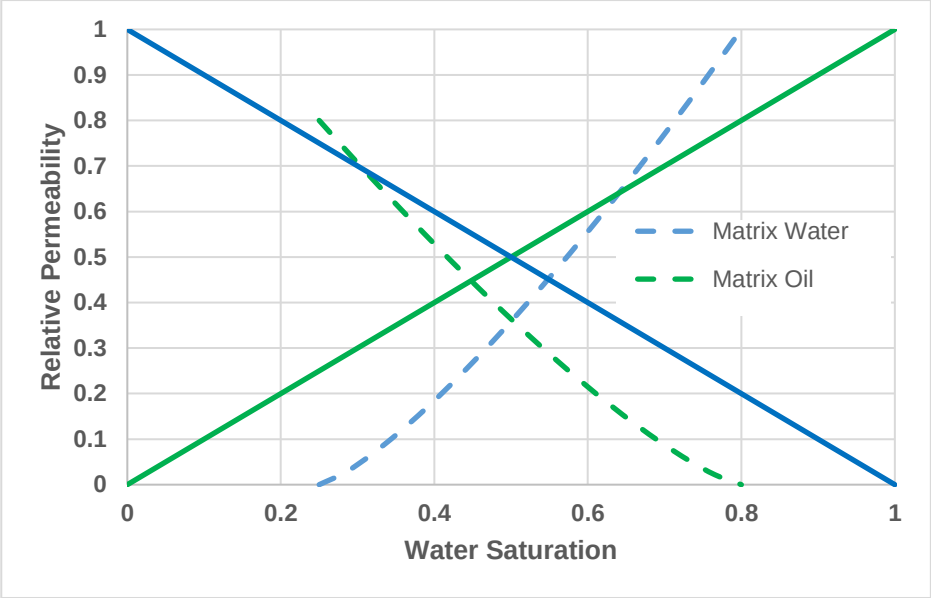

Fig. 33—Relative permeability curves for water/oil in reservoir matrix and propped fractures.

4.2.5 Results of History Match

This well is equipped with a gas lift pump. The oil/water/gas production rate, gas injection rate, casing pressure and tubing pressure within a period of the first 116 days of production were provided by the operator. Bottom hole pressure (BHP) is calculated based on tubing pressure, surface fluid production rate and gas injection rate with Beggs and Brill correlation (Beggs and Brill 1973). It is assumed here that the separator gas is used and injected at the valve placed at the end of the tubing.

Initial water saturation is set with a decreasing trend from propped fracture to the matrix of the distant part of the reservoir, ranging from 0.99 to 0.35 as a result of trial and error for history match. The simulation runs by constraining well operation with the high water production rate for the first 3 days, then the oil production rate for the following days. **Fig. 34** shows the simulation

results of oil production and BHP in comparison with the actual data. There's almost no oil produced at the beginning since the opened fractures are full of hydraulic fluid, and the nearby matrix also has high water saturation due to leak-off. The simulated BHP is closed to the history data but decreases more slowly. Water production rate and cumulative water production volume match well (**Fig. 35**). It reveals the combination of relative permeability curves and modified initial water saturation could represent the reservoir condition and flow behavior good enough. Fig. 36 shows that the simulated gas oil ratio (GOR) has a good match with the actual one.

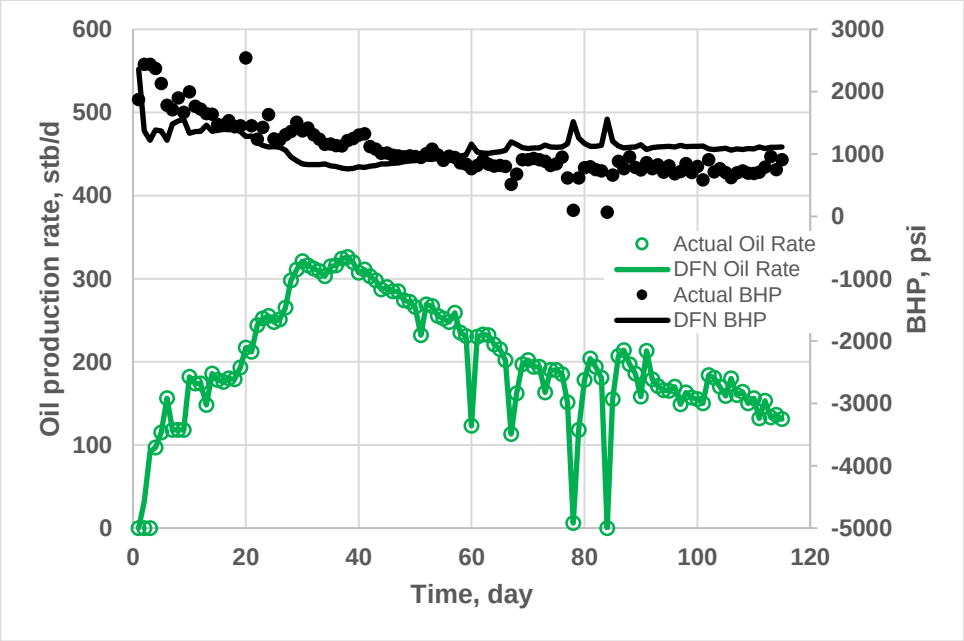

Fig. 34—Comparison of simulation results with actual history data for oil rate and BHP.

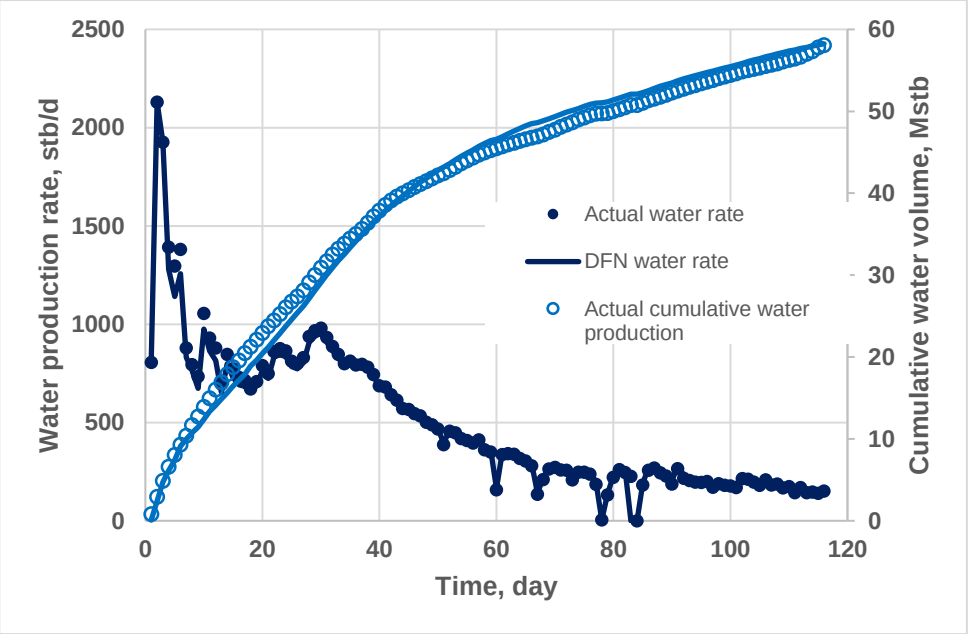

Fig. 35—Comparison of simulation results with actual data for water production rate and cumulative water production volume.

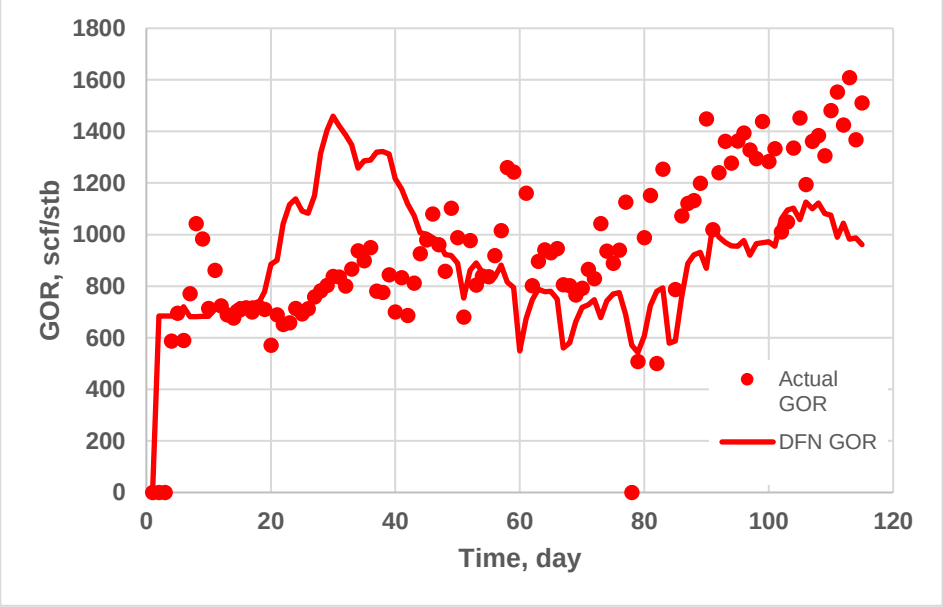

Fig. 36—Comparison of simulation results with actual data for GOR.

Fig. 37 shows the initial and final water saturation maps for the whole reservoir and zoomed view of some stages. At the beginning of production, hydraulic fluid filled the propped fracture with a saturation of 0.99. And it decreases to 0.96, 0.67, 0.5 and 0.35 step by step with distance increases (**Fig. 37(c)**). It is interesting to note that even though the saturation in propped fractures decreases to approximately 0.5, there's still a high-pressure band around the propped fractures (**Fig. 37(f)**), which is maintained by the formation water following towards the well.

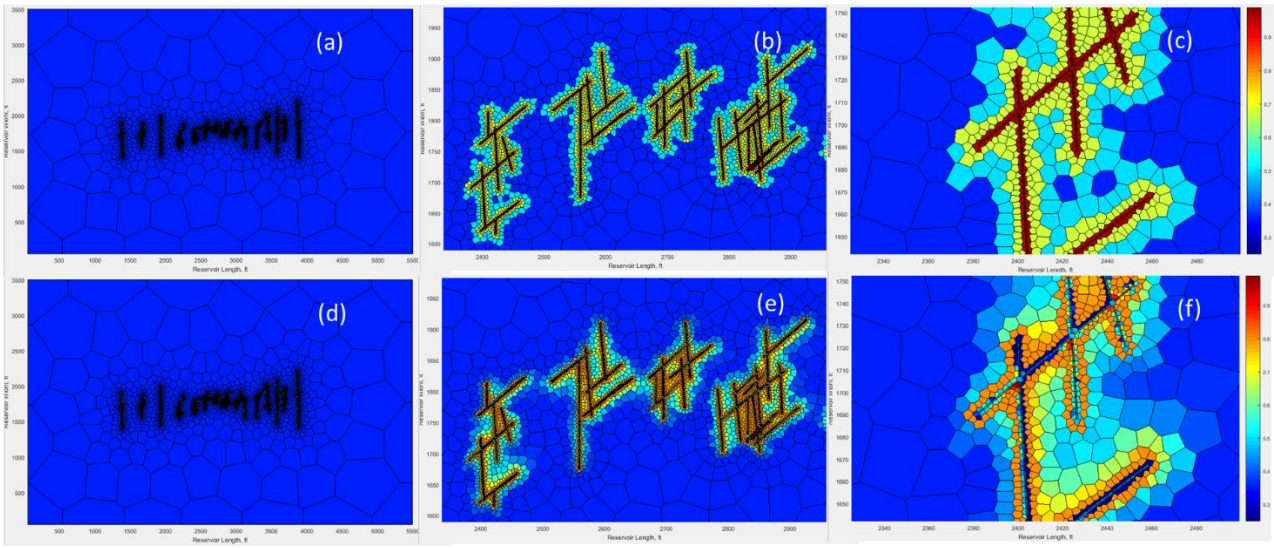

Fig. 37—(a)(b)(c) The initial water saturation at different scales. Water saturation in the area near the propped fractures is set higher due to hydraulic fluid leak-off. (d)(e)(f) Water saturation on the 116th day at different scales.

Pressure maps at the initial condition and at the end of the simulation are shown in **Fig. 38**. Pressure in the distant part of the reservoir decreases to around 2100 psi in the end as seen in **Fig. 38(b)**. Consequently, the fluid flow in matrix is boundary dominated. At the near propped DFN region, pressure decreases to around 1500 psi.

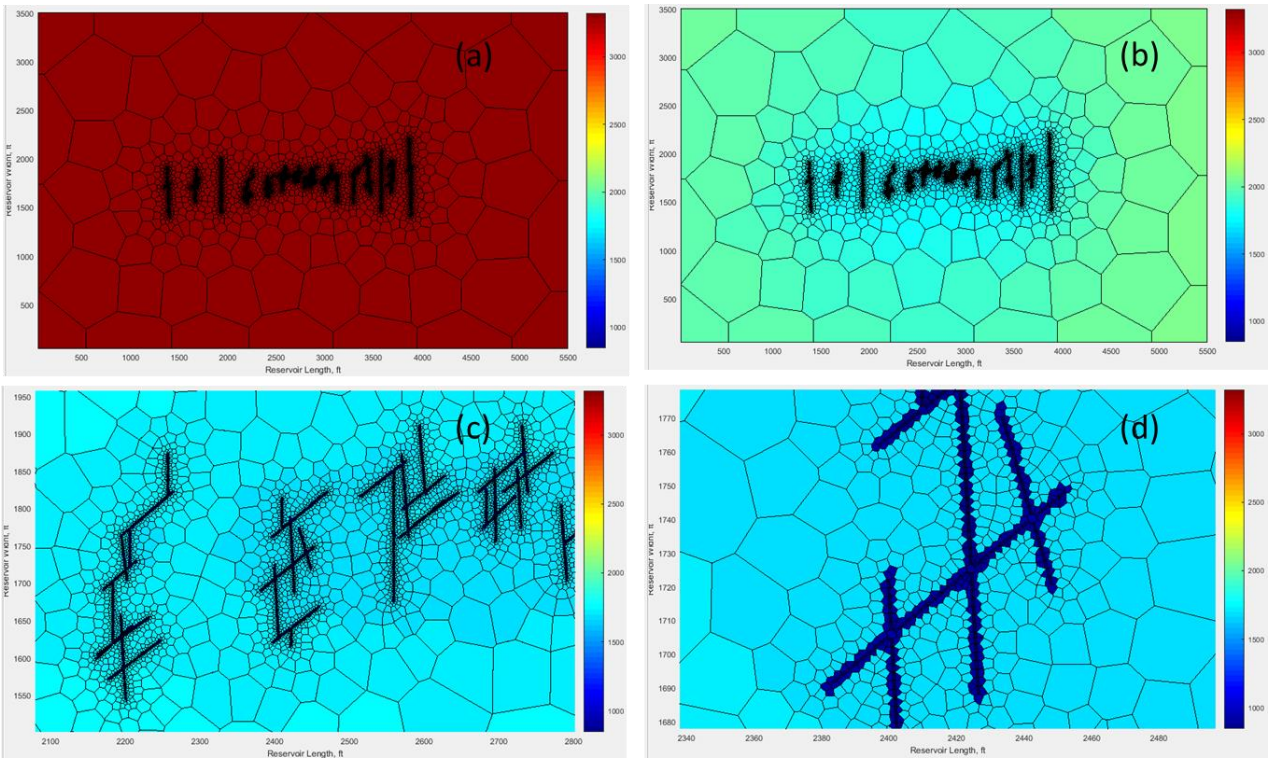

Fig. 38—(a) The initial reservoir pressure. (b)(c)(d) Pressure map on the 116th day at different scales.

4.3 Discussions

Despite the fact that the effective MS events distributed approximately in the one plane with perforations along the maximum horizontal stress in most of the stages, a bias is observed for some of the stages. One possible reason is the inter-stage communication occurs due to annular fluid flow or leaking plugs (Wheaton et al. 2016). The lack of events is also observed in the heel region, likely resulting from the poor geophone location for imaging this area.

This approach does not include a filtration process for neighboring MS events. It is still possible that some of the effective MS events are triggered by the slippage of the same natural fractures. Therefore, the hydraulic fractures may be captured by more natural fractures during its propagation than reality. Accordingly, the extension lengths of the hydraulic wings in the model become smaller. Nonetheless, the history match indicates such DFN is still acceptable to represent the geometry of the sink. It is because the propped fracture area is constrained by the total proppant mass injected and plays an important role in the low permeability reservoir.

From the history match, it is seen that the actual BHP decrease more steeply than the simulation results. In reality, it could be caused by the smaller well spacing. Moreover, reduction in conductivity of induced but unpropped fractures with fluid depletion may be due to another reason. These fractures will be created and close over time, impacting short-term and long-term production (Sharma and Manchanda 2015).

Our history matched model links the reservoir and completion data, such as the MS, to the production behavior of the whole well.

CHAPTER V

DFN MODELS BASED ON OUTCROP MAP/FMI LOG

Both outcrop map and FMI log could provide intuitionistic information about the underground natural fracture geometry. FMI log conducted before and after hydraulic fracturing can also show the fractures created during the treatment. Sun (2016) presented a workflow to use outcrop map from Eagle Ford (Ferrill et al. 2014) to generate DFN models. In this section, a DFN model is generated with a similar approach, and calibrated with available Eagle Ford historical production data. Next, another DFN model is generated according to the FMI log of an Eagle Ford well.

5.1 DFN Generation Based on Outcrop Map

Firstly, outcrop map is digitalized (**Fig. 39**). There are two sets of NFs. The spacing of this NF network is heterogeneous, ranging from 1 ft to 10 ft for N-S striking NFs, and from 15 ft to 40 ft for E-W striking NFs. Secondly, the outcrop map is duplicated to generate a pattern of NF network which covers a stage of the hydraulically fractured horizontal well (**Fig. 40**). The modeled stage has 5 hydraulic fractures which are perpendicular to the horizontal well. The NF pattern is a 5*3 duplication matrix of the original outcrop map, including 1125 natural fractures in total. It is well established that natural fractures, even when sealed with mineral cement, can be reactivated during hydraulic fracturing treatment (Dahi-Taleghani and Olson 2011; Gale et al. 2014). Coring of Wolfcamp shale showed not all the natural fractures are reactivated, and many of them remain intact (Gale et al. 2018). In this section, intersected HFs and NFs are assumed to connect, and the

NFs are assumed to have a much higher permeability than the matrix rock. The single stage DFN model is then discretized by PEBI grid, shown in **Fig. 41**. This model has 107,493 cells.

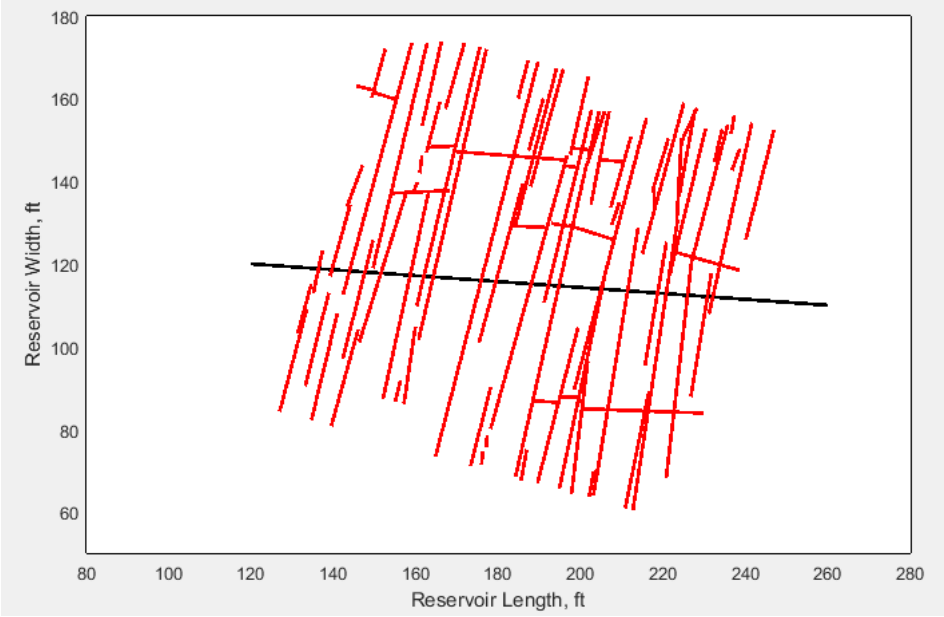

Fig. 39—The digitalized outcrop map.

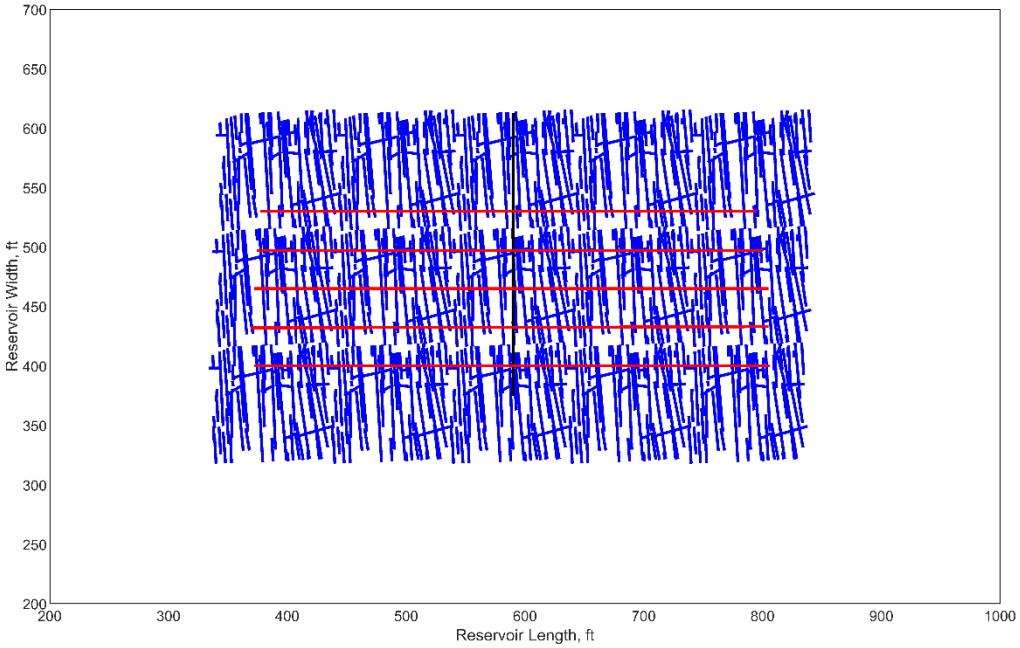

Fig. 40—NF network is generated by duplication of outcrop map. Five hydraulic fractures are placed, representing one fracturing stage of the horizontal well.

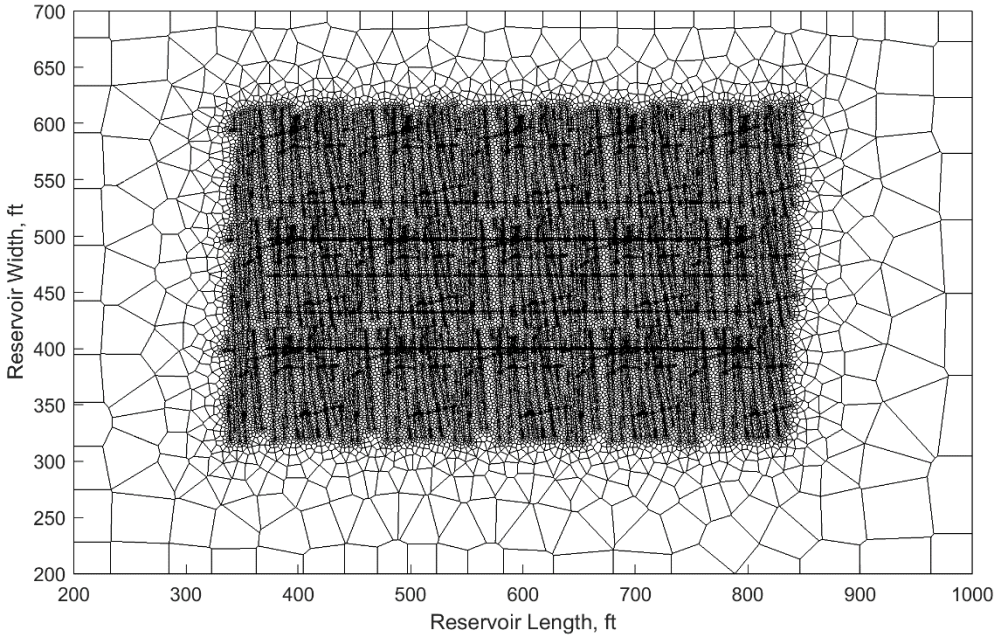

Fig. 41—The PEBI grid of the DFN model based on the outcrop map.

This model is assumed to be a type well in a specific geological area, since the history data used is an average production rate of six horizontal wells located in the volatile oil region in Eagle Ford formation (Phi and Schechter 2017). These wells were completed around 2010 with 4-8 clusters per stage, and 10-20 stages for each well. The length of the horizontal well is assumed to be 4200 ft. Since the model is a single stage model, the simulation results are upscaled to the full well by a multiplier.

Width of these hydraulic fractures is 0.03 ft. Half-length of them is set to 150 ft. For the hydraulic fracture segment within 75 ft to perforation, the permeability is set to 700 md (21 md-ft conductivity), which could be considered to achieve infinite conductive. For the HF segment from 75 ft to 150 ft, the permeability is set to a same number as that of NF. Such number is calibrated through history match. The reason is that field coring showed proppant hardly transported beyond 75-ft distance (Raterman et al. 2018). It is also observed that hydraulic fractures are steeply dipping rather than vertical, but modeling them as vertical plane should not affect the results too much. Other parameters are tuned within the range from public data, shown in **Table 7**. In terms of the well schedule, the well is constrained by a maximum oil rate at the beginning of production, accounting for the hydraulic fluid flow back. After that, a constant BHP of 1500 psi is used to constrain the well operation.

	DFN MODEL	REFERENCE	SOURCE
Matrix perm, nd	400	1 to 800	Inamdar, 2010
Matrix porosity	0.08	Limestones 4 – 6%, Marls 8 – 12%; 8-12%; 4-15%	Tobi, 2017; Za Za Energy, 2013; Drillinginfo
Thickness, ft	80	50 to more than 300; 25-100;	Stegent et al., 2010; contour map
NF spacing, ft	Outcrop		
HF spacing, ft	32	Cluster spacing 47 ft; Fracture count exceeds cluster count; 20 – 60% of wellbore has fractures at < 5ft spacing;	Kevin et al., 2018
HF perm, md	<75ft: 700 75~150 ft: 0.6	Proppant hardly transport beyond 75 ft. GOHFER: 5-20 md-ft (CfD> 30, infinite Cd) Over 75 ft: ~0.1 md-ft	Kevin et al., 2018 GOHFER modeling
NF perm, md	0.6	History match	
Depth, ft	8000	5000-12000	contour map
Initial pressure, psi	5000	0.4-0.8 psi/ft; 0.5-0.8 psi/ft; 0.6 psi/ft	Stegent et al., 2010; Za Za Energy, 2013; Drillinginfo

Table 7—Parameter tuned with history match and their reference range.

Parameters of the EOS and initial composition used is same as those in paper from Phi and Schechter (2017), shown in **Table 8**.

Components	CO2	N2 to C1	C2 to C3	IC4 to IC5	FC6	C7+
Initial mole fraction	0.011	0.627	0.173	0.059	0.015	0.114
MW, gm/gmol	44	16.25	34.59	63.48	86	16.46
Acentric factor	0.225	0.008563	0.115398	0.206523	0.27504	0.49007
Critical pressure, atm	72.8	45.20076	46.14292	35.54813	32.46	20.39975
Critical volume, m3/k-mol	0.094	0.09883	0.165089	0.2756	0.344	0.664578
Critical temperature, K	304.2	189.4124	327.7392	436.9842	507.5	674.8091
Parachor	78	76.3666	121.629	202.573	250.109	460.728
Average normal boiling point, F	-109.21	-254.114	-75.0611	53.3246	146.93	421.166
OMEGA	0.457236	0.457236	0.457236	0.457236	0.457236	0.457236
OMEGB	0.077796	0.077796	0.077796	0.077796	0.077796	0.077796
Pseudo-critical volumes, m3/kmol	0.094	0.098833	0.16572	0.275916	0.344	0.664578
BIN, N2 to C1	0.103153					
BIN, C2 to C3	0.128389	0.004373				
BIN, IC4 to IC5	0.116143	0.017293	0.004362			
BIN, FC6	0.115	0.025414	0.008921	0.000819		
BIN, C7+	0	0.057802	0.031531	0.012784	0.007187	
Reservoir temperature, F				307		
Initial saturation pressure, psi				4191		
Initial viscosity, cp				0.055		
Initial GOR, scf/stb				4200		

Table 8—Parameters related to the compositional modeling.

Simulation results of history match are shown in **Fig. 42**. The match of oil rate and cumulative oil production is acceptable, considering water, gas and BHP data are not available for model calibration. In this section, the purpose of calibration by history match is not to build an exact model for a particular well. It is to validate the approach of using outcrop map to generate DFN models. The results indicate that such models with appropriate reservoir parameters could have reasonable production behavior.

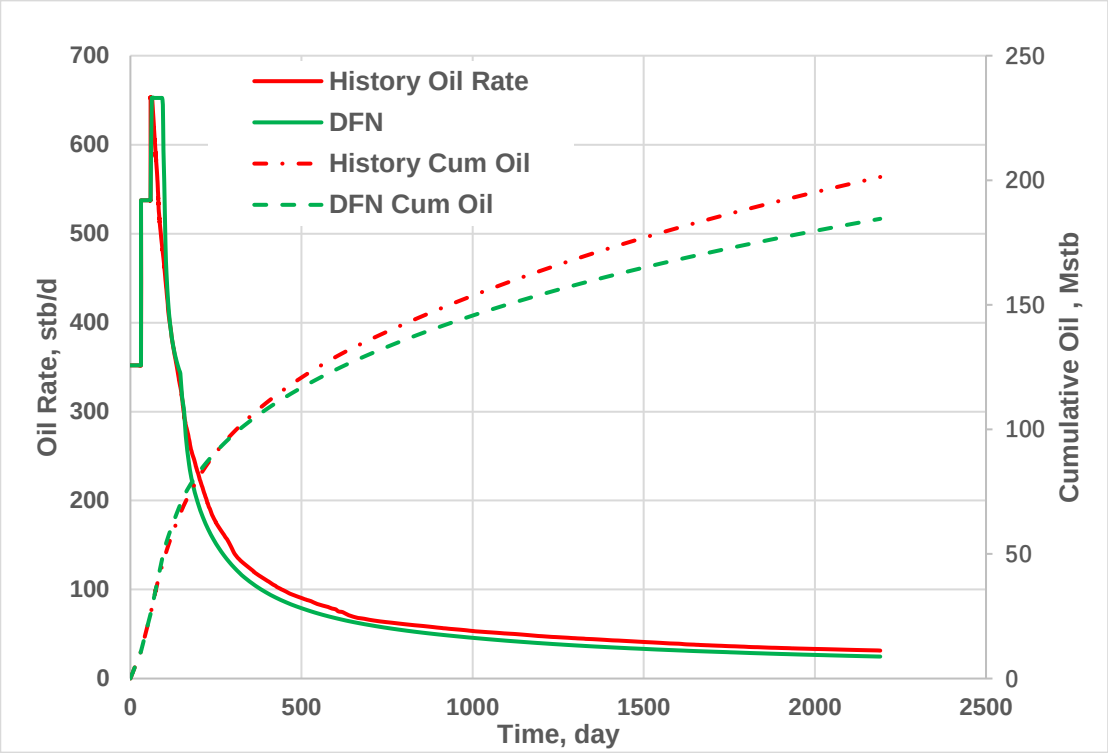

Fig. 42—Simulation results after the calibration with historical oil rate.

5.2 DFN Generation Based on FMI Log and DAS/DTS Response

Raterman et al. (2018) showed a lot of field data about a hydraulic fracturing job in Eagle Ford. That paper includes cores and FMI log from data wells drilled after fracturing treatment, and distributed acoustic sensing/distributed temperature sensing (DAS/DTS) data from neighboring horizontal producers. FMI log and cores obtained exactly reveal the fractures' location, which could give information about the trend of fracture propagation distance, and proppant distribution, because the data wells are located at different distances to the treatment well. From FMI log before the treatment, nearly no natural fracture is observed. From FMI log after the treatment, hydraulic fractures exist, and they form swarms in which many fractures are spaced just a few inches apart. And these swarms are separated with several feet (**Fig. 43)**. From the fracture density histogram based on the FMI log, a trend is found that the density decreases above and laterally away from the treatment well (**Fig. 44**). DAS/DTS data in neighboring producers acquired during the treatment showed response, indicating some hydraulic fractures could propagate more than 1500 ft. The response spacing in DAS/DTS has good correspondence to the cluster spacing in the treatment well.

It is also found that there's no permeability enhancement to intact rock matrix, which was supported by SEM mapping and steady-state core-plug-permeability measurements from both pre-stimulation and post-stimulation cores.

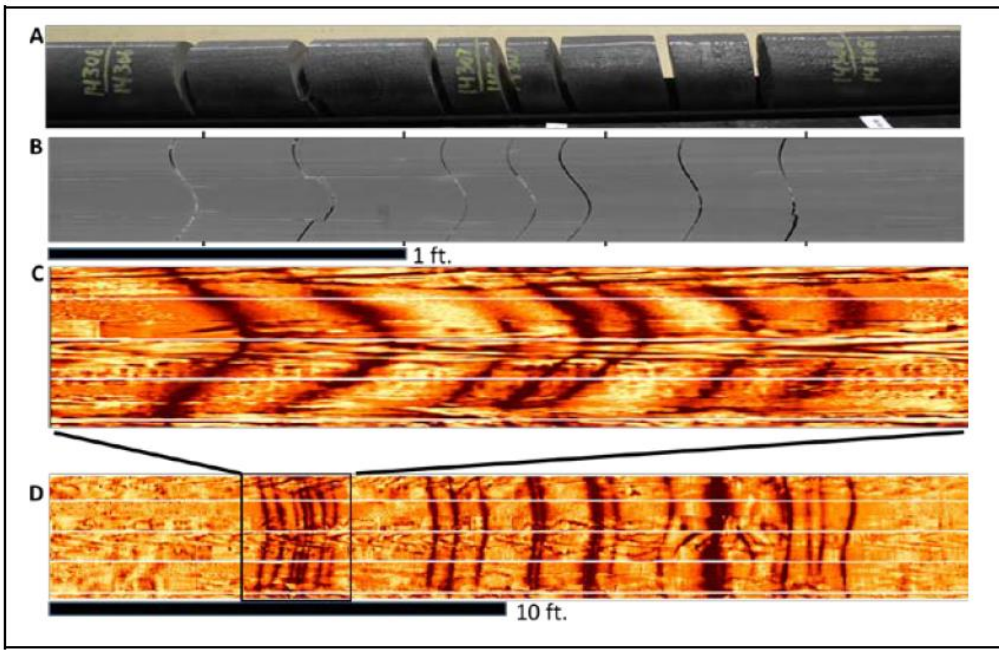

Fig. 43—FMI log of an Eagle Ford well shows swarms of hydraulic fractures with uneven distribution.

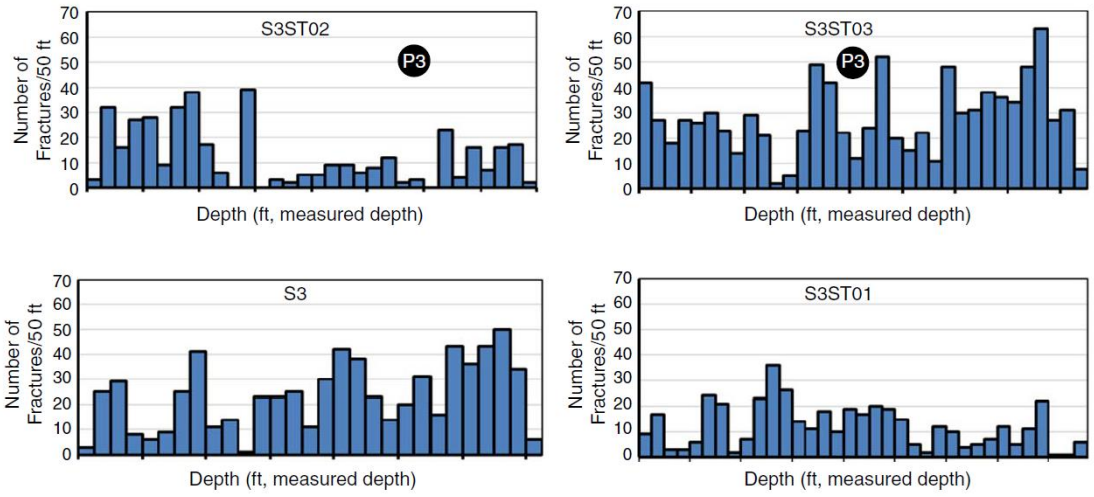

Fig. 44—Fracture density at each data well with different distance to the treatment well.

A cluster DFN model is built according to the information released for this Eagle Ford well. Its cluster spacing is 50 ft. The hydraulic fracture spacing is generated according to the FMI log and cores shown in **Fig. 43**. The lengths of these fractures are determined according to the trend shown in **Fig. 44**. The length information is shown in **Table 9**. If more FMI log data is available, it is possible to build a DFN model which covers a full stage or a full horizontal well. Note that images from FMI log covering a full well are numerous, and could be treated by automatic interpretation with a similar technique applied for wellbore schematics (Kemajou et al. 2019).

Number of transverse fractures	Length, ft
1	1500
10	360
10	130
21	70

Table 9—Lengths of the fractures in the cluster DFN model.

From the paper, it is also observed that the hydraulic fractures within any of the swarms have an orientation difference of 5° to 20°. And the HFs diverge with a projected line of the intersection just outside the borehole wall. In this cluster model, the branching is simplified as multiple parallel transverse fractures initiated from longitudinal fractures (**Fig. 45**). PEBI grids of this model at different locations are shown in **Fig. 46**.

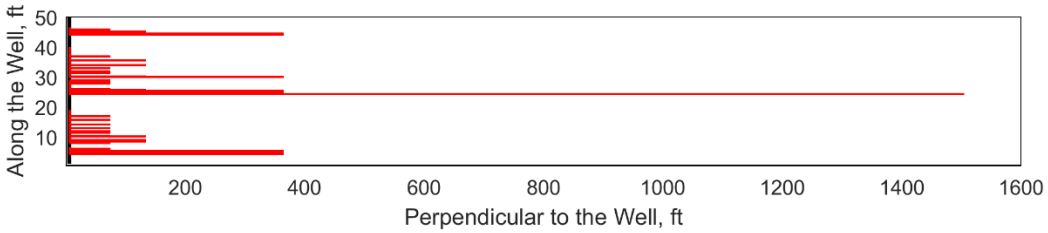

Fig. 45—The cluster DFN model generated based on FMI log and neighboring well response.

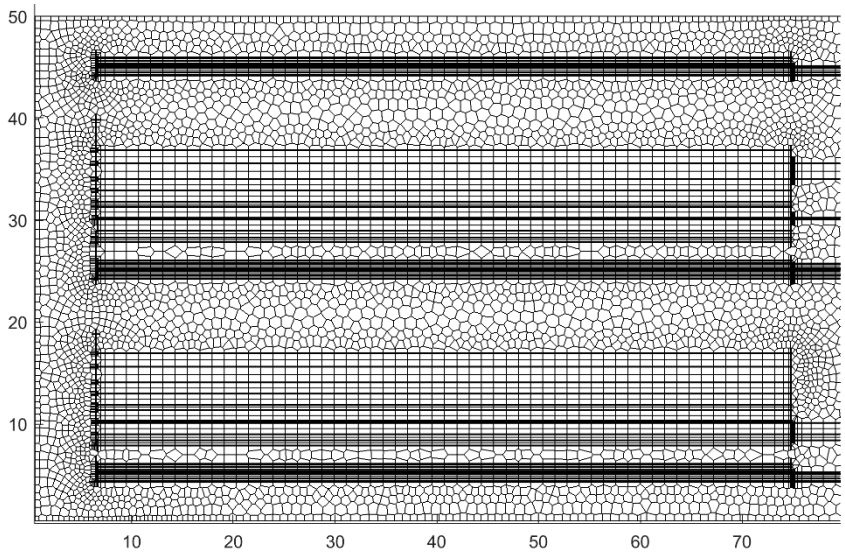

Fig. 46—Different parts of the PEBI grid of the cluster DFN model.

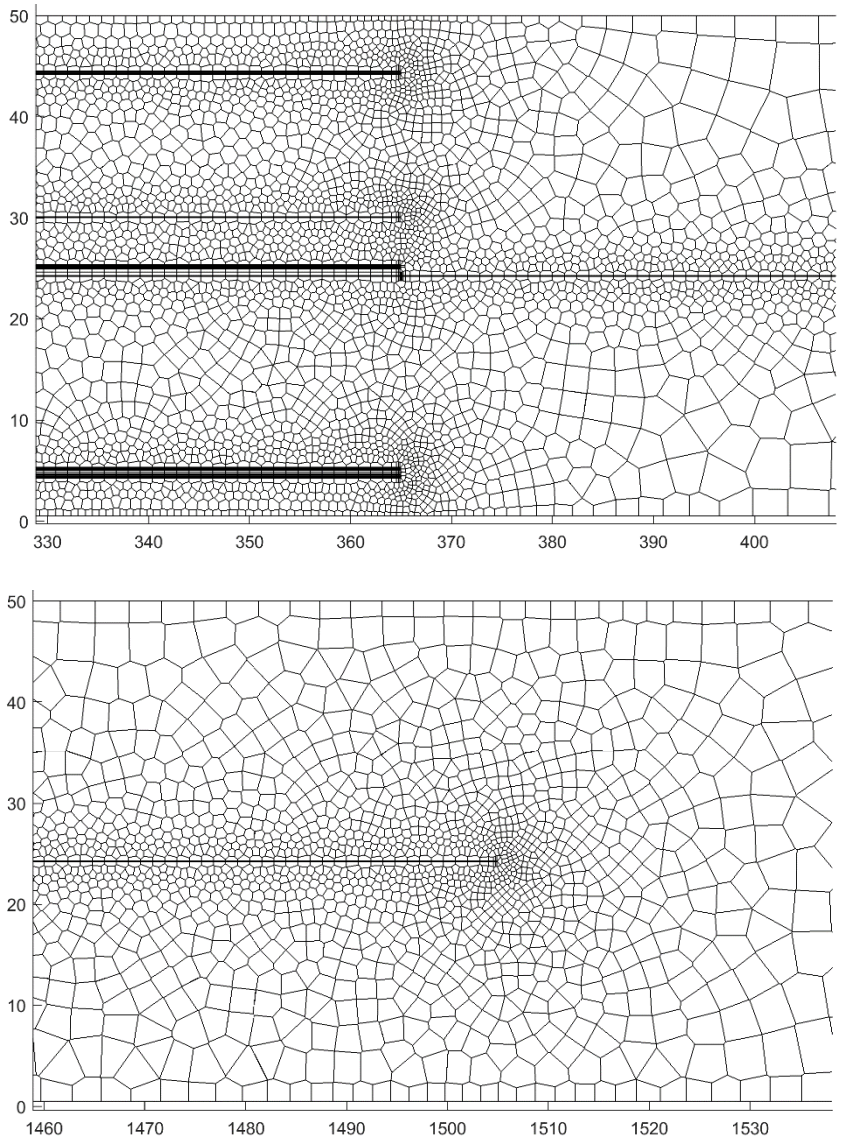

Fig. 46—Continue.

Since there was no data well placed in further distance, the number of fractures which extended further than 360 ft is unknown, and their true lengths are also unknown. Thus, this single-cluster DFN model may underestimate the total fracture area.

Permeability of these fractures is not constant along the fractures. For segment within 75 ft, the permeability is set to 700 md. For segment over 75 ft, which is considered as unpropped, its permeability is set to 20 md, which is determined by calibration with history data. This permeability setup accounts for the fact that proppant did not transport very far. Other reservoir and fracture properties are same as those in the previous section.

The simulation result, which is an upscale of the cluster model to a 4200-ft horizontal well, is shown in **Fig. 47**. The history data which is an average from six wells described in the previous section is also plotted. The only tuned parameter is the unpropped permeability. Not too much effort is made for this calibration. The purpose of the history match is to validate the production capability of the DFN generated from FMI log and DAS/DTS response. It reveals that natural fracture is not necessary to achieve an appropriate production performance if swarms of hydraulic fractures exist.

Pressure map and saturation map at 1st day, 1 month, 1 year, 2 year and 5 year are shown in **Fig. 48** and **Fig. 49**. It is obvious that the pressure and saturation distribution is uneven because of the uneven distribution of fracture density.

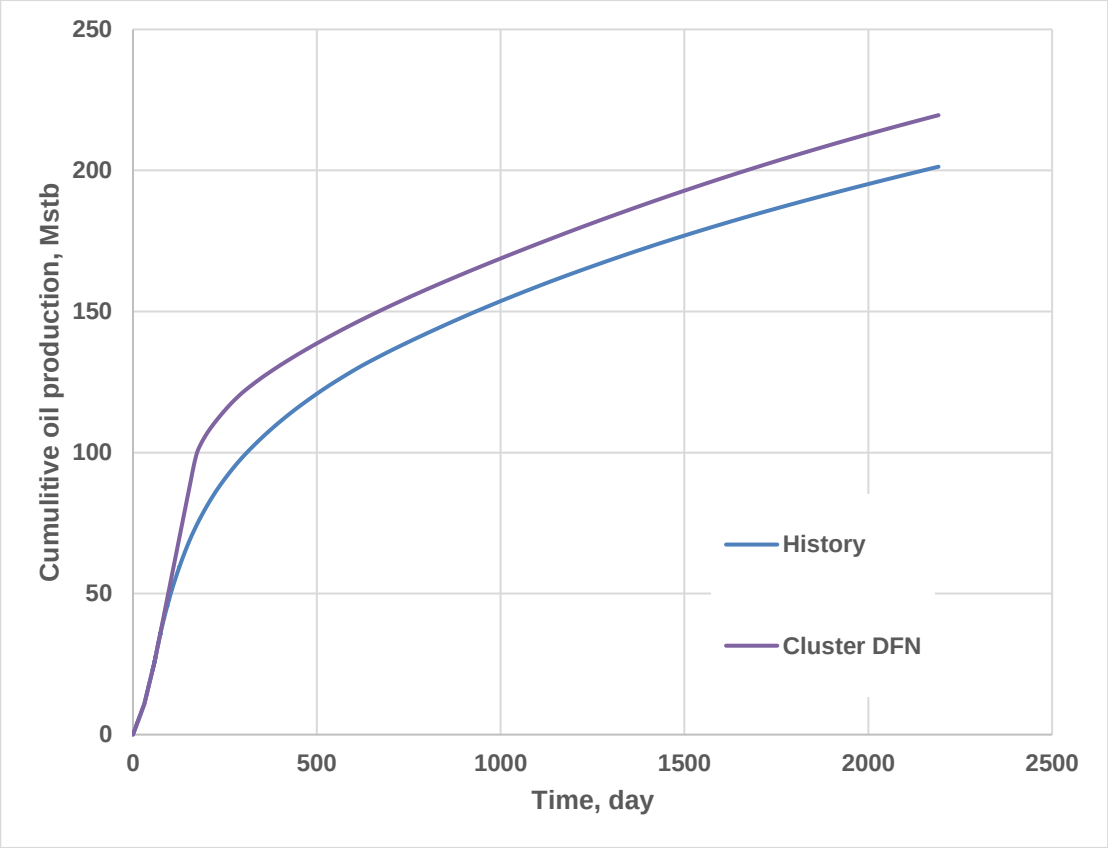

Fig. 47—Cumulative oil production of the Cluster DFN model and the historical data averaging from the six wells.

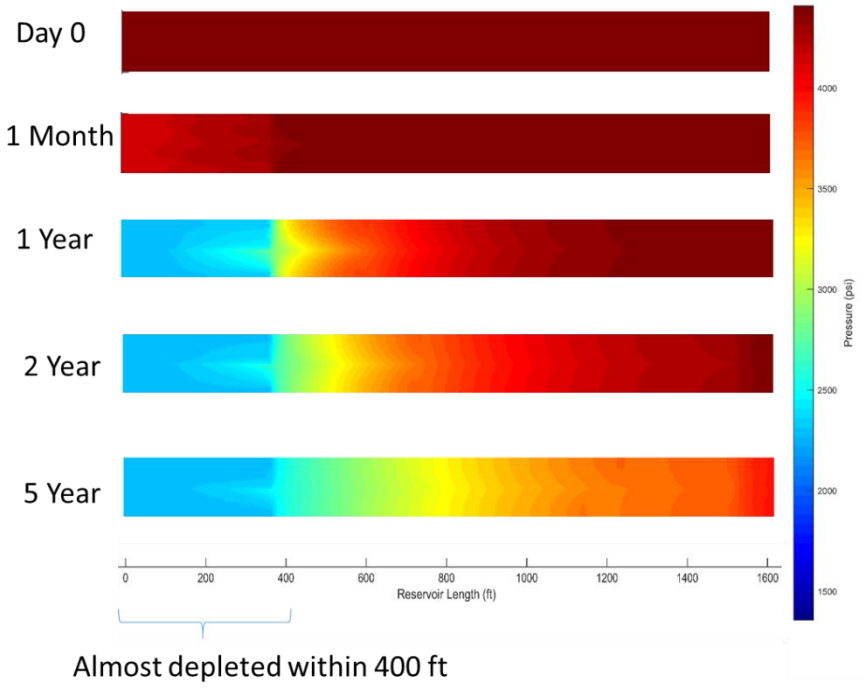

Fig. 48—Pressure map at different time. The region close to well is almost depleted after 5-year production, due to the high fracture density there.

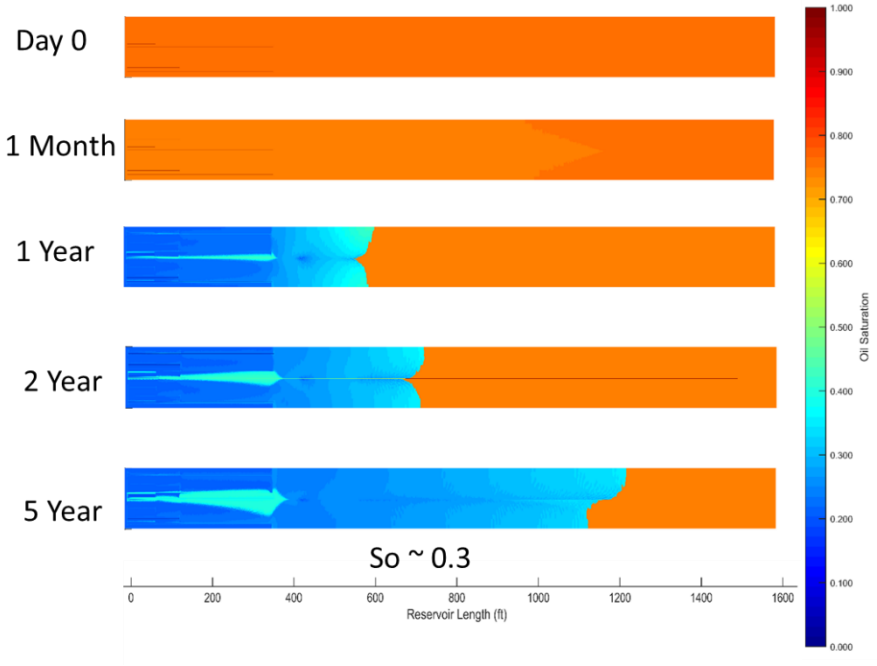

Fig. 49—Oil saturation map at different time. Oil saturation near well approaches to 0.3, and the residual oil saturation is 0.25.

CHAPTER VI

SURFACTANT EOR STUDY – LEAKOFF AND SPONTANEOUS IMBIBITION

6.1 Review of Lab Experiments and Core Model History Match

It is found that the shale such as Wolfcamp and Eagle Ford are originally oil to intermediate-wet. Organic matter such as kerogen can create a mixed wettability as a result of the water-wet inorganic pores and oil-wet organic pores. Such wettability can be altered toward water-wet by adding surfactants at concentrations of 1 - 2 gpt. Moreover, the interfacial tension between oil and water is also reduced by surfactant additives. As a result, surfactant-assisted spontaneous imbibition recovers 3x – 7x oil, compared to the water spontaneous imbibition (Alvarez et al. 2017a; Alvarez et al. 2018a; Alvarez and Schechter 2016a, 2016b; Alvarez and Schechter 2017; Alvarez et al. 2017b; Alvarez et al. 2018b; Saputra and Schechter 2018).

Although contact angle, IFT, zeta potential, and surfactant adsorption isotherm are measured, there is not a clear correlation which relates these values to the final recovery and recovery rate. It seems there is a trend that the lower contact angle leads to a higher final recovery factor, while lower IFT leads to a faster recovery. Probably contact angle reveals the degree of preference of the rock on oil, which determines the oil saturation at equilibrium. On the other hand, IFT affects the shape of oil in discontinuous flow, and lower IFT makes oil droplets easier to pass through pore throat. Thus, on the macro level, oil relative permeability increases as IFT decreases.

Core models were built (Zhang et al. 2018b; Zhang et al. 2019) to match lab results by using correlation derived capillary pressure curve and tuning relative permeability curves. In this section, the same input from one of the history match models in the paper is used (**Fig. 50)**.

Capillary pressure is elevated when a surfactant is added, which means that at low water saturation, capillary pressure becomes the driving force to suck water in and push oil out. The intersection at x-axis implies the ending point of spontaneous imbibition. Relative permeability of oil is improved by adding surfactant. Note that the ending points of relative permeability are not changed after surfactant soak, which may be incorrect. Wettability alteration and IFT reduction should result in a reduction of residual oil saturation.

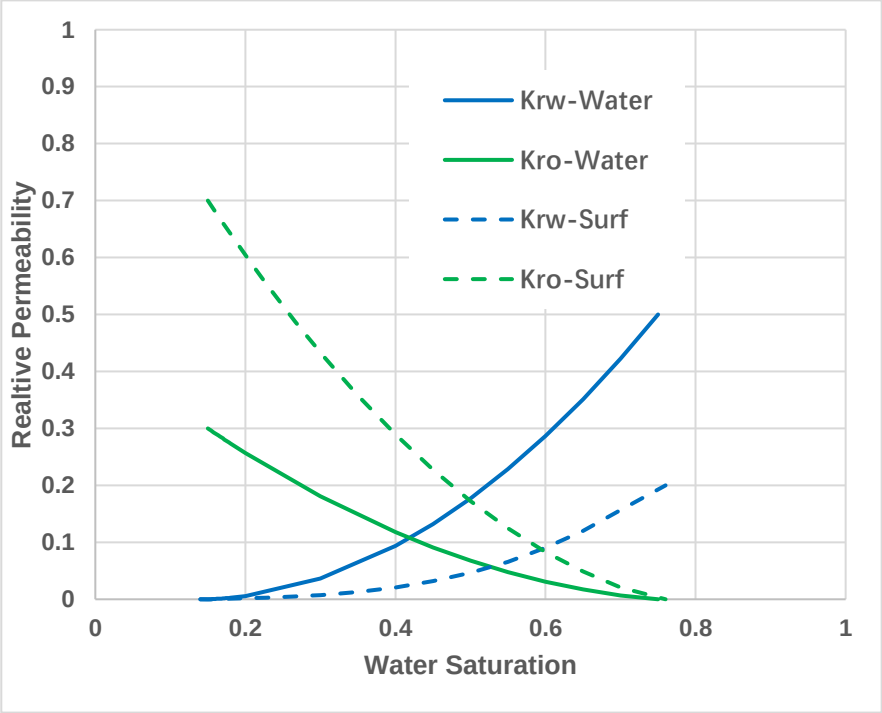

Fig. 50—Upper: oil-water relative permeability curves for water and surfactant cases; Lower: capillary pressure curves for water and surfactant cases. Adapted from the paper by Zhang et al. (2018b)

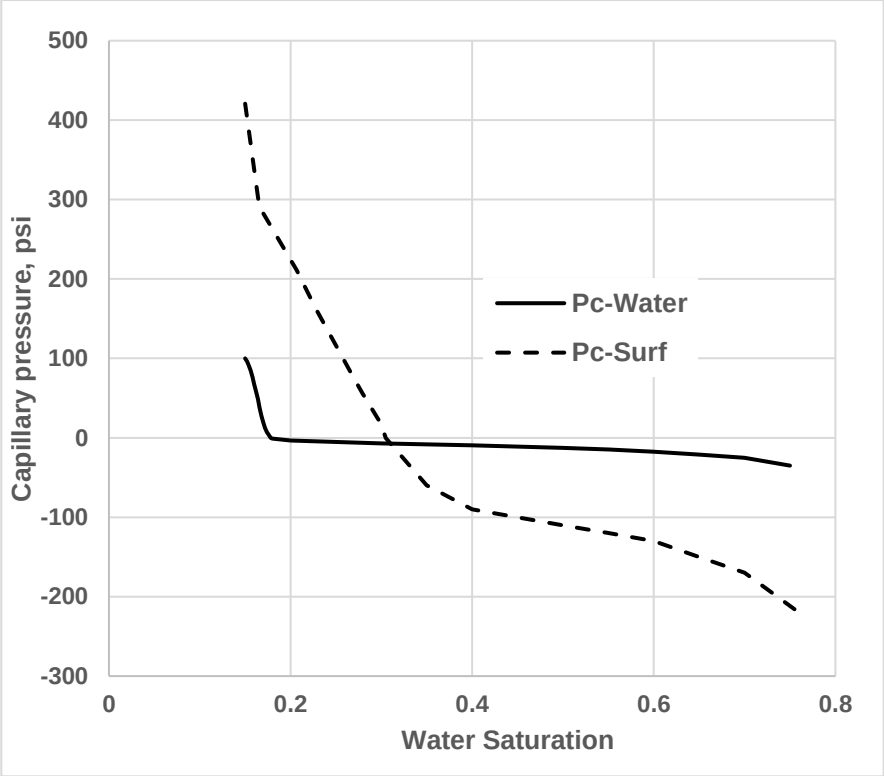

Fig. 50—Continue.

6.2 Field-Scale Simulation with DFN models

Based on the micro-mechanisms revealed from lab experiments, surfactant EOR simulation will be run on the calibrated outcrop-DFN models generated from the previous chapter. To reduce simulation time, only one-wing is modeled (**Fig. 51)**. Low salinity module in Nexus will be used to simply model the wettability alteration induced by surfactant solutions. Similar to the surfactant module in other commercial simulators, salinity is also treated as a tracer in the water phase. For surfactant, its effect on alteration of relative permeability curves depends on adsorption rate and its in-situ concentration in the aqueous phase. For a relatively long period of soak, surfactant adsorption completes and there's no further change of relative permeability curves. On the other hand, the process of salinity change does not have adsorption. So the alteration of relative permeability curves due to salinity change accomplishes instantaneously. Accordingly, it will be optimistic to use low salinity module to simulate surfactant if the soak period is not long enough. Moreover, to mimic the permanent adsorption of surfactant on the rock surface, the alteration of relative permeability curves in this study is set to be irreversible.

The process of fracture pore volume increase during hydraulic fracturing is also modeled, which could provide a relatively high volume of water or surfactant solution during imbibition. The schedule is to inject water/surfactant solution at 12,000 psi for 1 hour and then soak for 1 month. The production operation is constrained by BHP of 1500 psi.

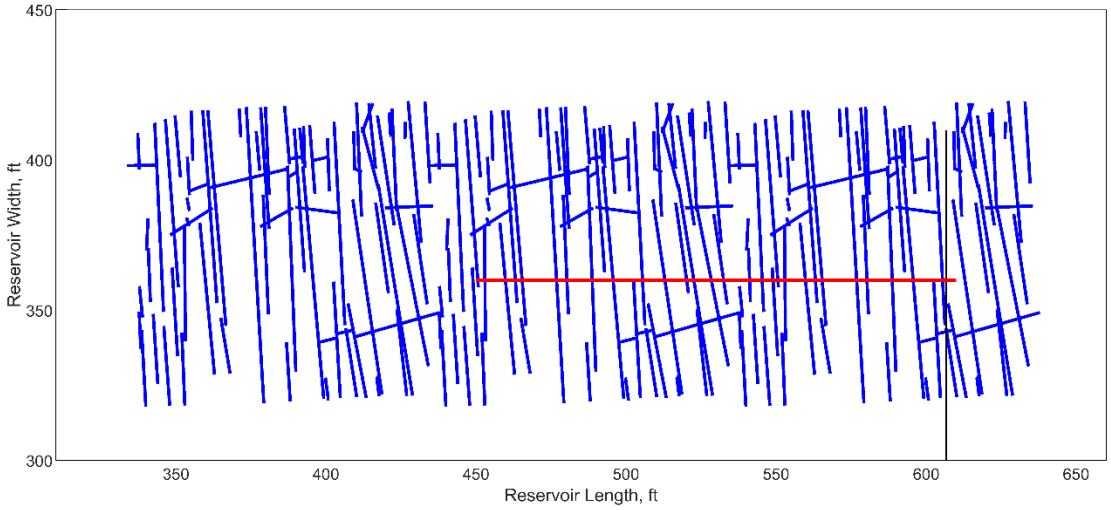

Fig. 51—One-wing model based on the calibrated outcrop-DFN model generated in the previous chapter.

Results of soak with water and surfactant are shown in **Fig. 52**. The green lines are the cumulative oil production, while the red line is the incremental recovery of surfactant soak comparing to water soak as the elapse of time. The effect of surfactant on oil recovery is marginal. The reason is that the region invaded by injection fluid is limited. **Fig. 53** shows the "surfactant" concentration distribution. Only matrix rock on each side of fractures within 2-ft distance is invaded by surfactant.

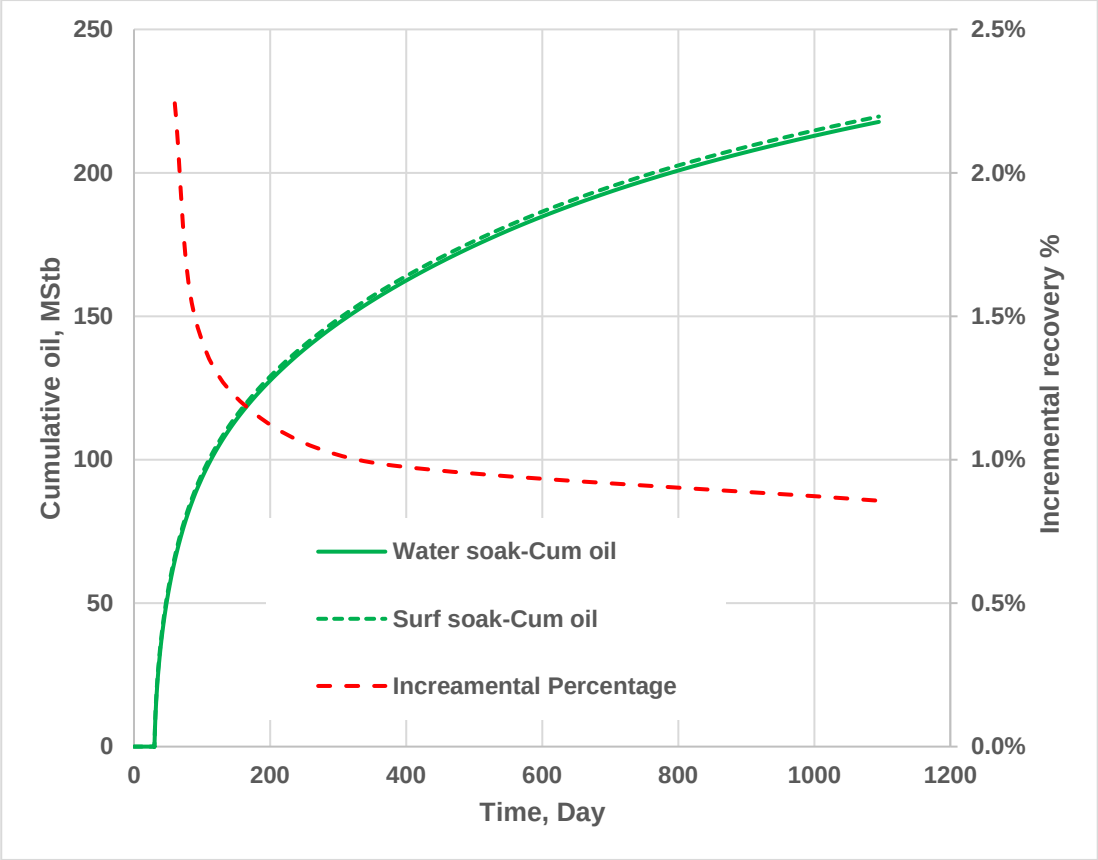

Fig. 52—Comparison of the water soak case and the surfactant soak case.

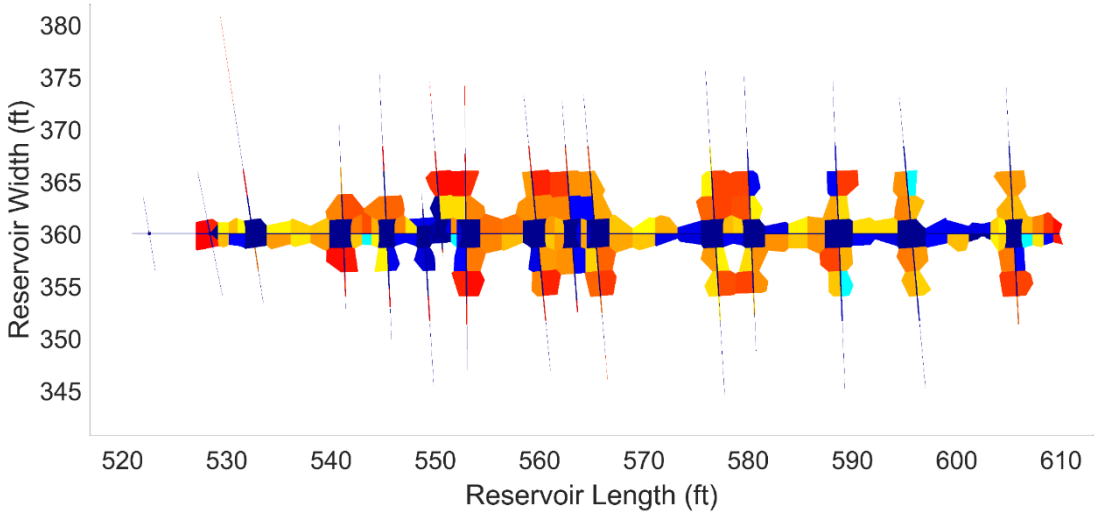

Fig. 53—"Surfactant" concentration map. The surfactant-invasion zone is limited within 2-ft distance to fractures.

The relative permeability curves of fractures used for the above cases are straight-line type. Many publications use straight-line type curves for fractures, although they may not have been correct (Kazemi et al. 1976; Pieters and Graves 1994). The capillary trapping mechanism caused by the roughness of the fracture wall leads to non-linear type curves (Chen et al. 2004; Lian and Cheng 2012). If surfactant can reduce the capillary force in rough fractures, relative permeability curves of fractures could switch from non-linear to linear. As a theoretical study, a case is run, in which the fracture relative permeability curves are the same as those of matrix before the surfactant addition, and turn to straight lines after the surfactant addition. The results are shown in **Fig. 54**. The incremental recovery is 43% at the beginning, and declines to 15.5% after 3-year depletion. It demonstrates that the effect of surfactant could be more significant if the switch of fracture relative permeability is considered. Unfortunately, such an effect has not been reported and further study is needed.

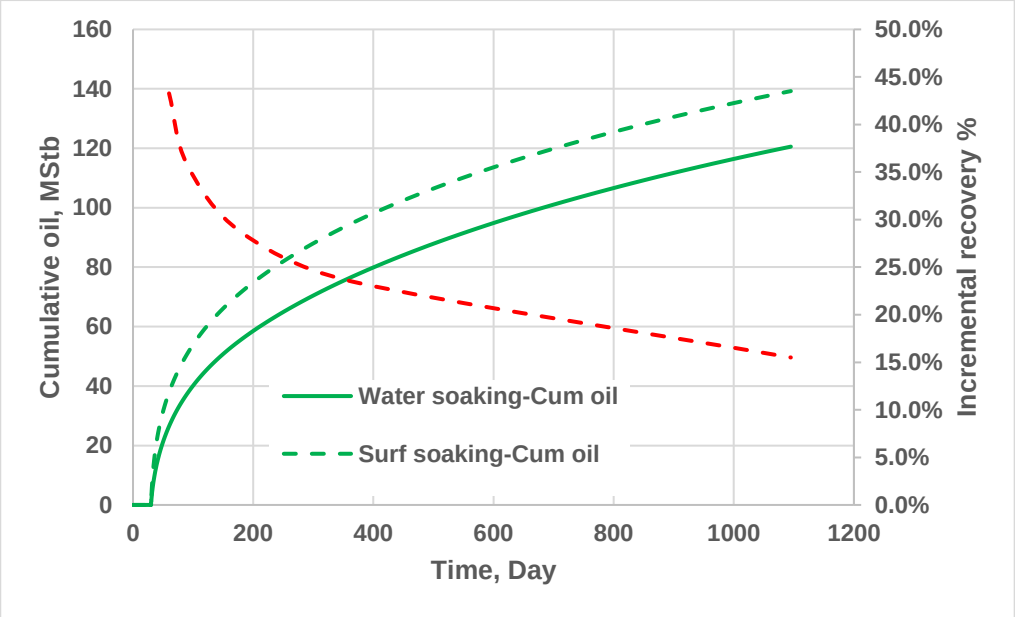

Fig. 54—Comparison of water soak and surfactant soak case. It is assumed the fracture relative permeability curves are the same as those used for matrix and can switch to linear if surfactant exists.

CHAPTER VII

GAS HUFF & PUFF STUDY

In this chapter, firstly, mechanisms of gas HnP experiments are reviewed and analyzed. Then the previous simulation studies are reviewed. Finally, the impact of discontinuity feature of fracture networks on HnP recovery mechanisms and operation optimization are investigated by the use of the calibrated DFN models.

7.1 Analysis of Swelling Tests and Slim Tube Tests in Publications

Swelling test or solubility swelling is a simple single-contact phase behavior experiment, which determines the relationship of saturation pressure and volume of gas injected, and the volume of the new saturated mixture compared to the volume of the original saturated reservoir oil (Ahmed 1989). It is a convection-assist equilibrium test by agitating the samples until a single-phase is achieved.

Usually, the injected gas mole fraction is tested up to 60%. For black oil and CO_2 mixture, saturation pressure increases with the injected gas mole fraction (**Table 10**).

	Recombined Wolfcamp oil	Recombined Cooper Basin oil
Initial GOR, scf/stb	1230	1250
CO2 mole %	Saturation pressure, psi	
0	3479	2364.7
20	3603	2697.7
40	3867	2969.7
60	4635	3401.7
MMP, psi	3600	2800

Table 10—Initial GOR, saturation pressure observed from the swelling test with CO2, and minimum miscible pressure (MMP) of recombined Wolfcamp oil and Cooper Basin Oil (Bon 2009; Liu et al. 2018).

It is possible that the saturation pressure decreases with gas mole fraction increase, if gas mole fraction is above a limit. A stock tank oil is used to run the CO_2 swelling test by simulation (CMG WinProp). The composition of the stock tank oil is obtained from the simulation results of the Eagle Ford oil described in the previous chapter, shown in **Table 11**. Saturation pressure and swelling factor are shown in **Fig. 55**. Saturation pressure turns to decrease when CO_2 mole fraction is over 90%. Upon the definition of miscible fluids, which is the two fluids can mix in all proportions to form a homogeneous solution, the miscible pressure is around 2827 psi from the saturation pressure diagram. For the original Eagle Ford oil described in the previous chapter, the simulated miscible pressure is lower than the saturation pressure of the original oil. It is because the original oil is volatile oil, which has little mole fraction of heavy components.

Component	Mole fraction
CO2	0.0352
N2toCH4	0.347
C2HtoC3H	0.9453
IC4toIC5	4.2406
FC6	5.3545
C7+	89.0774

Table 11—Compositions of the stock tank oil from the simulation result.

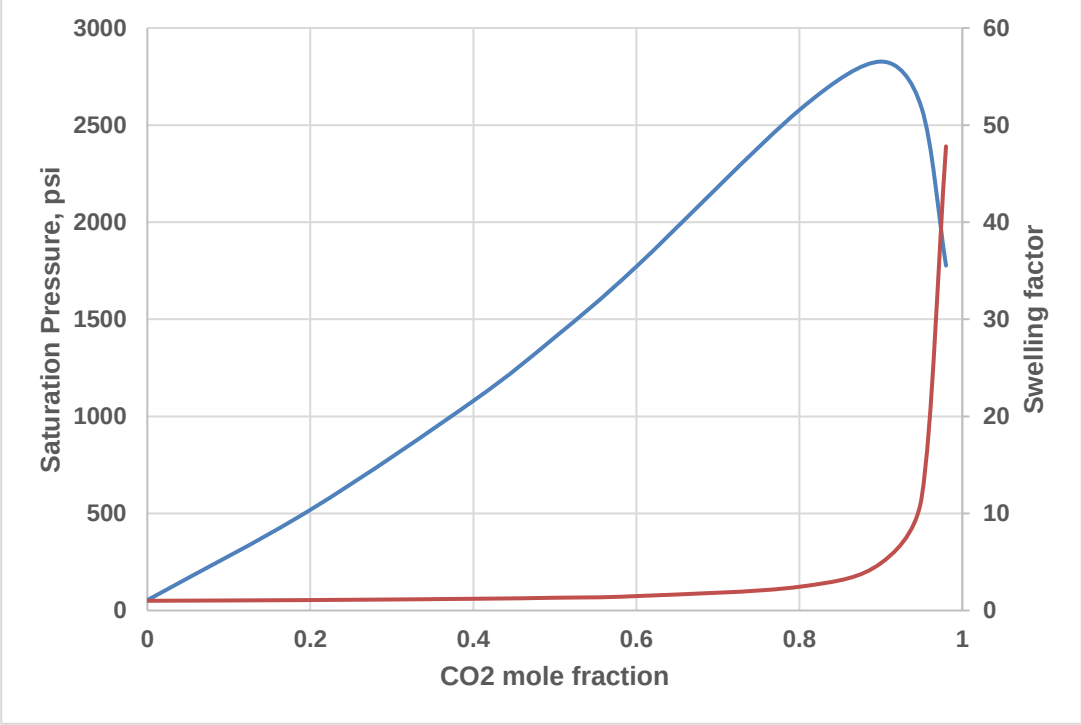

Fig. 55—The saturation pressure of the CO_2 and stock tank oil mixtures, and the corresponding swelling factor.

Slim tube test is used to determine the oil recovery factor as a function of injection pressure. Usually, 1~1.2 PV gas is injected for one run. At least four data points are needed to obtain an intersection of two trend lines, which indicates the critical pressure, named minimum miscible

pressure (MMP). The recovery factor of the run with the injection pressure above MMP is very high (>85%), and does not rise too much even if the injection pressure raises dramatically. The recovery factor of the run with the injection pressure below MMP depends on the injection pressure.

It is possible that the MMP observed from slim tube tests is lower than the actual miscibility pressure (Bon 2009). Let's use the simulation of the swelling test with the stock tank oil as an example. Since the permeability is high for the medium used in slim tube tests, the effect of the convention, or Eddy diffusion, is strong. Accordingly, the whole process can be considered under thermodynamic equilibrium. If the injection pressure is higher than the actual miscibility pressure (2827 psi), injected CO_2 is dissolved in the oil near the inlet from the beginning. At the next time step, CO_2 fraction in the oil in upstream pores near the inlet increases as a result of continues injection, and part of the mixture moves to the downstream pores, forming a single-phase mixture there with a lower CO_2 fraction. On the macro level, the front of CO_2 moves from the inlet to the outlet, and the CO_2 fraction increases continuously behind the front (**Fig. 56**). Simultaneously, oil is produced from the outlet. After 1.2 PV gas injection, most of the oil is displaced. There's still a little bit remaining oil components dissolved in the gaseous phase in the core. It is also possible that some oil condenses near the outlet since the pressure there is low. That's why the recovery factor is not 100%. If we do not consider the condensate near the outlet, this is a process of the first-contact miscible displacement since the fluid flow is always single-phase at each cross-section.

Fig. 56—Schematic diagram shows the process of first-contact miscible displacement. Red is the injected gas component, while black is the oil components.

If the injection pressure is lower than the actual miscibility pressure, for example, 2000 psi, injected CO_2 is still dissolved in the oil near the inlet at the beginning. But when the CO_2 mole fraction reaches about 70%, it becomes two phases. The lighter phase, containing more CO_2 and light hydrocarbon components, moves to the downstream pores and enriched with more light components. After transporting for some distance, this phase becomes miscible with in-situ oil, forming a single-phase region. On the macro level, a two-phase region exists after a short-period of injection, and the size of this region increases as the downstream pores lose light components and become immiscible. Oil saturation in this two-phase region continuously decreases as a result of the two-phase flow until injection stops (**Fig. 57**). Due to capillary force, remaining oil saturation there cannot decrease to zero. The size of the two-phase region at the end of injection depends on the injection pressure. If the pressure is high, the multi-contact miscibility of the light phase comes soon, and the two-phase region is short. The final recovery factor mainly depends on the size of the two-phase region. It is possible to have a high recovery factor with the multi-contact miscible displacement (Adel et al. 2016). But it cannot be as high as first-contact miscible displacement.

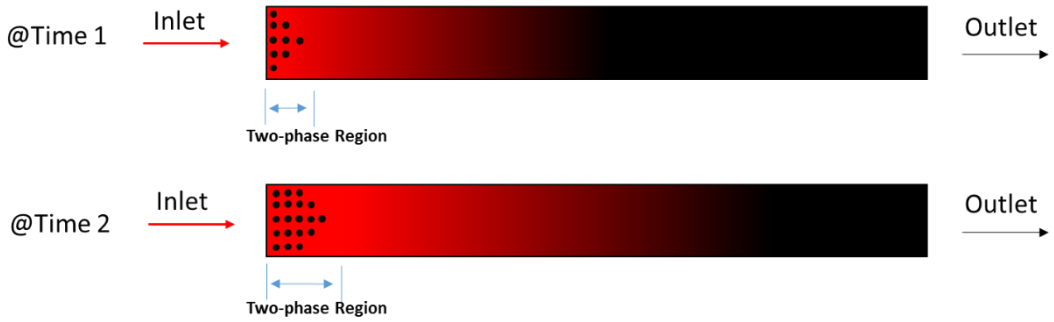

Fig. 57—Schematic diagram shows the process of multi-contact miscible displacement. A two-phase region forms near the inlet.

If the injection pressure is further lower, the two-phase region becomes very long, or even fills the whole porous medium. Thus, gas breaks through very soon, and the final recovery factor is low due to the immiscible two-phase flow. The final recovery depends on both the size of the two-phase region and the mobility ratio of the two phases.

In conclusion, either the first-contact miscible displacement or the multi-contact miscible displacement gives a high recovery factor, and the MMP obtained from slim tube test could be smaller than the actual miscibility pressure.

7.2 Analysis of Data from Core-Scale HnP Experiments in Publications

CO_2 at high pressure becomes supercritical fluid with a relatively high density. At 4000 psi, 307 °F, its density is 28 lb/ft^3, and its viscosity is 0.037 cp. It behaves more like a liquid. The lab experiment of CO_2 HnP is like the Dean-Stark extraction -- the saturated core is immersed in the solvent at high temperature. Similarly, the solvent amount is adequate in lab expreiments, which may not be true for the field-scale application.

A calculation based on EOS is conducted to show the recovery performance with the assumption of equilibrium. The oil sample used is the stock oil with the composition shown in **Table 11**. The soaking pressure used is 2200 psi, which is lower than the actual miscibility pressure, but possibly close to the MMP obtained from the slim tube test. Temperature is 307 °F. The calculation workflow is shown in **Fig. 58**, and recovery factor here is the volume of recovered stock tank oil in each cycle divided by the pore volume of the core. A case with initial CO_2/oil volume fraction of 0.9/0.1 is modeled. The high volume fraction of CO_2 used here accounts for the high pore volume of glass beads pack surrounding the core.

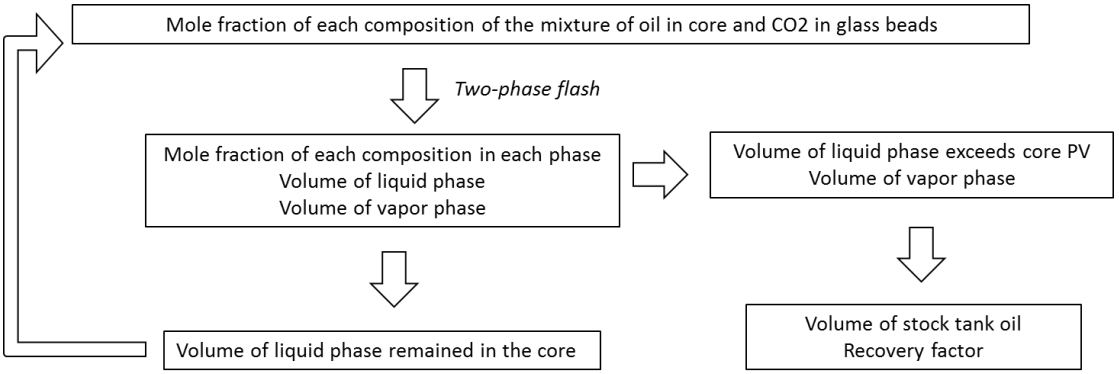

Fig. 58—Calculation workflow of the CO_2 HnP on a saturated core with the assumption of equilibrium.

	In-situ vapor volume %	In-situ liquid volume %	Recovery factor, %
Initial	90	10	0
1st huff	85.28	14.72	54.2
2nd huff	96.12	3.88	34.0

Table 12—Input and output of the two-phase flash to simulate the core-scale CO_2 HnP with the assumption of equilibrium.

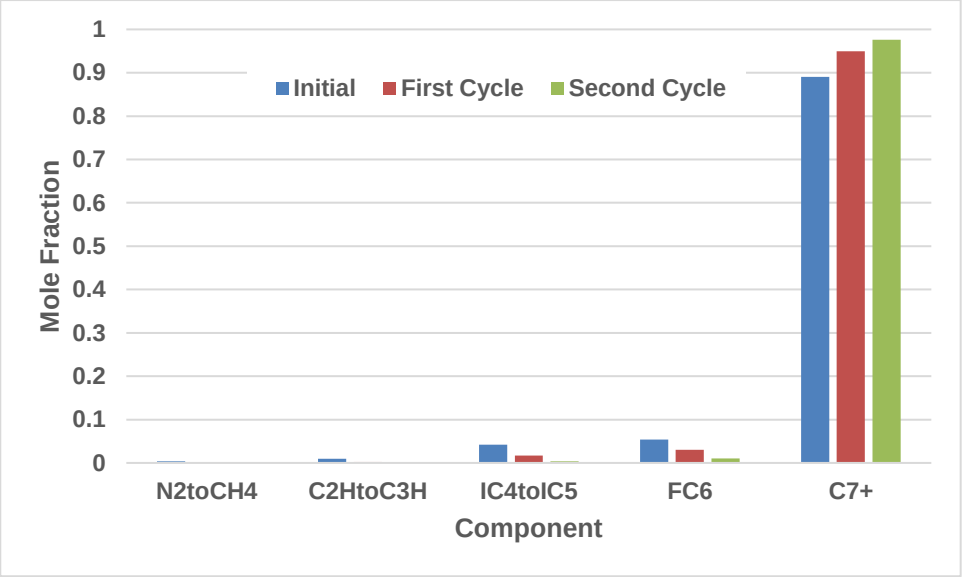

Fig. 59—Composition of the in-situ oil. Mole fraction of lighter components decreases after each cycle.

Results of in-situ vapor/liquid volume fraction and recovery factor are shown in **Table 12**. In the first cycle, in-situ oil volume expands from 10% to 14.72%, which contributes a recovery factor of 23.4%. On the other hand, vapor with the in-situ volume of 85.28% contributes a recovery factor of 30.7%. The recovery mechanism in this cycle is oil swelling and the vaporization. In the second cycle, in-situ oil volume decreases to 3.88%, indicating no liquid flows to the outlet during the puff period. All the stock tank oil recovered in the second cycle is a result of vaporization. After the two-cycle HnP, a final recovery factor of 88.2% is achieved. The composition of the in-situ oil shows a decreasing trend of the light components and an increasing trend of the heavy components during HnP cycles (**Fig. 59**), which implies an opposite trend for the stock tank oil.

This simple calculation reveals that vaporization and oil swelling, as a result of phase behavior, contributing to the recovery of oil through HnP processes. But the high recovery factor derived from the calculation is not comparable to the results of lab experiments (Adel et al. 2018;

Liu et al. 2018). It is because the actual HnP on cores cannot be treated as an equilibrium process. Equilibrium is the final state of substances which achieves the lowest Gibbs free energy through mass transport of molecular diffusion and/or convection. At equilibrium, the fugacity/chemical potential of each component in different phase are equal, and mass transport stops macroscopically. Both swelling test and slim tube test are equilibrium processes involving strong convention effect. HnP processes on tight cores have almost no convectional flow inside the cores. Mass transport mainly counts on molecular diffusion. The lower recovery factors (<50%) from lab experiments on re-saturated cores imply equilibrium is never achieved within the experiment period. Moreover, molecular diffusion during HnP is a multi-component diffusion in dense phases, which should be modeled by Maxwell-Stephane relations instead of Fick's law. In Maxwell-Stephane relations, the diffusion coefficient is an n * n matrix, where n is the number of components. The diagonal values, called the "main diffusion coefficient", determine the contribution to diffusion flux relying on the concentration of the same components in different phases. The off-diagonal diffusion coefficients have been termed the "cross-diffusion coefficient". They determine the contribution to one component's diffusion flux from the other components' concentrations, which play an important role in the dense-phase systems. Some correlations have been proposed to calculate the Maxwell-Stephane diffusion coefficients (Dutta 2009; Hoteit 2011). But it is still difficult to obtain the value of the coefficients. Instead, diffusion coefficients for Fick's law correlation are widely used in the numerical simulation (Grogan et al. 1988; Sigmund 1976b). For the multi-phase diffusion in porous media, the diffusion flux depends on the diffusion coefficients, compositions, tortuosity, porosity and saturation (Lake 1989).

Some of the phenomenon observed in the HnP lab experiments could be explained by multi-component diffusion:

1. Final recovery of high-permeability Berea (100 md) is close to that of low-permeability shale (Tovar et al. 2018b). The rock parameters affecting molecular diffusion are porosity and tortuosity, which could be similar for Berea and shale racks. So, the diffusion velocity in these two kinds of cores is close.
2. Higher operating pressure beyond MMP leads to a higher recovery factor (Adel et al. 2018). Diffusion coefficients depend on the pressure. Higher pressure results in higher diffusion coefficients.
3. Longer soak time leads to a higher recovery factor. Additionally, the recovery factor with continuous CO2 flow for the same period is low (Tovar et al. 2018a). During soak, light components gathers in the CO_2 phase, and attract the heavy components to transport from oil to CO_2. If we use Fick's law to explain the continues CO_2 flow, the result should be a over-estimated recovery factor, because the mole fraction of hydrocarbon components in CO_2 flow is nearly zero and the diffusion flux keeps maximum. The lab results showed opposite due to the fact that off-diagonal diffusion is significant for multi-component diffusion. On the other hand, the CO_2 continuous flow experiments also imply the upper limit of contribution from oil swelling effect in HnP process. The recovery factors of those range from 2-15%, contributing less than 40% to the final oil recovery. Oil swelling is a result of the dissolved CO_2, whose mole fraction in the oil should be very close in each case with the same contact period.

Note that some phenomenons such as composition shift in produced oil, volume expansion and viscosity deduction of the oil phase, are not unique with molecular diffusion. Equilibrium process as a result of the strong convention could lead to the same observation.

7.3 Review of Core-Scale and Field-Scale Numerical Simulations in Publications

Some researchers conducted numerical simulation about HnP process in tight rocks. Alfarge et al. (2018) did history match of a CO_2 flood experiment on a conventional core with permeability ranging from 800-1100 md (Hawthorne et al. 2013) by tuning the diffusivity coefficient and diffusion type. Since the original experiment includes strong convective flow, the reliability of the diffusivity coefficient obtained from history match is doubtful, which is even not shown in the paper. A following simulation study about history match of a field HnP application in Bakken formation in the same paper concludes that the molecular diffusion is the main mechanism controlling CO_2-EOR performance in shale oil formations. But the lack of the information about the production data and operation in neighboring well, together with the unreliable diffusivity coefficient, makes the conclusion weak. Torres et al. (2018) showed a history match of CO2-EOR on a Bakken core with the permeability of ~0.01 md. The procedures of the experiments were described by Jin et al. (2017), which implied significant convectional flow was involved. The diffusion coefficient obtained from the history match was $1.67*10^{-5}$ cm^2/s based on Fick's law assumption. Although diffusion was activated in their field models, the contribution of that was not reported.

Sahni and Liu (2018) run field models with molecular diffusion described by Maxwell-Stephane correlation, and found molecular diffusion had no major effect on incremental recovery. The diffusion coefficients were generated by Sigmund method embedded in the CMG simulator. The calculated values were not shown in that paper.

Sensitivity studies (Wang and Yu 2019; Yu et al. 2019) of the diffusion coefficient in Fick's law type showed that the coefficient smaller than 10^{-4} cm^2/s does not have a significant effect on

production increment on history-matched DPDK models. But the history-matched single-porosity model showed larger recovery factors as a benefit of molecular diffusion with the same coefficient value (Wang and Yu 2019). The possible reason is that the diffusion flux depends on porosity and pressure, which may be elevated to achieve history match with the single-porosity model. Thus, the effect of molecular diffusion is exaggerated. However, the detail about the parameters used for the single-porosity model was not announced in that paper.

Zou (2015) showed both the calculated diffusion coefficients according to Sigmund correlation (Sigmund 1976a, 1976b) and tuned diffusion coefficient by history matching HnP experiments on preserved sidewall shale cores (Tovar et al. 2014). The value of those coefficients is within the range of 10^{-8} - 10^{-7} cm^2/s. And the reservoir-scale simulation on a single-porosity model in this publication demonstrated that diffusion had little contribution.

To sum up the observation and analysis from publications, multi-component diffusion following Maxwell-Stephane correlation does exist for CO_2 HnP in tight rock. If there is no convectional flow, the main recovery mechanisms are the oil swelling and the asynchronous mass transport of oil component to the CO_2 phase. If there is convectional flow, the additional recovery mechanism is the viscosity reduction of the oil phase. Note that convection can also lead to oil swelling, component' mass transport, and viscosity reduction. If there is relatively strong convectional flow in the reservoir, the benefits from diffusion flux may become minor.

For this study, molecular diffusion is not included, because:

1. It is hard to get the true molecular diffusion coefficients for each component for the Maxwell-Stephane correlation.
2. Actual molecular diffusion may be slow, and hardly contribute too much during the relative short HnP process. The reported CO_2 diffusion coefficients in simple multi-

component systems have the order of 10^{-5} - 10^{-4} cm^2/s (Grogan et al. 1988; Renner 1988).

3. The purpose of this study is to understand the influence of fracture geometry on HnP performance. Molecular diffusion should not affect the conclusions.

7.4 DFN Simulations of Field-Scale CO2 HnP

The DFN model generated according to the FMI log and the DAS/DTS response is used for the CO_2 HnP study. The detail of this model is described in Section 5.2. The simulation results are upscaled to a full horizontal well with the length of 4200 ft.

7.4.1 CO_2 HnP with Reservoir Pressure above Bubble Point

Since many of the wells in Eagle Ford shale and Wolfcamp shale produce oil in black-oil type, this simulation study begins with the simplest situation: reservoirs are still in single phase at the beginning of HnP application. Because EOS and initial composition available are for volatile oil, the reservoir pressure is elevated from 5000 psi to 7700 psi to forbid the reservoir gas cap, which is still a reasonable value for Eagle Ford formation. Additionally, the BHP is constrained as 4200 psi, which is higher than the bubble point pressure of 4191 psi. The true miscibility pressure of CO_2 with this volatile oil is lower than the bubble point pressure from the EOS calculation.

A five-year depletion with well constrained by a minimum BHP of 4200 psi is performed as the base case. CO_2 HnP begins in the third year, and is scheduled as cycles of one-month injection and one-month production. Injection pressures tested are 5000 psi and 8000 psi. The injection rate is constrained below 10 MMscf/day. Simulation results are shown in **Fig. 60**. It is

obvious that higher injection pressure results in higher recovery factor. The incremental recovery factor based on primary depletion from the case of 5000 psi injection pressure is 29.2%, while that from the case of 8000 psi injection pressure is 59.9%.

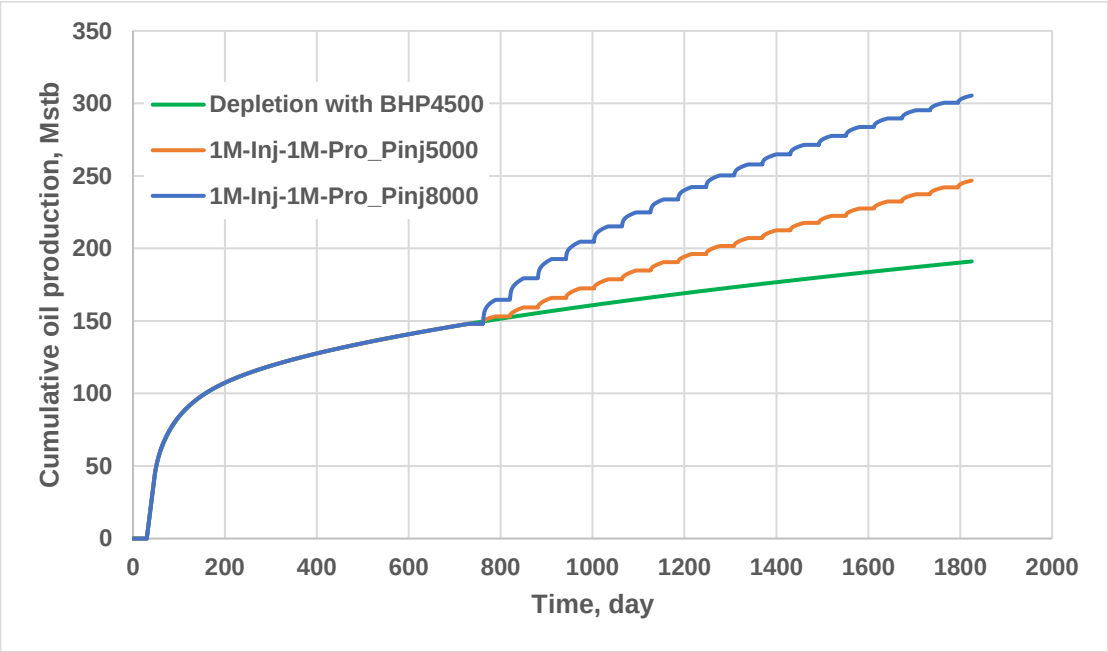

Fig. 60—Cumulative oil production of depletion and CO_2-HnP with an injection pressure of 5000 psi and 8000 psi. One HnP cycle includes one-month injection and one-month production.

Different HnP schedules are tested with the injection pressure of 8000 psi. A case with cycles of two-month injection and two-month production (2M-Inj-2M-Pro) was run, and the result is shown in Fig. 61. Its incremental recovery factor is 70.8%, which is higher than that of the one-month injection and one-month production (1M-Inj-1M-Pro) case. The reason is that the 1M-Inj-1M-Pro schedule leaves more CO_2-enriched light oil in the reservoir in the production period,

which is pushed back to the deep reservoir in the next injection period. The short cycling period makes the HnP process less efficient.

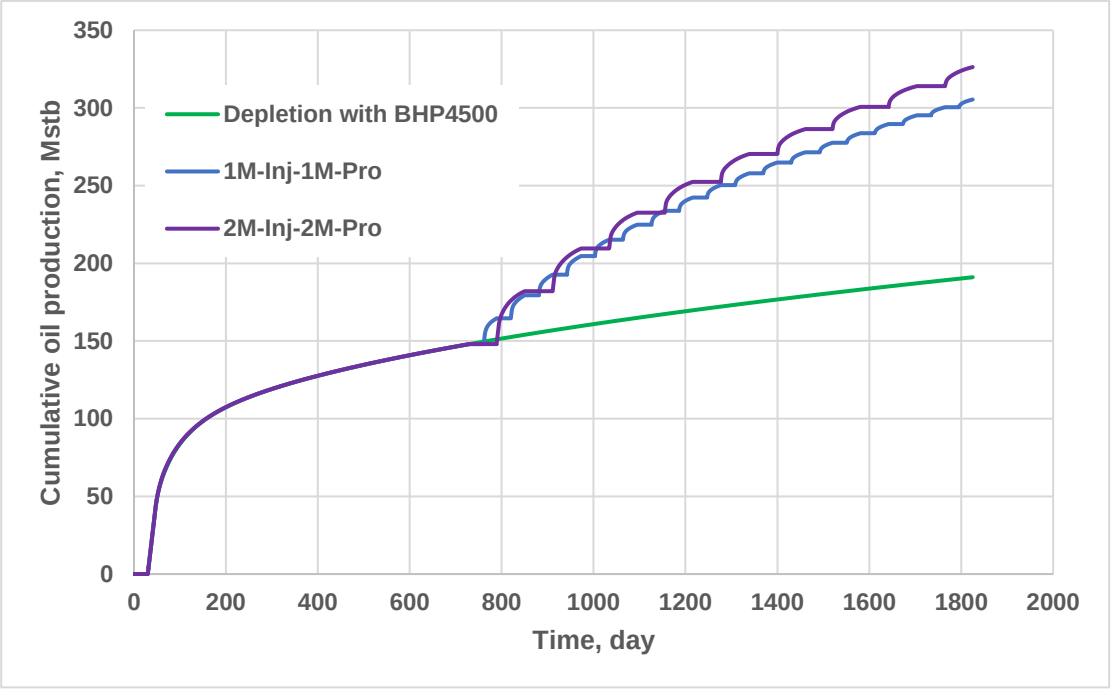

Fig. 61—Cumulative oil production of depletion and CO_2-HnP with different cycling schedule. One schedule is cycling of one-month injection and one-month production, and the other schedule is cycling of two-month injection and two-month production.

Fig. 62 shows that the pressure of the near-well region is charged firstly due to the high fracture density there, and the pressure spreads to the deeper reservoir with continues injection. There is no obvious change of pressure in the deep reservoir above 600 ft from the well, although one hydraulic fracture plane propagates 1500 ft. **Fig. 63** shows the gas saturation map of reservoir area with high fracture density. There is no two-phase grid block because of the assumption of equilibrium. CO_2 entering pores forms a single-phase fluid with in-situ oil components. The single-phase mixture spreads as the injection of CO_2 continues.

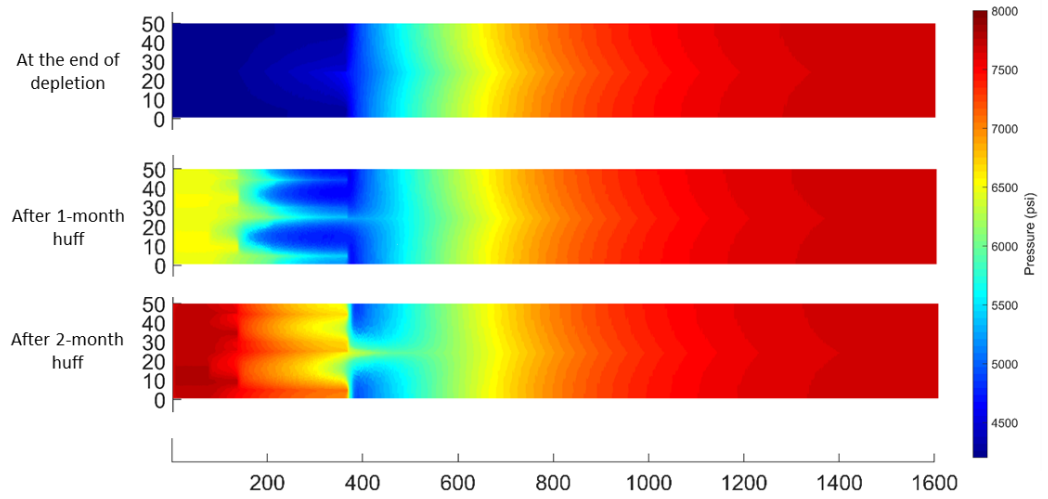

Fig. 62—Pressure map of the full reservoir at the end of depletion, after one-month huff process and after two-month huff process with 8000 psi injection pressure. The pressure is charged in the near well region, where high fracture density exists.

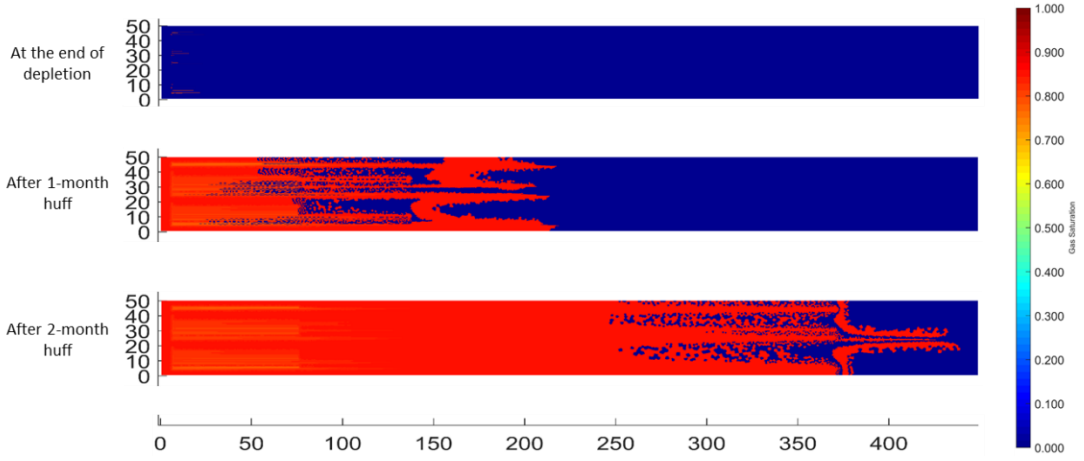

Fig. 63—Gas saturation map of reservoir area within 450 ft at the end of depletion, after one-month huff process and after two-month huff process with 8000 psi injection pressure.

The gas injection rate of the 2M-Inj-2M-Pro case shows that there is no decline in each huff period (**Fig. 64**). Thus, more gas could be injected during each cycle for this fracture network.

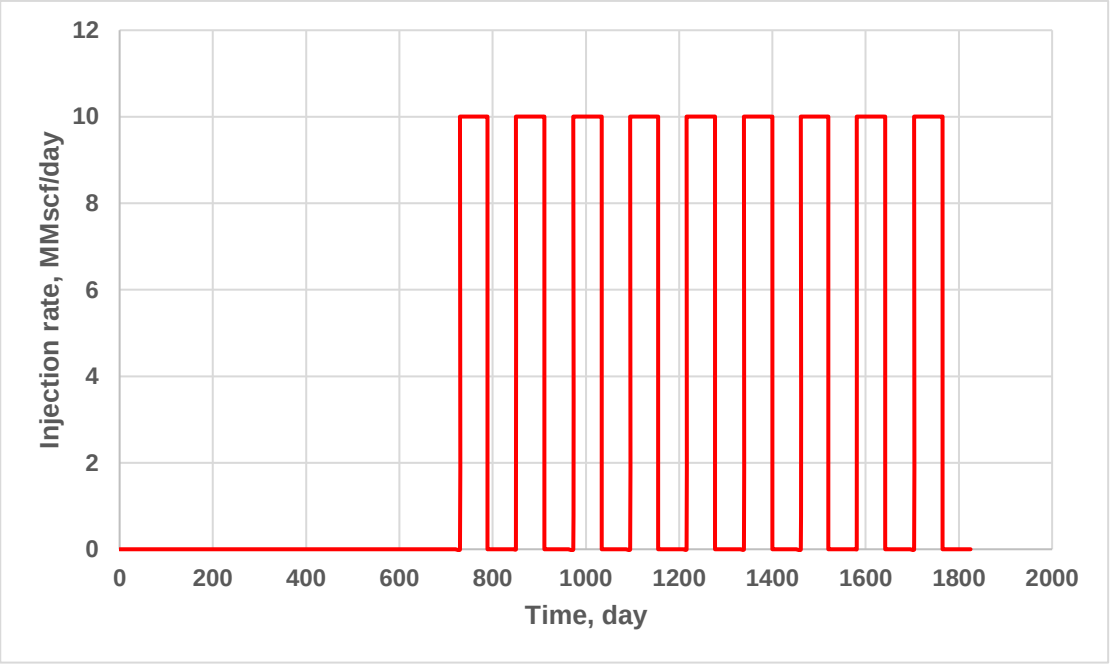

Fig. 64—CO_2 injection rate of the 2M-Inj-2M-Pro case with an injection pressure of 8000 psi.

HnP with lean gas is also tested with the injection pressure of 8000 psi (**Fig. 65**). Compared to CO_2, lean gas recovers more oil, resulting in an incremental recovery factor of 79.1%. One of the reasons is that a large portion of the hydrocarbon from injected lean gas could stay in the stock tank, resulting in a lower GOR. Another reason is that the viscosity of the mixture is lower with lean gas (**Fig. 66**), which increases the convectional flow during puff processes.

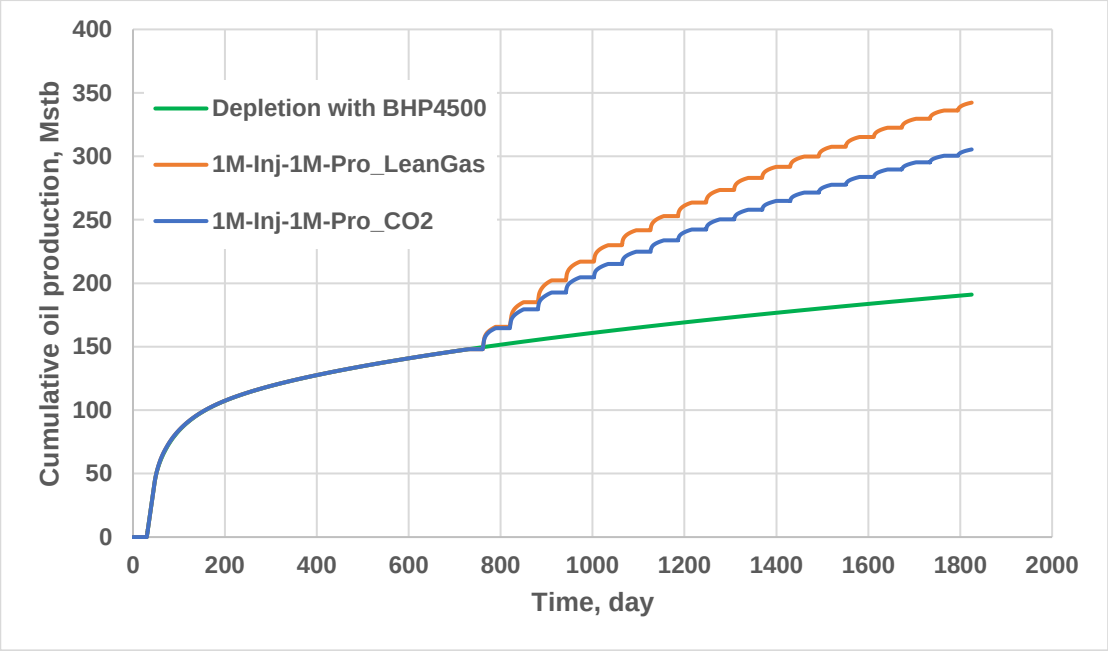

Fig. 65—Cumulative oil production of depletion and HnP with different injection compositions. One injected gas is CO_2, and the other is lean gas.

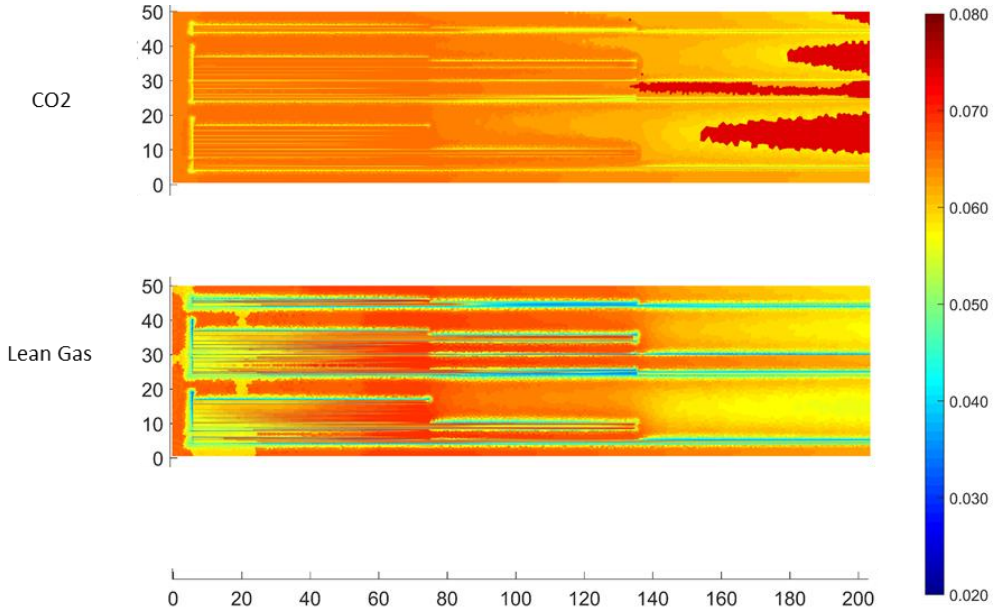

Fig. 66—Viscosity map of the mixture after one-month huff for the cases of CO_2 and lean gas injection.

7.4.2 CO2 HnP with Reservoir Pressure below Bubble Point

A reservoir model with the same setup but the initial pressure of 5000 psi is assumed. The producer BHP is constrained at 1500 psi. Gas injection pressure is 5000 psi, and the rate is constrained below 10 MMscf/day. Cumulative oil production results of cases with different CO_2-HnP schedule are shown in **Fig. 67**. The two-month injection two-month production scenario achieves the highest incremental recovery factor of 124.9%, which is higher than that of the case with the same scenario but in a reservoir above bubble point (79.1%). This is because, for the depleted reservoir with in-situ gas phase existing, the gas phase has higher mobility, but the fraction of heavy components in the gas phase is low. Thus, plenty of gas produces, which damages the oil production rate. The gas injection will pressurize the near fracture region, forming single phase to improve the flux of heavy components. **Fig. 68** shows the oil saturation evolution with CO_2 injection. At the beginning, the reservoir is in two-phase condition with an oil saturation of ~0.3. With gas injected, the oil saturation increases due to pressurization. With the gas continuous injection, a high-saturation oil bank (red) forms and moves towards the deeper reservoir. The region adjacent to fractures is occupied by CO_2-rich phase (blue).

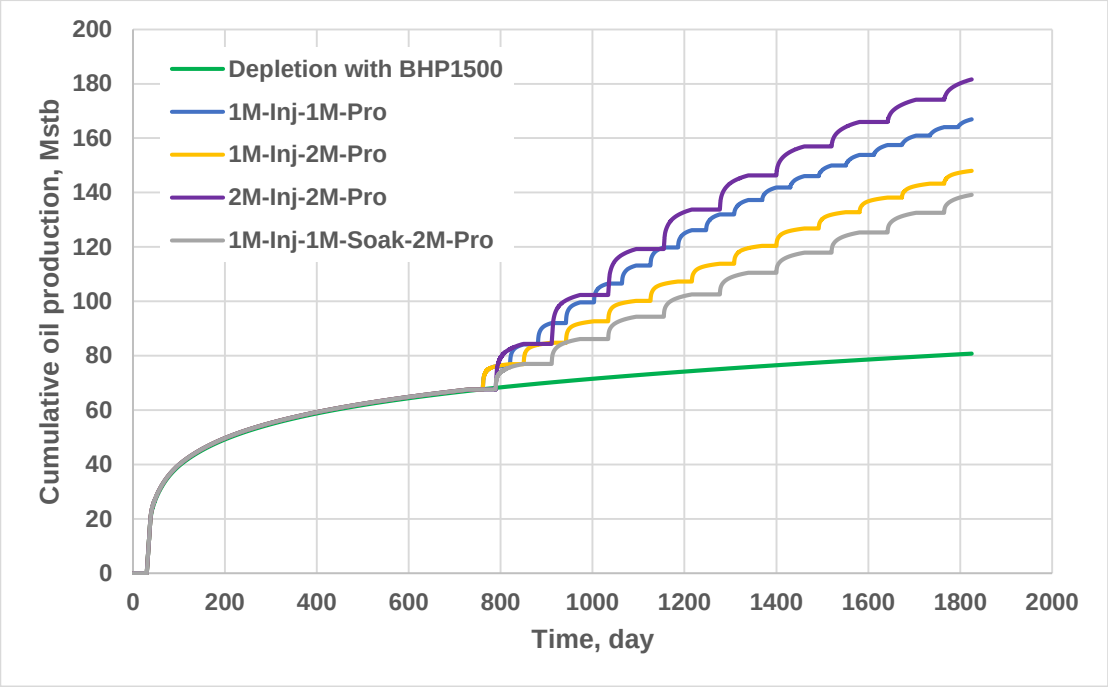

Fig. 67—Cumulative oil production of depletion and CO_2-HnP with different cycling schedule. One schedule is cycling of one-month injection and one-month production, and the other schedule is cycling of two-month injection and two-month production.

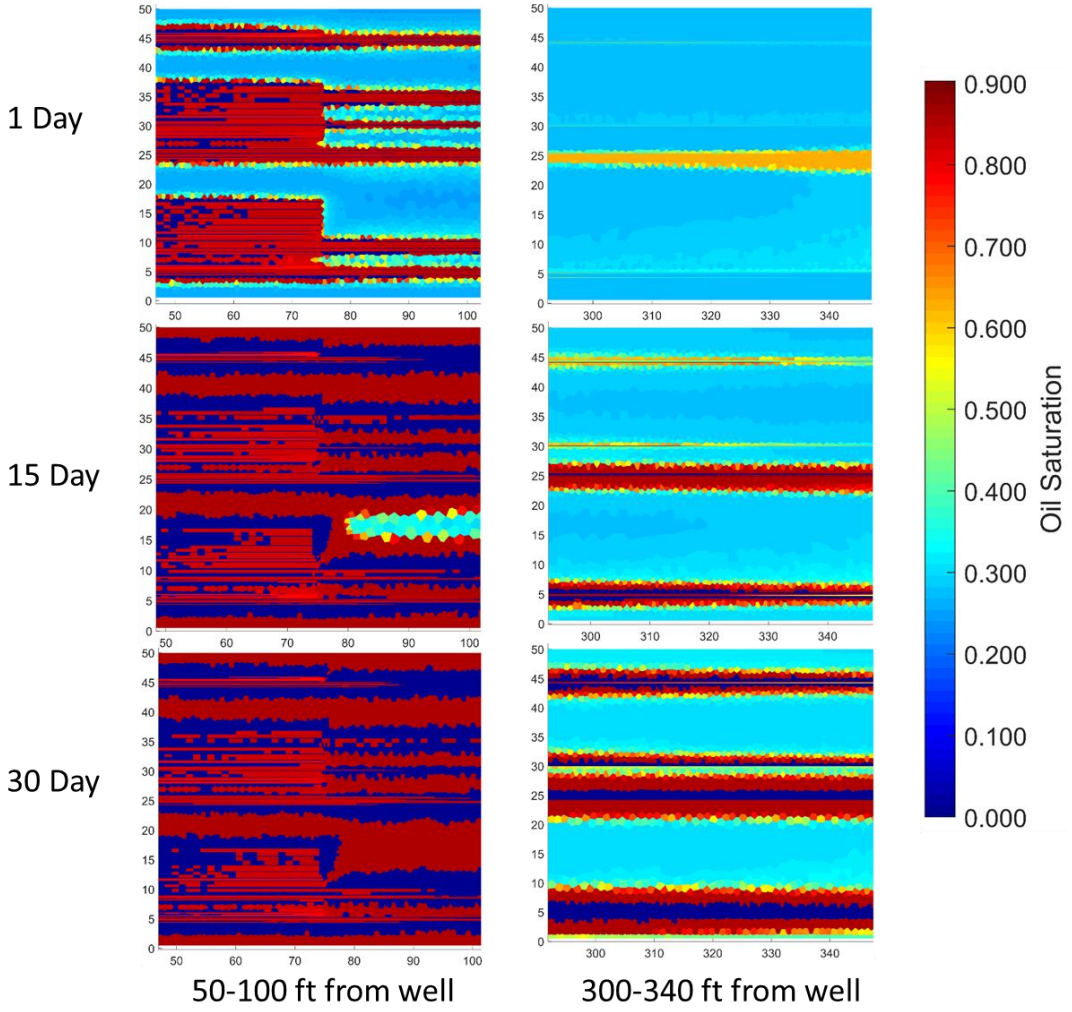

Fig. 68—Oil saturation map during the injection of CO_2. Left is the near well region while right is the far field region. CO_2 pushes oil to form an oil bank with ~3 ft thickness surrounding fractures with some distance. A band with 1 - 2 ft is formed by CO_2–rich phase adjacent to the fractures.

The effect of operation timing with the same amount of injection is investigated. Three cases are compared: one-month injection one-month production (1M-Inj-1M-Pro), one-month injection two-month production (1M-Inj-2M-Pro) and one-month injection/one-month soak/one-month production (1M-Inj-1M-Soak-1M-Pro). The production results of the 3-year HnP process

are shown in **Fig. 67**. To compare the effect with the same injection amount, the production of 8 cycles HnP are shown in **Fig. 69**. Cumulative production of 1M-Inj-1M-Pro and 1M-Inj-2M-Pro are very close, indicating the benefit from the gas injection is gone after one-month production. The case with one-month soak has a slightly higher production. It is because pressure gradient and CO_2 composition gradient exist in the outer side of fracture swarms once injection stops, and CO_2 will transport further to the matrix and reduce the viscosity of additional amount of oil during soak period (**Fig. 70**). Soak may have a more significant effect if a local equilibrium is not achieved, which may be possible in the real field applications. **Fig. 70** also shows that the CO_2 fraction is low inside the fracture swarms (light blue to yellow), but it is high at the outer boundary of the swarms (red). The reason is that pressure of the matrix rock inside the swarms is quickly built up, and CO_2 invasion there is restrained. At the outer boundary, CO_2 is easier to be injected and accumulated, because the far-field fluid with relatively low pressure is compressed, providing more volume for CO_2 entrance. This phenomenon is unable to be observed from other DFN methods using big grid size.

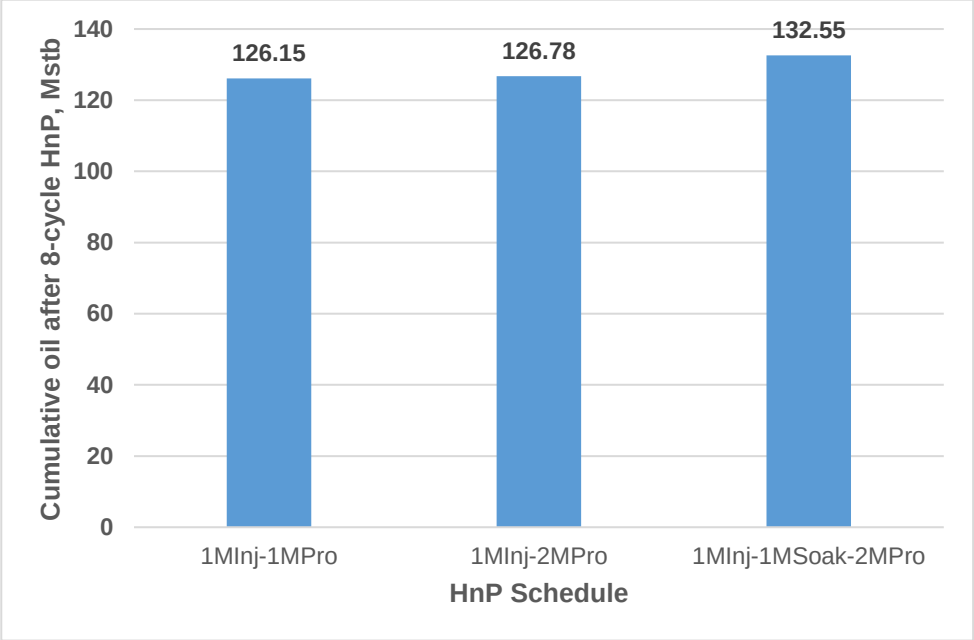

Fig. 69—Cumulative oil production at the end of eight cycles of HnP.

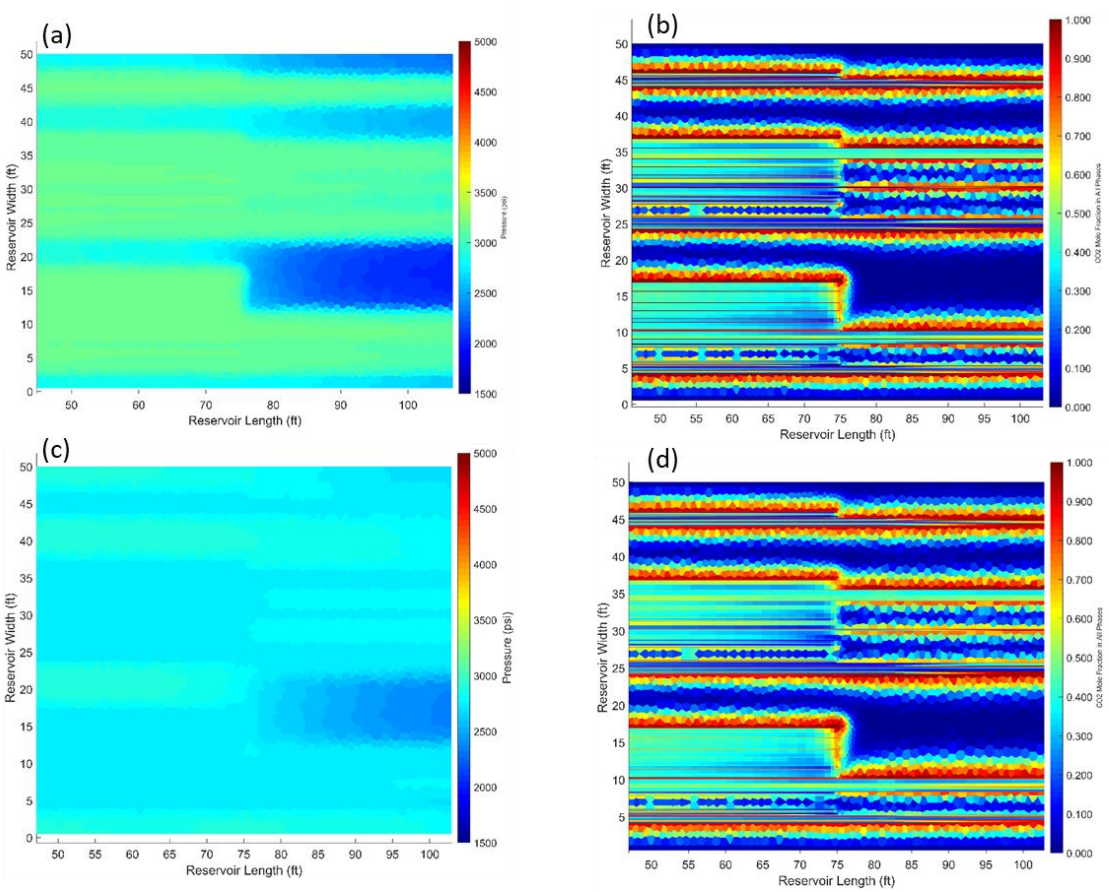

Fig. 70—Pressure map and CO_2 mole fraction map of area 50-100 ft away from the well. (a) Pressure distribution before after injection, before soak; (b) CO_2 mole fraction in all phases before soak; (c) Pressure distribution after soak; (d) CO_2 mole fraction in all phases after soak.

7.4.3 CO_2 HnP with Injection Pressure below Bubble Point/MMP

Performance of CO_2 HnP with the operating pressure below bubble point/MMP is investigated on reservoirs with an initial pressure of 8000 psi. The well is constrained by 1500 psi BHP during production. For this volatile oil, the CO_2 MMP is lower than the bubble point. The HnP schedule of all the cases in this section is one-month injection followed by one-month

production. The results of cases with an injection pressure of 2300 psi, 2500 psi, and 2700 psi are shown in **Fig. 71**. Unlike the observation from core-scale HnP, even though the operating pressure is below MMP, all the cases show obvious recovery increment, which are 20.4%, 30.1%, and 37.2%, respectively. The reason is that the volume of vapor phase near fracture decrease after the CO_2 injection, and the mobility of the oil phase increases. Moreover, with higher injection pressure, the ratio of oil-phase volume to vapor-phase volume increases, resulting in higher oil production.

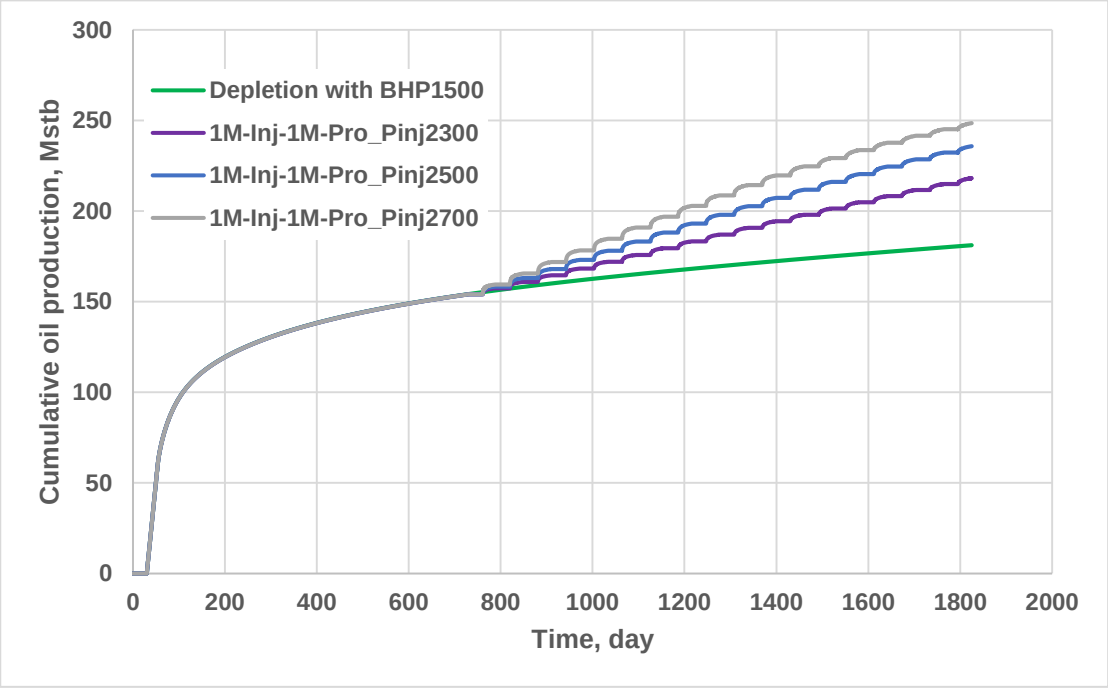

Fig. 71—Cumulative oil production of depletion and CO_2-HnP with different injection pressure below MMP.

CHAPTER VIII

CONCLUSIONS AND RECOMMENDATIONS

In terms of the generation of reservoir models, two important aspects are investigated, which are gridding algorithms and generation of DFN geometry. Field observation of high-density complex fracture system indicates the significance of using unstructured gridding in reservoir modeling to capture the fracture geometry with minimum grid number. In this study, gridding algorithms are developed to refine the fracture intersections and tips and reduce grid distortion. The sensitivity study on multi-phase flow indicates the right way to run the reservoir simulation with fine grids.

The differences caused by the gridding approaches and numerical methods are systematically tested on reservoirs with equally distributed orthogonal fractures. The PEBI gridding algorithms are verified through comparison with single-porosity and dual-porosity models. Furthermore, the importance of PEBI grid is revealed through the simulation of models with consideration of actual permeability contrast and fracture discontinuity.

In order to deal with DFN geometry, three workflows are proposed to generate DFN with different kinds of field data, which are MS-based, outcrop-based, and FMI-based. Note that simulation of fracture propagation is not involved in this study mainly because the current propagation simulations assume homogeneous medium, resulting in large deviation with the actual situation. The generated DFN are then transferred to reservoir models through discretization by PEBI grid, and such reservoir models are calibrated by production data. These approaches are not independent of each other. The more data utilized, the less uncertainty the models have.

Unfortunately, it is usually difficult to find a well with complete sets of data involving MS, outcrop map, FMI log and production history.

Reservoir models for fractured well in tight rocks are usually used to obtain estimated ultimate recovery (EUR) and study well communication in the industry. These tasks can be accomplished by modeling with either structure grid or unstructured grid. However, EOR processes in fractured reservoir usually involve the severe uneven distribution of phases and components in the space domain and rapid change of phase saturation and component fractions in the time domain. Thus, the PEBI grid is preferred for EOR study. Simulation of the EOR process is carried out in this study, showing some results which are difficult to be obtained in lab experiments and simulation with a structured grid.

To sum up, the main conclusions are listed below:

- Dual-porosity method is not accurate if the transient period of fracture-matrix flow is long. Additionally, the dual-porosity method cannot deal with fractures in poor connectivity.
- DFN geometry can is by utilizing various kinds of information, such as microseismicity, outcrop map, and FMI log. The DFN reservoir model can be calibrated by matching historical data, and parameters tuned are within a reasonable range from publications.
- Surfactant spontaneous imbibition with one-month soak shows marginal recovery enhancement on matrix rock. The desaturation effect and the alteration of fracture relative permeability curves with surfactant soaking may lead to more promising recovery enhancement. But the data is not available now, and further lab investigation is suggested.

- Injected gas can enter the matrix pores of reservoirs after two-year depletion on account of the total compressibility of rock and reservoir fluids. Oil swelling may not be a recovery mechanism with the assumption of phase equilibrium, because the total volume is shrinking in pores when the mixture of the initial two fluids is forming a single phase.
- Re-pressurization and viscosity deduction are the main recovery mechanisms for gas HnP. For reservoirs below bubble-point, another recovery mechanism is the improvement of heavy components' flux.
- In this study, lean gas shows better performance because its mixture with the volatile oil has a lower viscosity.
- Either adding a soak period or increasing portion of production period in each cycle has a minor effect on production enhancement. Again, equilibrium is assumed here.
- Maxwell-Stephane coefficients are suggested for an accurate match with lab experiments. After the match, the ratio of convection flux to molecular diffusion flux can be studied with field-scale models.
- DFN with the unstructured grid is a good method to study the EOR processes with rapid change in phase saturation and component fraction. More details can be observed by assigning very fine grids near flowing channels. Compared to other continuum methods, the study of field application by this method will be more reliable by properly utilizing field data.

REFERENCES

Adel, I.A., Tovar, F.D., and Schechter, D.S. 2016. Fast-Slim Tube: A Reliable and Rapid Technique for the Laboratory Determination of MMP in CO2 - Light Crude Oil Systems. Presented at the SPE Improved Oil Recovery Conference, Tulsa, Oklahoma, USA. SPE-179673-MS. https://doi.org/10.2118/179673-MS.

Adel, I.A., Tovar, F.D., Zhang, F. et al. 2018. The Impact of MMP on Recovery Factor During CO2 – EOR in Unconventional Liquid Reservoirs. Presented at the SPE Annual Technical Conference and Exhibition, Dallas, Texas, USA. SPE-191752-MS. https://doi.org/10.2118/191752-MS.

Ahmed, T.H. 1989. *Hydrocarbon Phase Behavior. Tarek Ahmed*. Contributions in Petroleum Geology & Engineering: 7: Houston : Gulf Pub. Co., [1989].

Alfarge, D., Wei, M., and Bai, B. 2018. Integrated Investigation of CO2-EOR Mechanisms in Huff-N-Puff Operations Based on History Matching Results. Presented at the SPE Improved Oil Recovery Conference, Tulsa, Oklahoma, USA. SPE-190234-MS. https://doi.org/10.2118/190234-MS.

Alvarez, J.O., Saputra, I.W.R., and Schechter, D.S. 2017a. Potential of Improving Oil Recovery with Surfactant Additives to Completion Fluids for the Bakken. *Energy & Fuels* **31** (6): 5982-5994. https://doi.org/10.1021/acs.energyfuels.7b00573.

Alvarez, J.O., Saputra, I.W.R., and Schechter, D.S. 2018a. The Impact of Surfactant Imbibition and Adsorption for Improving Oil Recovery in the Wolfcamp and Eagle Ford Reservoirs. *SPE Journal* **23** (06): 2103-2117. SPE-187176-PA. https://doi.org/10.2118/187176-PA.

Alvarez, J.O. and Schechter, D.S. 2016a. Altering Wettability in Bakken Shale by Surfactant Additives and Potential of Improving Oil Recovery During Injection of Completion Fluids. Presented at the SPE Improved Oil Recovery Conference, Tulsa, Oklahoma, USA. SPE-179688-MS. https://doi.org/10.2118/179688-MS.

Alvarez, J.O. and Schechter, D.S. 2016b. Wettability, Oil and Rock Characterization of the Most Important Unconventional Liquid Reservoirs in the United States and the Impact on Oil Recovery. Presented at the SPE/AAPG/SEG Unconventional Resources Technology Conference, San Antonio, Texas, USA. URTEC-2461651-MS. https://doi.org/10.15530/URTEC-2016-2461651.

Alvarez, J.O. and Schechter, D.S. 2017. Wettability Alteration and Spontaneous Imbibition in Unconventional Liquid Reservoirs by Surfactant Additives. *SPE Reservoir Evaluation & Engineering* **20** (01): 107-117. SPE-177057-PA. https://doi.org/10.2118/177057-PA.

Alvarez, J.O., Tovar, F.D., and Schechter, D.S. 2017b. Improving Oil Recovery in Unconventional Liquid Reservoirs by Soaking-Flowback Production Schedule with Surfactant Additives. Presented at the SPE Liquids-Rich Basins Conference - North America, Midland, Texas, USA. SPE-187483-MS. https://doi.org/10.2118/187483-MS.

Alvarez, J.O., Tovar, F.D., and Schechter, D.S. 2018b. Improving Oil Recovery in the Wolfcamp Reservoir by Soaking/Flowback Production Schedule with Surfactant Additives. *SPE Reservoir Evaluation & Engineering* **21** (04): 1083-1096. SPE-187483-PA. https://doi.org/10.2118/187483-PA.

Baca, R.G., Arnett, R.C., and Langford, D.W. 1984. Modelling Fluid Flow in Fractured-Porous Rock Masses by Finite-Element Techniques. *International Journal for Numerical Methods in Fluids* **4** (4): 337-348. 10.1002/fld.1650040404.

Bao, A. and Gildin, E. 2017. Data-Driven Model Reduction Based on Sparsity-Promoting Methods for Multiphase Flow in Porous Media. Presented at the SPE Latin America and Caribbean Petroleum Engineering Conference, Buenos Aires, Argentina. SPE-185514-MS. https://doi.org/10.2118/185514-MS.

Bao, A., Gildin, E., and Zalavadia, H. 2018. Development of Proxy Models for Reservoir Simulation by Sparsity Promoting Methods and Machine Learning Techniques. *Proc*., ECMOR XVI-16th European Conference on the Mathematics of Oil Recovery, https://doi.org/10.3997/2214-4609.201802180

Bao, A., Hazlett, R.D., and Babu, D.K. 2017. A Discrete, Arbitrarily Oriented 3d Plane-Source Analytical Solution to the Diffusivity Equation for Modeling Reservoir Fluid Flow. *SPE Journal* **22** (05): 1609-1623. SPE-185180-PA. https://doi.org/10.2118/185180-PA.

Barba, R.E., Jr. and Cutia, A.S. 1992. Evaluating Horizontal Well Potential in the Spraberry Trend. Presented at the Permian Basin Oil and Gas Recovery Conference, 18-20 March, Midland, Texas. SPE-23949-MS. http://doi.org/10.2118/23949-MS.

Batchelor, A.S., Baria, R., and Hearn, K. 1983. Monitoring the Effects of Hydraulic Stimulation by Microseismic Event Location: A Case Study. Presented at the SPE Annual Technical Conference and Exhibition, 5-8 October, San Francisco, California. SPE-12109-MS. http://doi.org/10.2118/12109-MS.

Beckner, B.L., Chan, H.M., Mcdonald, A.E. et al. 1991. Simulating Naturally Fractured Reservoirs Using a Subdomain Method. Presented at the SPE Symposium on Reservoir Simulation, Anaheim, California. SPE-21241-MS. https://doi.org/10.2118/21241-MS.

Beggs, D.H. and Brill, J.P. 1973. A Study of Two-Phase Flow in Inclined Pipes. *Journal of Petroleum Technology* **25** (05): 607-617. SPE-4007-PA. http://doi.org/10.2118/4007-PA.

Beggs, H.D. 1987. Oil System Correlations (1987 Peh Chapter 22). Society of Petroleum Engineers.

Belayneh, M. and Cosgrove, J.W. 2004. Fracture-Pattern Variations around a Major Fold and Their Implications Regarding Fracture Prediction Using Limited Data: An Example from the Bristol Channel Basin. *Geological Society, London, Special Publications* **231** (1): 89. https://doi.org/10.1144/GSL.SP.2004.231.01.06.

Blyton, C.a.J., Gala, D.P., and Sharma, M.M. 2015. A Comprehensive Study of Proppant Transport in a Hydraulic Fracture. Presented at the SPE Annual Technical Conference and Exhibition, 28-30 September, Houston, Texas, USA. SPE-174973-MS. http://doi.org/10.2118/174973-MS.

Bon, J. 2009. *Laboratory and Modelling Studies on the Effects of Injection Gas Composition on Co_2-Rich Flooding in Cooper Basin, South Australia*. Ph.D., University of Adelaide

Caillabet, Y., Fabrie, P., Landereau, P. et al. 2000. Implementation of a Finite-Volume Method for the Determination of Effective Parameters in Fissured Porous Media. *Numerical Methods for Partial Differential Equations* **16** (2): 237-263. https://doi.org/10.1002/(sici)1098-2426(200003)16:2<237::Aid-num6>3.0.Co;2-w.

Caillabet, Y., Fabrie, P., Lasseux, D. et al. 2001. Computation of Large-Scale Parameters for Dispersion in Fissured Porous Medium Using Finite-Volume Method. *Computational Geosciences* **5** (2): 121-150. 10.1023/a:1013140922402.

Chai, Z., Yan, B., Killough, J.E. et al. 2016. Dynamic Embedded Discrete Fracture Multi-Continuum Model for the Simulation of Fractured Shale Reservoirs. Presented at the International Petroleum Technology Conference, Bangkok, Thailand. IPTC-18887-MS. https://doi.org/10.2523/IPTC-18887-MS.

Chen, C.-Y., Li, K., and Horne, R.N. 2004. Experimental Study of Phase Transformation Effects on Relative Permeabilities in Fractures. Presented at the SPE Annual Technical Conference and Exhibition, Houston, Texas. SPE-90233-MS. https://doi.org/10.2118/90233-MS.

Chierici, G.L., Ciucci, G.M., and Sclocchi, G. 1974. Two-Phase Vertical Flow in Oil Wells - Prediction of Pressure Drop. *Journal of Petroleum Technology* **26** (08): 927-938. SPE-4316-PA. http://doi.org/10.2118/4316-PA.

Coats, K.H. 1980. An Equation of State Compositional Model. *Society of Petroleum Engineers Journal* **20** (05): 363-376. SPE-8284-PA. https://doi.org/10.2118/8284-PA.

Correia, M., Maschio, C., and Schiozer, D.J. 2012. A Procedure for Upscaling a Complex Fractured Reservoir Model Using near-Well Refinement. Presented at the SPE Latin America and Caribbean Petroleum Engineering Conference, Mexico City, Mexico. SPE-153558-MS. https://doi.org/10.2118/153558-MS.

Dahi-Taleghani, A. and Olson, J.E. 2011. Numerical Modeling of Multistranded-Hydraulic-Fracture Propagation: Accounting for the Interaction between Induced and Natural Fractures. *SPE Journal* **16** (03): 575-581. SPE-124884-PA. https://doi.org/10.2118/124884-PA.

Deghmoum, A.H., Tiab, D., and Mazouzi, A. 2001. Relative Permeability in Dual Porosity Porous Media. *Journal of Canadian Petroleum Technology* **40** (12): 32-42. PETSOC-01-12-01. http://doi.org/10.2118/01-12-01.

Du, S., Yoshida, N., Liang, B. et al. 2015. Dynamic Modeling of Hydraulic Fractures Using Multisegment Wells. Presented at the SPE Liquids-Rich Basins Conference - North America, Midland, Texas, USA. SPE-175540-MS. https://doi.org/10.2118/175540-MS.

Dutta, A. 2009. *Multicomponent Gas Diffusion and Adsorption in Coals for Enhanced Methane Recovery*, Stanford University

Dyes, A.B. and Johnston, O.C. 1953. Spraberry Permeability from Build-up Curve Analyses. *Journal of Petroleum Technology* **5** (05). SPE-228-G. http://doi.org/10.2118/228-G.

Edwards, D.A., Cheng, N., Dombrowsky, T.P. et al. 2013. Representing Hydraulic Fractures Using a Multilateral, Multisegment Well in Simulation Models. Presented at the SPE Reservoir Simulation Symposium, The Woodlands, Texas, USA. SPE-163644-MS. https://doi.org/10.2118/163644-MS.

Ferrill, D.A., Mcginnis, R.N., Morris, A.P. et al. 2014. Control of Mechanical Stratigraphy on Bed-Restricted Jointing and Normal Faulting: Eagle Ford Formation, South-Central Texasmechanical Stratigraphy, Faults and Fractures in the Eagle Ford of Texas. *AAPG Bulletin* **98** (11): 2477-2506. https://doi.org/10.1306/08191414053.

Friedrich, M. and Monson, G. 2013. Two Practical Methods to Determine Pore Pressure Regimes in the Spraberry and Wolfcamp Formations in the Midland Basin. Presented at the

SPE/AAPG/SEG Unconventional Resources Technology Conference, 12-14 August, Denver, Colorado, USA. URTEC-1582132-MS. https://doi.org/10.15530/URTEC-1582132-MS.

Fussell, D.D. and Yanosik, J.L. 1978. An Iterative Sequence for Phase-Equilibria Calculations Incorporating the Redlich-Kwong Equation of State. *Society of Petroleum Engineers Journal* **18** (03): 173-182. SPE-6050-PA. https://doi.org/10.2118/6050-PA.

Gale, J.F.W., Elliott, S.J., and Laubach, S.E. 2018. Hydraulic Fractures in Core from Stimulated Reservoirs: Core Fracture Description of HFTS Slant Core, Midland Basin, West Texas. Presented at the SPE/AAPG/SEG Unconventional Resources Technology Conference, Houston, Texas, USA. https://doi.org/10.15530/URTEC-2018-2902624.

Gale, J.F.W., Laubach, S.E., Olson, J.E. et al. 2014. Natural Fractures in Shale: A Review and New Observationsnatural Fractures in Shale: A Review and New Observations. *AAPG Bulletin* **98** (11): 2165-2216. https://doi.org/10.1306/08121413151.

Garcia-Teijeiro, X. and Rodriguez-Herrera, A. 2014. Dependence of Stress-Induced Micro-Seismicity on Natural Fracture Properties and in-Situ Stress. Presented at the SPE/CSUR Unconventional Resources Conference – Canada, 30 September–2 October, Calgary, Alberta, Canada. SPE-171632-MS. http://doi.org/10.2118/171632-MS.

Granet, S., Fabrie, P., Lemonnier, P. et al. 2001. A Two-Phase Flow Simulation of a Fractured Reservoir Using a New Fissure Element Method. *Journal of Petroleum Science and Engineering* **32** (1): 35-52. https://doi.org/10.1016/S0920-4105(01)00146-2.

Grogan, A.T., Pinczewski, V.W., Ruskauff, G.J. et al. 1988. Diffusion of CO2 at Reservoir Conditions: Models and Measurements. *SPE Reservoir Engineering* **3** (01): 93-102. SPE-14897-PA. https://doi.org/10.2118/14897-PA.

Guevara, E.H. 1988. *Geological Characterization of Permian Submarine Fan Reservoirs of the Driver Waterflood Unit, Spraberry Trend, Midland Basin, Texas*. Report of Inves. United States: Univ of Texas Bureau of Economic.

Hawthorne, S.B., Gorecki, C.D., Sorensen, J.A. et al. 2013. Hydrocarbon Mobilization Mechanisms from Upper, Middle, and Lower Bakken Reservoir Rocks Exposed to CO2. Presented at the SPE Unconventional Resources Conference Canada, Calgary, Alberta, Canada. SPE-167200-MS. https://doi.org/10.2118/167200-MS.

Heinemann, Z.E., Brand, C.W., Munka, M. et al. 1991. Modeling Reservoir Geometry with Irregular Grids. *SPE Reservoir Engineering* **6** (2): 225–232. SPE-18412-PA. http://dx.doi.org/10.2118/18412-PA.

Hoteit, H. 2011. Proper Modeling of Diffusion in Fractured Reservoirs. Presented at the SPE Reservoir Simulation Symposium, The Woodlands, Texas, USA. https://doi.org/10.2118/141937-MS.

Jaeger, J.C. and Cook, N.G.W. 1969. Fundamentals of Rock Mechanics. In. London: Methuen.

Jia, P., Cheng, L., Huang, S. et al. 2015. Production Simulation of Complex Fracture Networks for Shale Gas Reservoirs Using a Semi-Analytical Model. Presented at the SPE Asia Pacific Unconventional Resources Conference and Exhibition, Brisbane, Australia. SPE-176981-MS. https://doi.org/10.2118/176981-MS.

Jin, L., Hawthorne, S., Sorensen, J. et al. 2017. Advancing CO2 Enhanced Oil Recovery and Storage in Unconventional Oil Play—Experimental Studies on Bakken Shales. *Applied Energy* **208**: 171-183. https://doi.org/10.1016/j.apenergy.2017.10.054.

Juanes, R., Samper, J., and Molinero, J. 2002. A General and Efficient Formulation of Fractures and Boundary Conditions in the Finite Element Method. *International Journal for Numerical Methods in Engineering* **54** (12): 1751-1774. 10.1002/nme.491.

Karimi-Fard, M., Durlofsky, L.J., and Aziz, K. 2004. An Efficient Discrete-Fracture Model Applicable for General-Purpose Reservoir Simulators. *SPE Journal* **9** (02): 227-236. SPE-88812-PA. https://doi.org/10.2118/88812-PA.

Karimi-Fard, M. and Firoozabadi, A. 2001. Numerical Simulation of Water Injection in 2d Fractured Media Using Discrete-Fracture Model. Presented at the SPE Annual Technical Conference and Exhibition, New Orleans, Louisiana. 10.2118/71615-MS.

Kazemi, H., Merrill, L.S., Jr., Porterfield, K.L. et al. 1976. Numerical Simulation of Water-Oil Flow in Naturally Fractured Reservoirs. *Society of Petroleum Engineers Journal* **16** (06): 317-326. SPE-5719-PA. 10.2118/5719-PA.

Kemajou, V.N., Bao, A., and Germain, O. 2019. Wellbore Schematics to Structured Data Using Artificial Intelligence Tools. Presented at the Offshore Technology Conference, Houston, Texas. OTC-29490-MS. https://doi.org/10.4043/29490-MS.

Kim, J.-G. and Deo, M.D. 2000. Finite Element, Discrete-Fracture Model for Multiphase Flow in Porous Media. *AIChE Journal* **46** (6): 1120-1130. 10.1002/aic.690460604.

Lake, L.W. 1989. *Enhanced Oil Recovery*. Upper Saddle River, NJ: Prentice Hall.

Lei, Q., Latham, J.-P., and Tsang, C.-F. 2017. The Use of Discrete Fracture Networks for Modelling Coupled Geomechanical and Hydrological Behaviour of Fractured Rocks. *Computers and Geotechnics* **85**: 151-176. https://doi.org/10.1016/j.compgeo.2016.12.024.

Li, C. and King, M.J. 2016. Integration of Pressure Transient Data into Reservoir Models Using the Fast Marching Method. Presented at the SPE Europec featured at 78th EAGE Conference and Exhibition, Vienna, Austria. SPE-180148-MS. https://doi.org/10.2118/180148-MS.

Li, L. and Lee, S.H. 2008. Efficient Field-Scale Simulation of Black Oil in a Naturally Fractured Reservoir through Discrete Fracture Networks and Homogenized Media. *SPE Reservoir Evaluation & Engineering* **11** (04): 750-758. SPE-103901-PA. https://doi.org/10.2118/103901-PA.

Lian, P. and Cheng, L. 2012. The Characteristics of Relative Permeability Curves in Naturally Fractured Carbonate Reservoirs. *Journal of Canadian Petroleum Technology* **51** (02): 137-142. SPE-154814-PA. https://doi.org/10.2118/154814-PA.

Liang, B. and Du, S. 2018. A Novel Workflow for Fracture Reconstruction and Uncertainty Analysis for Unconventional Reservoir Development. Presented at the SPE Liquids-Rich Basins Conference - North America, Midland, Texas, USA. SPE-191795-MS. https://doi.org/10.2118/191795-MS.

Liu, S., Sahni, V., Tan, J. et al. 2018. Laboratory Investigation of EOR Techniques for Organic Rich Shales in the Permian Basin. Presented at the SPE/AAPG/SEG Unconventional Resources Technology Conference, Houston, Texas, USA. URTEC-2890074-MS. https://doi.org/10.15530/URTEC-2018-2890074.

Mccain, W.D., Jr. 1991. Reservoir-Fluid Property Correlations-State of the Art (Includes Associated Papers 23583 and 23594). *SPE Reservoir Engineering* **6** (02): 266-272. SPE-18571-PA. http://doi.org/10.2118/18571-PA.

Mcdaniel, R.R., Holmes, D.V., Borges, J. et al. 2009. Determining Propped Fracture Width from a New Tracer Technology. Presented at the SPE Hydraulic Fracturing Technology Conference, 19-21 January, The Woodlands, Texas. SPE-119545-MS. http://doi.org/10.2118/119545-MS.

Mckenna, J., Grealy, M., Blaz, M. et al. 2016. Using Depletion-Zone Microseismicity to Understand Producing Volumes. In *SEG Technical Program Expanded Abstracts 2016*, 5043-5047. Society of Exploration Geophysicists.

Moinfar, A., Varavei, A., Sepehrnoori, K. et al. 2014. Development of an Efficient Embedded Discrete Fracture Model for 3d Compositional Reservoir Simulation in Fractured

Reservoirs. *SPE Journal* **19** (02): 289-303. SPE-154246-PA. https://doi.org/10.2118/154246-PA.

Nagel, N.B., Garcia, X., Sanchez, M.A. et al. 2012. Understanding "SRV": A Numerical Investigation of "Wet" Vs. "Dry" Microseismicity During Hydraulic Fracturing. Presented at the SPE Annual Technical Conference and Exhibition 8-10 October, San Antonio, Texas, USA. SPE-159791-MS. http://dx.doi.org/10.2118/159791-MS.

Nordgren, R.P. 1972. Propagation of a Vertical Hydraulic Fracture. *SPE Journal* **12** (04): 306-614. SPE-3009-PA. http://doi.org/10.2118/3009-PA.

Olorode, O.M., Freeman, C.M., Moridis, G.J. et al. 2012. High-Resolution Numerical Modeling of Complex and Irregular Fracture Patterns in Shale Gas and Tight Gas Reservoirs. Presented at the SPE Latin America and Caribbean Petroleum Engineering Conference, Mexico City, Mexico. SPE-152482-MS. https://doi.org/10.2118/152482-MS.

Perkins, T.K. and Kern, L.R. 1961. Widths of Hydraulic Fractures. *Journal of Petroleum Technology* **13** (09): 937-949. SPE-89-PA. http://doi.org/10.2118/89-PA.

Phi, T. and Schechter, D. 2017. CO2 EOR Simulation in Unconventional Liquid Reservoirs: An Eagle Ford Case Study. Presented at the SPE Unconventional Resources Conference, Calgary, Alberta, Canada. SPE-185034-MS. https://doi.org/10.2118/185034-MS.

Pieters, D.A. and Graves, R.M. 1994. Fracture Relative Permeability: Linear or Non-Linear Function of Saturation. Presented at the International Petroleum Conference and Exhibition of Mexico, Veracruz, Mexico. SPE-28701-MS. https://doi.org/10.2118/28701-MS.

Putra, E. and Schechter, D.S. 1999. Reservoir Simulation of Waterflood Pilot in Naturally Fractured Spraberry Trend. Presented at the SPE Asia Pacific Oil and Gas Conference and Exhibition, Jakarta, Indonesia. SPE-54336-MS. http://dx.doi.org/10.2118/54336-MS.

Raterman, K.T., Farrell, H.E., Mora, O.S. et al. 2018. Sampling a Stimulated Rock Volume: An Eagle Ford Example. *SPE Reservoir Evaluation & Engineering* **21** (04): 927-941. SPE-191375-PA. https://doi.org/10.2118/191375-PA.

Renner, T.A. 1988. Measurement and Correlation of Diffusion Coefficients for CO2 and Rich-Gas Applications. *SPE Reservoir Engineering* **3** (02): 517-523. SPE-15391-PA. https://doi.org/10.2118/15391-PA.

Riviè, Re, B., Wheeler, M.F. et al. 2000. Part II. Discontinuous Galerkin Method Applied to a Single Phase Flow in Porous Media. *Computational Geosciences* **4** (4): 337-349. 10.1023/a:1011546411957.

Sahni, V. and Liu, S. 2018. Miscible EOR Process Assessment for Unconventional Reservoirs: Understanding Key Mechanisms for Optimal Field Test Design. Presented at the SPE/AAPG/SEG Unconventional Resources Technology Conference, Houston, Texas, USA. URTEC-2870010-MS. https://doi.org/10.15530/URTEC-2018-2870010.

Saputra, I.W.R. and Schechter, D.S. 2018. Comprehensive Workflow for Laboratory to Field-Scale Numerical Simulation to Improve Oil Recovery in the Eagle Ford Shale by Selective Testing and Modelling of Surfactants for Wettability Alteration. Presented at the SPE/AAPG/SEG Unconventional Resources Technology Conference, Houston, Texas, USA. URTEC-2884598-MS. https://doi.org/10.15530/URTEC-2018-2884598.

Shapiro, S.A., Dinske, C., and Berlin Freie, U. 2009. Fluid-Induced Seismicity: Pressure Diffusion and Hydraulic Fracturing. *GEOPHYSICAL PROSPECTING* **57** (2): 301-310. http://dx.doi.org/10.1111/j.1365-2478.2008.00770.x.

Sharma, M.M. and Manchanda, R. 2015. The Role of Induced Un-Propped (Iu) Fractures in Unconventional Oil and Gas Wells. Presented at the SPE Annual Technical Conference and Exhibition, 28-30 September, Houston, Texas, USA. SPE-174946-MS. http://doi.org/10.2118/174946-MS.

Sigmund, P.M. 1976a. Prediction of Molecular Diffusion at Reservoir Conditions. Part 1-Measurement and Prediction of Binary Dense Gas Diffusion Coefficients. *Journal of Canadian Petroleum Technology* **15** (02): 11. PETSOC-76-02-05. https://doi.org/10.2118/76-02-05.

Sigmund, P.M. 1976b. Prediction of Molecular Diffusion at Reservoir Conditions. Part II - Estimating the Effects of Molecular Diffusion and Convective Mixing in Multicomponent Systems. *Journal of Canadian Petroleum Technology* **15** (03): 11. PETSOC-76-03-07. https://doi.org/10.2118/76-03-07.

Smith, M.B. and Montgomery, C.T. 2015. *Hydraulic Fracturing*: Taylor & Francis.

Sun, J. 2016. *Characterization and Simulation of Discrete Fracture Networks in Unconventional Shale Reservoirs*. Doctoral dissertation, Texas A & M University

Sun, J., Niu, G., and Schechter, D. 2016a. Numerical Simulation of Stochastically-Generated Complex Fracture Networks by Utilizing Core and Microseismic Data for Hydraulically Fractured Horizontal Wells in Unconventional Reservoirs– a Field Case Study. Presented at the SPE Eastern Regional Meeting, Canton, Ohio. 13–15 September. SPE-184077-MS. https://doi.org/10.2118/184077-MS.

Sun, J. and Schechter, D. 2015. Optimization-Based Unstructured Meshing Algorithms for Simulation of Hydraulically and Naturally Fractured Reservoirs with Variable Distribution

of Fracture Aperture, Spacing, Length, and Strike. *SPE Reservoir Evaluation & Engineering* **18** (04): 463-480. SPE-170703-PA. http://doi.org/10.2118/170703-PA.

Sun, J., Schechter, D., and Huang, C.-K. 2015. Sensitivity Analysis of Unstructured Meshing Parameters on Production Forecast of Hydraulically Fractured Horizontal Wells. Presented at the Abu Dhabi International Petroleum Exhibition and Conference, 9-12 November, Abu Dhabi, UAE. SPE-177480-MS. http://doi.org/10.2118/177480-MS.

Sun, J., Schechter, D., and Huang, C.-K. 2016b. Grid-Sensitivity Analysis and Comparison between Unstructured Perpendicular Bisector and Structured Tartan/Local-Grid-Refinement Grids for Hydraulically Fractured Horizontal Wells in Eagle Ford Formation with Complicated Natural Fractures. *SPE Journal* **21** (06): 2260-2275. SPE-177480-PA. https://doi.org/10.2118/177480-PA.

Syihab, Z. 2009. *Simulation on Discrete Fracture Network Using Flexible Voronoi Grid System*. PhD Dissertation, Texas A&M University (December 2009)

Torres, J.A., Jin, L., Bosshart, N.W. et al. 2018. Multiscale Modeling to Evaluate the Mechanisms Controlling CO2- Based Enhanced Oil Recovery and CO2 Storage in the Bakken Formation. Presented at the SPE/AAPG/SEG Unconventional Resources Technology Conference, Houston, Texas, USA. URTEC-2902837-MS. https://doi.org/10.15530/URTEC-2018-2902837.

Tovar, F.D., Barrufet, M.A., and Schechter, D.S. 2018a. Gas Injection for EOR in Organic Rich Shale. Part I: Operational Philosophy. Presented at the SPE Improved Oil Recovery Conference, Tulsa, Oklahoma, USA. SPE-190323-MS. https://doi.org/10.2118/190323-MS.

Tovar, F.D., Barrufet, M.A., and Schechter, D.S. 2018b. Gas Injection for EOR in Organic Rich Shales. Part II: Mechanisms of Recovery. Presented at the SPE/AAPG/SEG Unconventional Resources Technology Conference, Houston, Texas, USA. URTEC-2903026-MS. https://doi.org/10.15530/URTEC-2018-2903026.

Tovar, F.D., Eide, O., Graue, A. et al. 2014. Experimental Investigation of Enhanced Recovery in Unconventional Liquid Reservoirs Using CO2: A Look Ahead to the Future of Unconventional EOR. Presented at the SPE Unconventional Resources Conference, The Woodlands, Texas, USA. SPE-169022-MS. https://doi.org/10.2118/169022-MS.

Wang, L. and Yu, W. 2019. Gas Huff and Puff Process in Eagle Ford Shale: Recovery Mechanism Study and Optimization. Presented at the SPE Oklahoma City Oil and Gas Symposium, Oklahoma City, Oklahoma, USA. SPE-195185-MS. https://doi.org/10.2118/195185-MS.

Wang, Y. and Shahvali, M. 2016. Discrete Fracture Modeling Using Centroidal Voronoi Grid for Simulation of Shale Gas Plays with Coupled Nonlinear Physics. *Fuel* **163**: 65-73. https://doi.org/10.1016/j.fuel.2015.09.038.

Wang, Z., Li, C., and King, M. 2017. Validation and Extension of Asymptotic Solutions of Diffusivity Equation and Their Applications to Synthetic Cases. Presented at the SPE Reservoir Simulation Conference, Montgomery, Texas, USA. SPE-182716-MS. https://doi.org/10.2118/182716-MS.

Warpinski, N.R., Wolhart, S.L., and Wright, C.A. 2004. Analysis and Prediction of Microseismicity Induced by Hydraulic Fracturing. *SPE Journal* **9** (01): 24-33. SPE-87673-PA. http://doi.org/10.2118/87673-PA.

Warren, J.E. and Root, P.J. 1963. The Behavior of Naturally Fractured Reservoirs. *Society of Petroleum Engineers Journal* **3** (03): 245-255. SPE-426-PA. https://doi.org/10.2118/426-PA.

Wheaton, B., Haustveit, K., Deeg, W. et al. 2016. A Case Study of Completion Effectiveness in the Eagle Ford Shale Using DAS/DTS Observations and Hydraulic Fracture Modeling. Presented at the SPE Hydraulic Fracturing Technology Conference, 9-11 February, The Woodlands, Texas, USA. SPE-179149-MS. http://doi.org/10.2118/179149-MS.

Wu, C.-H., Yi, S., and Sharma, M.M. 2017a. Proppant Distribution among Multiple Perforation Clusters in a Horizontal Wellbore. Presented at the SPE Hydraulic Fracturing Technology Conference and Exhibition, 24–26 January, The Woodlands, Texas, USA. SPE-184861-MS. http://doi.org/10.2118/184861-MS.

Wu, W., Kakkar, P., Zhou, J. et al. 2017b. An Experimental Investigation of the Conductivity of Unpropped Fractures in Shales. Presented at the SPE Hydraulic Fracturing Technology Conference and Exhibition, 24–26 January, The Woodlands, Texas, USA. SPE-184858-MS. http://doi.org/10.2118/184858-MS.

Wu, Y.-S. and Pruess, K. 1988. A Multiple-Porosity Method for Simulation of Naturally Fractured Petroleum Reservoirs. *SPE Reservoir Engineering* **3** (01): 327-336. SPE-15129-PA. https://doi.org/10.2118/15129-PA.

Xu, Y. and Sepehrnoori, K. 2019. Development of an Embedded Discrete Fracture Model for Field-Scale Reservoir Simulation with Complex Corner-Point Grids. *SPE Journal* **Preprint** (Preprint): 24. SPE-195572-PA. https://doi.org/10.2118/195572-PA.

Xue, X., Yang, C., Park, J. et al. 2018. Reservoir and Fracture-Flow Characterization Using Novel Diagnostic Plots. *SPE Journal* **Preprint** (Preprint): 22. SPE-194017-PA. https://doi.org/10.2118/194017-PA.

Xue, X., Yang, C., Sharma, V.K. et al. 2016. Reservoir and Fracture Flow Characterization Using a Novel W(T) Formulation. Presented at the SPE/AAPG/SEG Unconventional Resources Technology Conference, San Antonio, Texas, USA. URTEC-2440083-MS. https://doi.org/10.15530/URTEC-2016-2440083.

Yang, C., King, M.J., and Datta-Gupta, A. 2017a. Rapid Simulation of Naturally Fractured Unconventional Reservoirs with Unstructured Grids Using the Fast Marching Method. Presented at the SPE Reservoir Simulation Conference, Montgomery, Texas, USA. SPE-182612-MS. https://doi.org/10.2118/182612-MS.

Yang, C., Xue, X., King, M.J. et al. 2017b. Flow Simulation of Complex Fracture Systems with Unstructured Grids Using the Fast Marching Method. Presented at the SPE/AAPG/SEG Unconventional Resources Technology Conference, Austin, Texas, USA. URTEC-2691393-MS. https://doi.org/10.15530/URTEC-2017-2691393.

Yu, W., Huang, S., Wu, K. et al. 2014. Development of a Semi-Analytical Model for Simulation of Gas Production in Shale Gas Reservoirs. Presented at the SPE/AAPG/SEG Unconventional Resources Technology Conference, Denver, Colorado, USA. URTEC-1922945-MS. https://doi.org/10.15530/URTEC-2014-1922945.

Yu, W., Zhang, Y., Varavei, A. et al. 2019. Compositional Simulation of CO2 Huff 'N' Puff in Eagle Ford Tight Oil Reservoirs with CO2 Molecular Diffusion, Nanopore Confinement, and Complex Natural Fractures. *SPE Reservoir Evaluation & Engineering* **22** (02): 492 - 508. SPE-190325-PA. https://doi.org/10.2118/190325-PA.

Zhang, F., Saputra, I.W.R., Adel, I.A. et al. 2018a. Scaling for Wettability Alteration Induced by the Addition of Surfactants in Completion Fluids: Surfactant Selection for Optimum Performance. Presented at the SPE/AAPG/SEG Unconventional Resources Technology Conference, Houston, Texas, USA. URTEC-2889308-MS. https://doi.org/10.15530/URTEC-2018-2889308.

Zhang, F., Saputra, I.W.R., Niu, G. et al. 2018b. Upscaling Laboratory Result of Surfactant-Assisted Spontaneous Imbibition to the Field Scale through Scaling Group Analysis, Numerical Simulation, and Discrete Fracture Network Model. Presented at the SPE Improved Oil Recovery Conference, 14-18 April 2018, Tulsa, Oklahoma. SPE-190155-MS. https://doi.org/10.2118/190155-MS.

Zhang, F., Saputra, I.W.R., Parsegov, S.G. et al. 2019. Experimental and Numerical Studies of EOR for the Wolfcamp Formation by Surfactant Enriched Completion Fluids and Multi-Cycle Surfactant Injection. Presented at the SPE Hydraulic Fracturing Technology Conference and Exhibition, The Woodlands, Texas, USA. SPE-194325-MS. https://doi.org/10.2118/194325-MS.

Zhou, W., Banerjee, R., Poe, B.D. et al. 2013. Semianalytical Production Simulation of Complex Hydraulic-Fracture Networks. *SPE Journal* **19** (01): 6-18. SPE-157367-PA. https://doi.org/10.2118/157367-PA.

Zhou, X., Morrow, N.R., and Ma, S. 2000. Interrelationship of Wettability, Initial Water Saturation, Aging Time, and Oil Recovery by Spontaneous Imbibition and Waterflooding. *SPE Journal* **5** (02): 199-207. SPE-62507-PA. https://doi.org/10.2118/62507-PA.

Zou, A.F. 2015. *Compositional Simulation of CO2 Enhanced Oil Recovery in Unconventional Liquid Reservoirs*